Emission of intermediate mass fragments in the p(1.9 GeV)+^{nat}Ni reaction

Arkadiusz Bubak

Berichte des Forschungszentrums Jülich ; 4138
ISSN 0944-2952
Institut für Kernphysik Jül-4138
(Diss., Katowice, Univ., 2004)

Zu beziehen durch: Forschungszentrum Jülich GmbH · Zentralbibliothek
D-52425 Jülich · Bundesrepublik Deutschland
☎ 02461 61-5220 · Telefax: 02461 61-6103 · e-mail: zb-publikation@fz-juelich.de

Abstract

The emission of the intermediate mass fragments (IMFs; $2 \leqslant Z \leqslant 14$) produced in the interaction of 1.9 GeV protons with nickel (^{nat}Ni) has been a subject of interest of the present study. Energy spectra of isotopically and elementally identified ejectiles have been measured at angles 15° and 120° with the respect to the beam direction. The identification of the emitted IMFs has been performed by means of the Bragg curve spectroscopy and the time-of-flight technique (TOF). The Bragg curve detectors (BCDs) were employed for the charge identification, whereas the TOF method combined with the BCD, for the mass identification. The main task of the present PhD thesis was to built appropriate data acquisition system, to perform the experiment on the internal beam of the COSY accelerator, to propose the methodology of the off-line analysis of the data, to apply it to the event-by-event stored data, and to perform the phenomenological analysis of the obtained data. The results, experimental procedures, and different techniques of the element and isotope identification by means of the BCD + TOF are presented. The determination of the power law parameter τ characterizing the mass and charge distributions of the reaction products is discussed. Various methods of the nuclear matter temperature determination, the comparison between nuclear matter thermometers, and the discussion of the obtained results, shown in the energy-temperature diagram (the so called caloric curve), are presented as well. The results suggest two different mechanisms of the IMFs production: from the equilibrated (IMFs measured at 120°), and non-equilibrated (IMFs measured at 15°) state of the nucleus.

Streszczenie

Emisja naładowanych fragmentów o ładunku $2 \leqslant Z \leqslant 14$, produkowanych w zderzeniach p(1.9 GeV) + ^{nat}Ni, była przedmiotem zainteresowania przedstawionych badań. Energetyczne widma emitowanych cząstek, zidentifikowanych pierwiastkowo i izotopowo, były mierzone pod kątami 15° i 120° względem kierunku padającej wiązki. Identyfikacja cząstek została przeprowadzona przy użyciu detektorów Bragg'a i techniki czasu przelotu. Głównymi zadaniami pracy doktorskiej było: zbudowanie odpowiedniego systemu akwizycji danych, przeprowadzenie eksperymentu na wewnętrznej wiązce akceleratora COSY, zaproponowanie metod analizy danych w tzw. trybie *off-line*, zastosowanie tych metod do opracowania wyników pomiaru zapisanych w formie *event-by-event*, oraz przeprowadzenie fenomenologicznej analizy opracowanych danych. Otrzymane wyniki, zastosowane procedury i techniki identyfikacji fragmentów reakcji przy użyciu detektorów Bragg'a i techniki czasu przelotu są przedstawione w niniejszej pracy. Dyskutowane jest także wyznacznie wartości parametru τ charakteryzującego rozkład masy i ładunku obserwowanych fragmentów. Innym poruszanym tematem jest wyznaczanie różnymi metodami temperatury materii jądrowej będącej w stanie równowagi, oraz prezentacja otrzymanych wartości na krzywej kaloryczniej.

Contents

Chapter 1

Introduction

All truth passes through three stages. First, it is ridiculed. Second, it is violently opposed. Third, it is accepted as being self-evident.

Arthur Schopenhauer, 1788–1860

The production of nuclear fragments by intermediate and high-energy protons interacting with nuclei has been investigated over four decades [1–6]. During this time many experiments have addressed key questions regarding the processes occurring in hot nuclei and behavior of highly excited nuclear matter created in the proton and heavy ion collisions with nuclei. Among these questions the fundamental ones are related to:

- Expansion and breakup of an excited system.
- Expansion of the nucleus during excitation and its subsequent decay [7–14].
- Multifragmentation of nuclei [10–13].
- Competition between sequential and simultaneous emission of fragments from the highly excited thermalized nuclei [15].
- Thermodynamic equilibration (chemical and thermal) in the excited nuclear system generated by nuclear collision.
- Non-equilibrium effects in the fragmentation [16].
- Pre-equilibrium particle emission [17, 18].
- Caloric curve and phase transition in nuclear matter [19–26].
- Production mechanism of the intermediate mass fragments (IMFs; $4 < A <$ mass of fission fragments) and its relation to the possible liquid-gas phase transition [22, 23, 27–29].
- Astrophysical aspects of the production of lithium, beryllium and boron elements [30, 31].

The only way to find an explanation of these issues leads through the complex and systematic studies of the proton-nucleus collision processes, by measurements of the kinetic energies and angular distributions of the ejectiles. The most comprehensive compilation of the existing data for the production cross sections in proton induced reactions on different targets can be found in Refs. [32–34], and references therein. In the course of systematic measurements of the production cross sections this compilation comprises about 15000 entries for about 550 target/product combinations. Of course, the existing data is far to be complete, and moreover some production cross sections obtained in different experiments differ significantly (up to order of magnitude) [34–37]. The lack of data refers especially to the long-lived radionuclides, nuclides far from the stability, and light and intermediate mass fragments emitted in the proton induced reactions. The experimental data are incomplete with the respect to the coverage of the target-product combinations, and the particles energies as well. For the light charged particles and intermediate mass fragments emitted in the proton induced reactions it is particularly visible in the beam energy

range above 1 GeV [5, 38, 39]. It is shown in Fig. 1.1, where the measured helium production cross sections for proton induced reactions on Fe are shown.

Also, the theoretical predictions of the production cross sections in proton-nucleus collisions, which could fill the gaps in the experimental database, are not satisfactory [36]. For example, the calculated light and intermediate mass fragments production cross sections deviate by factor of 5–10 from the experimental data [40]. There is no phenomenological systematics available to predict, with a good accuracy, the production cross sections, as well. Therefore the best possible way to obtain required data is to measure them.

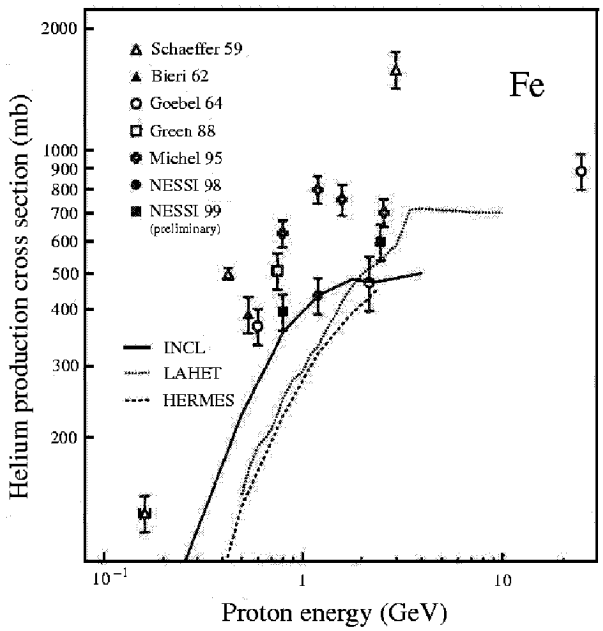

Figure 1.1. Helium production cross section for p-induced reaction on Fe as a function of proton incident energy. The data are from: Schaeffer 59 [41], Bieri 62 [42], Goebel 64 [43], Green 88 [44], Michel 95 [32], NESSI 98 [35] and NESSI 99 [45]. The lines show the results of calculations with INCL [46,47], HERMES [48], and LAHET [49,50] codes. Fig. adopted from Refs. [35,45].

The reliable data of production cross sections in proton induced reactions are important for the design and construction of the accelerator driven systems[1] (ADS) or spallation neutron sources[2] (e.g. SNS[3], ESS[4] or JSNS[5]). The focus has to be especially put on the production of the lightest particles like neutron, proton, deuteron, tritium and α-particles. In addition, the knowledge of intermediate mass fragments and fission products is of interest. The measured production cross sections will allow to estimate the energy deposition in the target materials. The technical problems which appear during designing ADS or spallation facilities are mainly related to the structural-radiation damages of the materials used for its construction, and radiation safety. The radiation damages caused by the helium production in the materials, which separate the radioactive target from the accelerator vacuum, highly limit their life-time. The radiation safety is e.g. related to the production of tritium (the radio-toxicity gas) during the operation of the

[1]Facility which uses the proton accelerator to destroy the nuclear waste. It is particularly attractive for the transmutation of heavy, long-lived isotopes produced by presently operating nuclear reactors into shorter-lived fission fragments.

[2]Facility which can produce intensive neutron beam. Neutron scattering can be used to study the arrangement, motion, and interaction of atoms in materials. It provides information which often cannot be obtained using other techniques, such as optical spectroscopy, electron microscopy, or X-ray diffraction.

[3]The American Spallation Neutron Source.

[4]The European Spallation Source.

[5]The Japanese Spallation Neutron Source.

liquid Hg target, presently the most favored target for the spallation source. Also the Accelerator-Based Conversion (ABC[6]) and Accelerator-Driven Energy Production (ADEP[7]) [51] require complete and precise nuclear data on the reactions induced by the nucleons, pions, and other projectiles in the energy range up to several GeV. During last years also the increasing use of the proton beams in cancer radiotherapy needs large and precise nuclear data libraries for the simulation of the radiation transport. This is extremely important for the selection of the optimal dose in the therapy.

These reasons motivated us to start a new experiment. In 1999 a new experimental project was launched. It aimed at determination of various intermediate mass fragments yields, in a wide range of their kinetic energy, charge and mass, produced by the protons (beam energies in the range 0.2–2.5 GeV) interacting with several targets (C, Fe, Au, Ag, Ni, N-melamine, Si and SiO_2). The project was named PISA (**P**roton **I**nduced **S**p**A**llation). The first measurement was carried out at the internal beam of the COSY (**CO**oler **SY**nchrotron) storage ring in the Forschungszentrum Jülich (Germany) in October 2002. During this measurement three different thin targets ($\sim$ 200 μg/cm^2) were used: C, Ni and Au bombarded by 1.9 GeV protons. The identification of the reaction products has been realized by means of the following detectors:

- two microchannelplate detectors (MCPD) working as "Start" and "Stop" detectors for the time-of-flight measurement (TOF),
- Bragg Curve Detectors (BCD) for the identification of the intermediate mass fragments in the low energy range (0.5–6 MeV/A [8]), followed by
- three silicon detectors in the telescope geometry for the identification of the light energetic particles, in energy range above 6 MeV/A,
- cooled silicon detectors intended for the identification of the IMFs produced in the low energy range (0.5–6 MeV/A), and
- set of the double scintillator detectors (phoswich detectors) intended for the identification of the light, charged evaporation and spallation products with energies above 6 MeV/A.

In this thesis the study of the IMFs emission induced by 1.9 GeV protons interacting with ^{nat}Ni is presented. The emphasis is put into the identification of the reaction products measured at 15° and 120° with the respect to the beam direction. The fragment identification was performed by means of the Bragg curve spectroscopy (BCS) and time-of-flight (TOF) technique. By combining the results from BCDs and MCPDs the identification of the following isotopes was possible: ^{6}Li, ^{7}Li, ^{8}Li, ^{7}Be, ^{9}Be, ^{10}Be, ^{10}B, ^{11}B, ^{11}C, ^{12}C, ^{13}C, ^{14}C, ^{13}N and ^{14}N. The advantages of using the BCD are: extremely low detection energy threshold ($\sim$ 0.5 MeV/A), and brilliant element resolution. The different methods which utilize the BCS for the identification of the IMFs were applied.

In the intermediate-energy proton-ion collisions IMFs are emitted from the highly excited nuclear matter [7, 52]. The studies performed with high-energy protons [1, 6, 32, 33, 53, 54] and intermediate-heavy ions [55, 56] suggest also the phase transition in the nuclear matter as a possible source of the IMFs [10, 19, 57].

The existing data on the production cross sections in proton induced reactions suggest that the emission of lighter fragments occurs predominantly from the non-equilibrated nucleus, whereas heavier fragments are emitted mostly from the equilibrated system. It was also noticed that the mechanism of the IMFs emission evolves from the fast emission from a non-equilibrated system at intermediate and high energies of bombarding protons, to the decay of a fully thermally equilibrated nucleus, at low incident beam energies [52]. Therefore, various scenarios of the reaction mechanism should be reflected in the angular and energy distributions of the emitted IMFs. Thus, the differences in the shape of the energy spectra of emitted fragments at various angles may serve as an evidence of the different fragments production mechanisms. It was also found

[6] Facility which can completely destruct of weapons plutonium.

[7] Facility which can produce fission energy from thorium, with concurrent destruction of the long-lived waste, and without the production of weapons-usable isotopes.

[8] energy per mass unit; E/A = E/u = E/amu

that the yield distribution of mass fragments (A_f) obeys a power law behavior, ${A_f}^{-\tau}$ [1, 6]. Therefore, the τ parameter may also reflect changes in the reaction mechanism [4, 53].

The sequential emission of particles from various stages of the reaction can be characterized by different parameters as power law parameter, excitation energy, temperature and density. Their determination can help to answer the questions addressed at the beginning of this section.

On the basis of the obtained yields, kinetic energy and angular distributions of IMFs in the PISA experiment, in this thesis the following three aspects of the nuclear reactions are discussed: the particles emission from the equilibrated nucleus, changes in the IMFs production mechanisms, and the determination of the temperature of highly excited thermalized nucleus. The determination of the temperature of the nuclear matter was based on the following two techniques: (i) the slope of the kinetic energy spectra of particles emitted from the nucleus [4, 52, 53, 58], and (ii) the double isotopic yield ratio of emitted particles [27, 28, 59–62].

The significant part of this thesis is also related to the description of the software package used in the PISA experiment. The data acquisition system for the PISA experiment has been prepared from scratch within this thesis.

The contents of the thesis is the following. Chapter 2 brings up theoretical issues of the nuclear reaction mechanism (multifragmentation, fission and spallation), the concept of thermal and chemical equilibrium of the nuclear matter, liquid to gas phase transition, and related with it the idea of the nuclear matter temperature. In Chapter 3 an overview of the setup of the apparatus used in the PISA experiment is given. In Chapter 4 the data acquisition system for the PISA experiment is presented. The software package used for on- and off-line analysis of the data is described as well. Section 5 is devoted to the description of the electronic circuit and trigger conditions used during data collection. Section 6 brings the readers in contact with the experimental procedures and results. The main emphasis was put on the methods of analyzing of the signals from the BCD. The methods of the intermediate mass fragments identification using the BCD only, and combining the information from the BCD and time-of-flight technique are shown. The determination of the nuclear matter temperature using two nuclear thermometers, and comparison between them are also presented. The comparison of the PISA results with those obtained by others is given as well. In appendix A, a few screenshots of the graphical user interface (GUI) of programs from the PISA software package are shown. In appendix B, the results of the simulation of the PISA experiment by means of Geant4 package [63] and Srim-2003 code [64, 65] are presented. The spectra from cooled silicon detectors used in the PISA experiment are shown in appendix C.

This work has partially been supported by the European Union HINDAS project FIS5-1999-00150.

Chapter 2

Theory overview

Felix, qui potuit rerum cognoscere causas

Publius Vergilius Maro, 70–19 B.C.

2.1 Mechanisms of nuclear reactions

When a high-energy proton penetrates a nucleus at least three major mechanisms of nuclear reaction can be distinguished: multifragmentation (fragmentation), fission and spallation. In general, multifragmentation (fragmentation) is a process in which light fragments, in the mass range $3 \lesssim A \lesssim 20$ ($10 \lesssim A \lesssim 50$) are produced in the decay of a compound nucleus. The fission process leads to the production of fragments with masses around $A_T/2$, where A_T is the mass of the target nucleus. This process dominates for protons interacting with heavy targets, generally with targets having a large fissility. Fragments with masses larger then $A_T/2$ are produced in the spallation process. The schematic overview of various mechanisms of proton-nucleus collision is shown in Fig. 2.1, where fragments multiplicity versus mass of the fragment is presented. This division is not strict, because e.g. evaporation process, which is considered as a part of the spallation mechanism, also yields several light fragments.

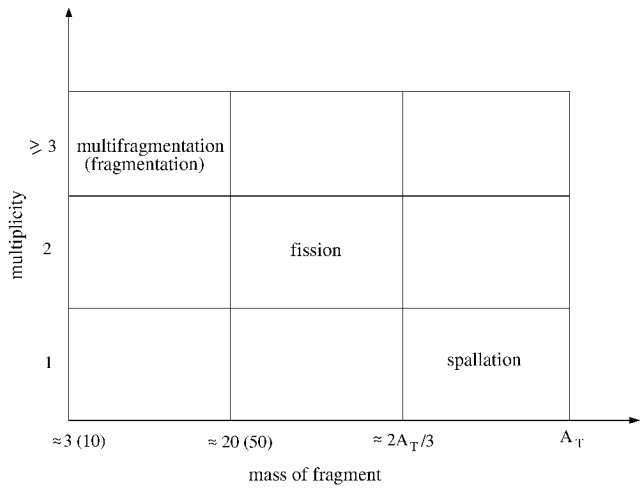

Figure 2.1. Multiplicity of fragments produced in proton-nucleus collisions versus mass of the fragment. Multifragmentation (fragmentation), fission and spallation processes are marked. The numbers in parentheses correspond to the fragmentation process. This figure with some modifications is taken from Ref. [66].

Details concerning the multifragmentation, fission and spallation processes are presented in following sections.

2.1.1 Multifragmentation process

The phenomenon in which fragments heavier than alpha particles, but lighter than fission fragments, are emitted in collisions of relativistic protons with various targets was discovered in cosmic rays in the thirties of 20th century [67, 68]. This process was named nuclear fragmentation or particle break-up. Later also multifragmentation (multiparticle break-up) process has been distinguished. The fragmentation is a process in which the particles in the mass range $10 \lesssim A \lesssim 50$ are produced, whereas during the multifragmentation, products with $3 \lesssim A \lesssim 20$ are observed, and no heavy remnant remains.

Scheme of the multifragmentation (fragmentation) process is shown in Fig. 2.2.

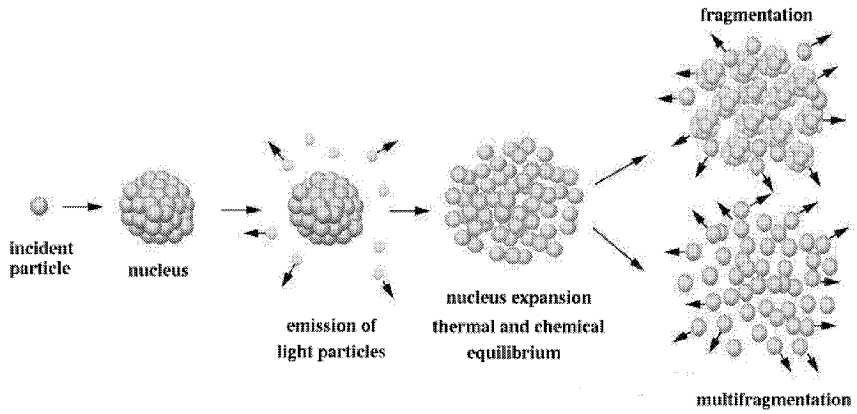

Figure 2.2. Scheme of the multifragmentation (fragmentation) process.

Recently, a lot of effort has been done to develop the theoretical description of the multifragmentation process. Significant progress in the understanding of this process was achieved using the data from accelerator experiments [15]. Several theoretical models were developed to explain the copious production of fragments:

- **microscopic dynamical models** related to the molecular dynamics, quantum molecular dynamics (QMD) or time dependent Hartree-Fock theory [69–76],
- **kinetic models** related to the Boltzmann(Vlasov)-Uehlig-Uhlenbeck (BUU, VUU) equations [77–80],
- **probabilistic models** [81–84],
- **macroscopic models** related to the Fisher condensation theory, coexistence of phase and critical indexes [85–89],
- **statistical models** (quantum statistical model (QSM), statistical multifragmentation model (SMM)) [9, 14, 90–95].

2.1.2 Fission process

In 1930s it was discovered that the neutrons can be captured by heavy nuclei and this leads to the production of new radioactive isotopes. Hahn and Strassman [96] observed, that uranium nuclei, after neutron capture, disintegrate into smaller fragments. This process was named "fission" by Meitner and Frish [97]. The fission is defined as a process when a nucleus divides or splits into two roughly equal nuclei, and two or three free neutrons. This process is associated with the release of substantial amount of energy. In the case of uranium nucleus (^{235}U) it is

about 180 MeV. The splitting of an atomic nucleus can occur either as a result of impact of the particles (usually neutrons) or spontaneously.

The decision whether a highly excited hot nucleus undergoes fission or just evaporation is driven by the competition between attractive surface tension (surface forces tension acted by short ranging nuclear forces) and repelling electrostatic Coulomb forces. In Fig. 2.3 the correlation between potential energy of the nucleus and deformation is shown. Beginning from the ground state-deformed nucleus point (Gsd) the deformation increases with increasing of the potential energy of nucleus towards the so-called saddle point deformation (Spd). Beyond the saddle point the potential energy declines due to the decreasing of the Coulomb repulsion until the scission point is reached. In Fig. 2.4, where the fission barrier (B_f), which represents difference between the ground state potential energy and the potential energy at the saddle point of the deformation, is plotted as a function of the nucleus mass (A), it is shown that fission barrier declines with increasing excitation energy of nucleus E^*. It is also shown that beyond maximum of the B_f at $A \simeq 70$, the fission barrier declines.

Scheme of the fission process is shown in Fig. 2.5.

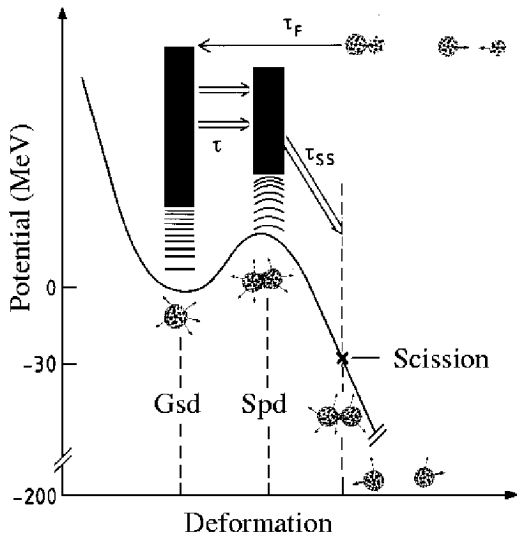

Figure 2.3. Potential energy as a function of the deformation. Abbreviations: Gsd – ground state-deformed nucleus point; Spd – saddle point deformation. Fig. adapted from Ref. [98].

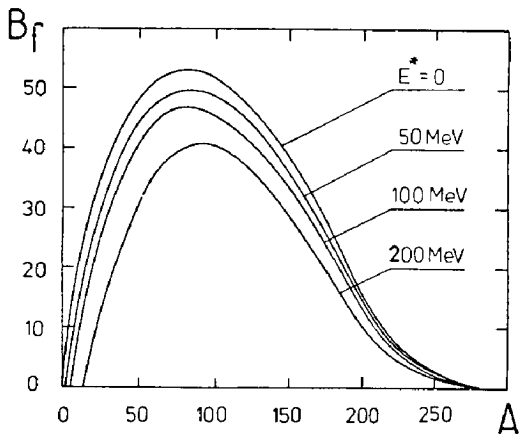

Figure 2.4. Fission barrier B_f as a function of atomic number A and E^* along the β-stability line. B_f is given in units of MeV. Fig. adapted from Ref. [99]

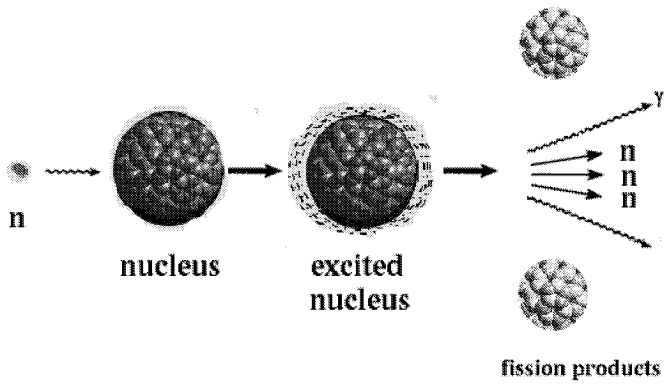

Figure 2.5. Scheme of the fission process.

2.1.3 Spallation process

The spallation refers to a non-elastic nuclear interaction induced by high energy particles in which several secondary particles are produced. A few theoretical models, which try to describe this process, exist. The most widely used distinguish three stages in the spallation process: intranuclear cascade, pre-equilibrium and deexcitation phase. During the first stage the incident particle undertakes collisions with individual nucleons inside the nucleus. During sequence of collisions light particles like protons, neutrons and pions, but also heavier fragments are immediately "spalled", or knocked out from the nucleus, while others remain inside the nucleus increasing the excitation energy of the target-like nucleus. The various theoretical models try to, in different way, deduce the time when the intranuclear cascade is stopped. For example: (i) in the Liège intranuclear cascade model [46, 47] this time is connected to the observed change in the calculated emission rates of light particles, whereas in (ii) the Bertini-type code [100] the stopping time is obtained from the energy of the fastest particle remaining in the nucleus. The first stage of the spallation process takes place during the time of about $10^{-23} - 10^{-22}$ s after collision. The second stage called pre-equilibrium, takes place during the time of about $10^{-22} - 10^{-21}$ s after collision. It leads to the last stage when, either other particles after some time are "boiled off", as the bombarded nucleus heats up, or the excited nucleus divides into two fragments. Each of this fragments can be in an excited state and further emits particles. It is so called the evaporation or fission phase (asymmetrical fission phase). The last stage happens on a much larger time scale. The mean lifetime of an excited nucleus depends very much on its excitation energy E^*. At the end of the deexcitation process, when not enough energy is stored as thermal heat in the nucleus to emit nucleons, γ rays are produced.

The scheme of the spallation process with various possible phases is shown in Fig. 2.6.

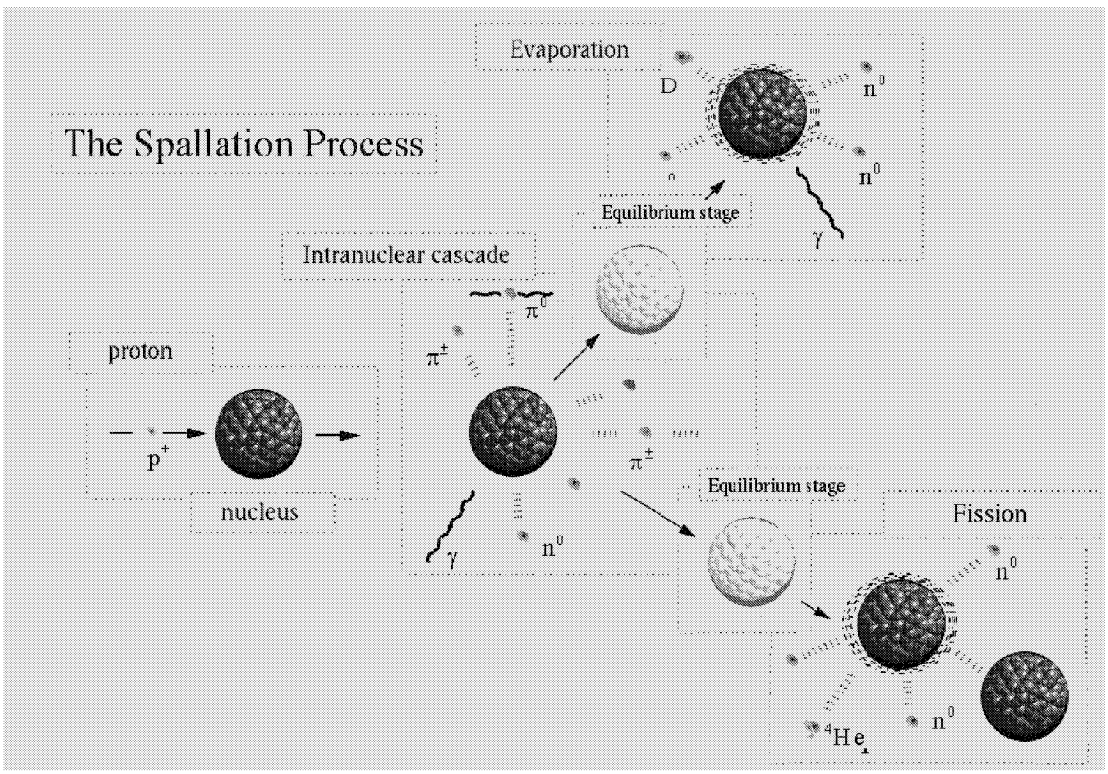

Figure 2.6. Scheme of the spallation process. Three stages of the process are indicated.

2.2 Thermal and chemical equilibrium

The investigation of some aspects of the nuclear matter presented in this thesis have been performed in terms of the equilibrium of the system. Therefore it is important to precise what thermal and chemical equilibrium mean. In general, the state of equilibrium can be defined as a state of dynamic balance in which the rates of forward and reverse reactions are equal (i.e. neither forward nor reverse reaction is favored). If one considers the nucleus, the equilibrium can be characterized as a state when the dynamical information, for example number of particles, momentum, etc., are frozen for a given time. There are two types of equilibrium: thermal and chemical. They can be characterized as follows. The nucleus is a state of hadronic matter at approximately zero temperature and low density. In the proton-nucleus collisions, the temperature and the density of the created nucleus increase. Then the system begins to expand and cools down (due to the particles emission) to the moment when the particles inside the system cease interacting strongly with each other. It is a state of the system with fixed ratios of different particles. The nucleus reaches chemical equilibrium of particles abundance. This is referred as a chemical equilibrium. There is also another type of the equilibrium. During further expansion of the nucleus the temperature goes down to the point where the interactions between particles are no longer effective. This is referred as a thermal equilibrium.

2.3 Liquid to gas phase transition

The energy transfered to the nucleus in proton-nucleus collisions leads to the state of nuclear matter which is far away from normal conditions (approximately zero temperature and density of about 0.17 nucleons/fm^3). The description of such system leads to the idea of the phase transition (PT) in nuclear matter, which is similar to the PT observed in e.g. water. In water one can observe three phases (states): solid, liquid and gas, known as ice, water and steam. Temperature and pressure determine the state of water molecules. Similar situation is observed in nuclear matter where neutrons and protons exhibit various states depending on the local temperature and density. Therefore one can try to present the thermodynamical properties of the nuclear matter similarly to thermodynamical properties of water, either (i) in the phase diagram, where the temperature is plotted versus the pressure, or (ii) using the so called caloric curve (CC) diagram, where temperature is plotted against the excitation energy E^*. The schematic view of the CC is shown in Fig. 2.7 on the next page. The temperature rises at low values of E^*, has a plateau at moderate values of E^*, and rises again at higher excitation energies. This is interpreted as an evidence of the first order liquid-gas PT. In fact, in nuclear matter two PTs are observed: (i) one related to temperatures of a few MeV (1 MeV $\approx 10^{10}$ K), and called first oder liquid-gas PT, and (ii) second one which is expected at the temperature of about 150 MeV. In the latter, nucleons themselves undergo a phase transition. Therefore it is expected to observe a transition from nuclear matter to the quark-gluon plasma. The second PT is beyond the scope of the PISA collaboration measurements due to the limited incident proton energy, therefore only the first one will be considered.

In contrast to the "normal" matter (e.g. water) the nuclear matter can not be kept in PT state long enough to study its properties. The interval time is about 10^{-21} seconds. Therefore PT values of temperature (T), pressure (p) and density (ρ) can not be measured directly. The evaluation of these state variables can be only performed by extrapolation from the reaction products to the disassembling system. It can be based on the study of following three aspects of the reaction products: (i) the shapes of the energy spectra from nuclear collision remnants [4,52,53,58], (ii) double isotopic yield ratio of emitted particles [27,28,59–62], and (iii) population ratio of excited states [60, 101]. These methods are described in this section, with the emphasis on the two first, which were used for the determination of the nuclear matter temperature. It should be noted that the interpretation of the caloric curve depends on the system's pressure (p) and density (ρ). However, neither p nor ρ are known experimentally. Therefore, the construction and interpretation of the caloric curve is based on other quantities, e.g. temperature of nuclear

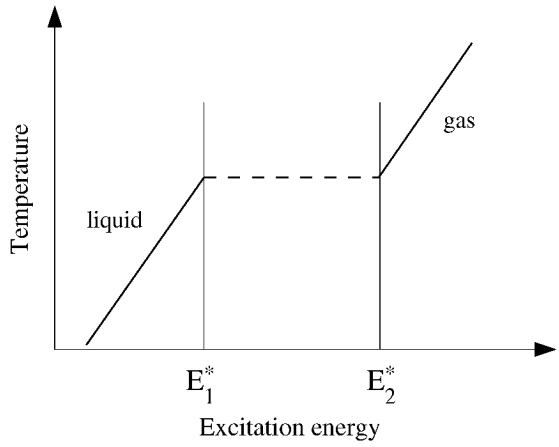

Figure 2.7. The schematic view of the caloric curve for the first order liquid-gas phase transition. For the explanation see text.

matter and excitation energy of the system.

2.3.1 Determination of the temperature from the fragments kinetic energy spectra

The slope of the particles kinetic energy spectra, assuming their Maxwellian distribution, is sensitive to the initial temperature of emitting source (T). The temperature can be evaluated by fitting to the kinetic energy spectra of fragments, in the center of mass coordinate system of the emitting source, the following Maxwellian function:

$$Y(E_{c.m}) \sim N \cdot \sqrt{E_{c.m.}} \cdot e^{-(E_{c.m.}/T)}, \tag{2.1}$$

where N is an overall normalization constant. After transformation of the Eq. 2.1 into the laboratory coordinate system, one obtains [58]:

$$\frac{d^2Y}{d\Omega dE} = N(E_{lab}/E_{c.m})^{1/2}(E_{c.m.} - B)^{1/2} \cdot e^{-((E_{c.m.}-B)/T)}, \tag{2.2}$$

where:

$$E_{c.m.} = E_{lab} + \tfrac{1}{2}A_f\beta^2 - 2[E_{lab}\tfrac{1}{2}A_f\beta^2]^{1/2}cos\Theta, \tag{2.3}$$

and E_{lab} is a fragment kinetic energy in the laboratory coordinate system, B is Coulomb barrier energy, A_f is the fragment mass, $\beta = v/c$, where v is the speed of remnant fragment recoiling along beam direction, c is the speed of light in vacuum, and Θ is the emission angle with the respect to the beam direction in the laboratory system.

As have been already observed in Refs. [4,52,53] energy spectra of emitted fragments at forward angles can be described by the Maxwellian distribution with rather flat slopes, in contrast to the nearly Gaussian shape observed at backward angles. It may be explained by different reaction mechanisms which are responsible for the fragments emission. During the first, fast stage of the reaction mainly light energetic particles are emitted in the direction strongly correlated with the beam direction (i.e. forward). Whereas during the second, slow stage of the reaction the equilibrated nucleus evaporates low energy elements isotropically. Therefore temperature obtained by fitting the Eg. 2.2 to the energy spectra of emitted fragments at various angles may not only be an evidence of the phase transition, but also may give information about the reaction mechanism.

2.3.2 Determination of the temperature from the double isotope yield ratio

One of the temperature determination methods relies on the measurement of the double ratio of isotopes yields, where the isotopes are produced in either particle-nuclei or nuclei-nuclei interactions. In this method the nuclear matter temperature can be found from the following equation proposed by Albergo et al. [59]:

$$T_{app} = \frac{B}{ln(a \cdot R_{app})}, \tag{2.4}$$

where a is a statistical factor, B is a combination of binding energies, and R_{app} is fragment yields ratio. The a depends on the statistical weights of the ground state nuclear spin $S(A, Z)$ of isotope with mass A and charge Z:

$$a = \frac{\Big[2S(A_2, Z_2) + 1\Big] / \Big[2S(A_2 + \Delta A, Z_2 + \Delta Z) + 1\Big]}{\Big[2S(A_1, Z_1) + 1\Big] / \Big[2S(A_1 + \Delta A, Z_1 + \Delta Z) + 1\Big]} \left(\frac{A_2/(A_2 + \Delta A_2)}{A_1/(A_1 + \Delta A_1)}\right)^{\eta}, \tag{2.5}$$

where the exponent η arises from the integration over the energy spectrum and is equal to 1.5 for the volume emission characterized by the Maxwellian distribution [28, 102]. The parameter B is a combination of binding energies ($BE(Z, A)$) of involved nuclei with mass A and charge Z:

$$\begin{aligned} B = {} & BE(A_1, Z_1) - BE(A_1 + \Delta A, Z_1 + \Delta Z) \\ & - BE(A_2, Z_2) - BE(A_2 + \Delta A, Z_2 + \Delta Z). \end{aligned} \tag{2.6}$$

The R_{app} parameter is measured ground state fragment yield ratio, defined as:

$$R_{app} = \frac{Y_a(A_1, Z_1)/Y_b(A_1 + \Delta A, Z_1 + \Delta Z)}{Y_c(A_2, Z_2)/Y_d(A_2 + \Delta A, Z_2 + \Delta Z)}, \tag{2.7}$$

where $Y(A_1, Z_1)$ and $Y(A_2, Z_2)$ are isotope yields. In order to cancel the nucleon chemical potential terms, the mass number differences of isotope pairs $(A_1, Z_1)/(A_1 + \Delta A, Z_1 + \Delta Z)$ must be the same as the mass number differences of isotope pair $(A_2, Z_2)/(A_2 + \Delta A, Z_2 + \Delta Z)$.

In Eq. 2.4 the cumulative effect of the sequential decays of unstable nuclei and some other processes which can occur after the system disintegration, is not taken into account. Therefore Tsang et al. [28] have defined for each double isotope ratio a correction factor κ by the following relation:

$$R_{app} = \kappa R_0, \tag{2.8}$$

where R_{app} (R_0) is the measured (equilibrium) value of the double isotope ratio. This factor can be only determined by examination of a large number of double ratio thermometers. After taking κ factor into account the temperature T_0 can be obtained from the following equation:

$$\frac{1}{T_{app}} = \frac{1}{T_0} + \frac{ln\kappa}{B}, \tag{2.9}$$

where B is the binding energy parameter defined in Eq. 2.4, T_{app} is the temperature obtained in the experiment and T_0 is the temperature of equilibrated system.

The double isotope yield ratio method can be used under following assumptions [103]:

1. The free nucleons and composite fragments are contained within a certain volume V at a temperature T.
2. The Maxwellian statistics is valid.

3. The system is in the chemical and thermal equilibrium.
4. The experimental yield of fragments is proportional to their density inside the volume V.
5. All observed fragments derive from the single source.
6. The observed isotopes are in their ground states.

2.3.3 Determination of the temperature from the population ratio of excited states

The third method of the determination of the nuclear matter temperature is based on the ratio of the population of excited states of a given isotope. In this method the temperature (T_{app}) is deduced from the following equation [7, 104]:

$$T_{app} = \frac{E_i^* - E_j^*}{ln(aR_{app})}, \tag{2.10}$$

where a is a ratio of spin factor of two states i and j of a given isotope:

$$a = \frac{2J_i + 1}{2J_j + 1}, \tag{2.11}$$

$R_{app} = Y_i/Y_j$ is the ratio of the yields of two states i and j, and E_i^* and E_j^* are the excitation energies.

Similar to the temperature obtained from double isotope yield ratio method, "apparent" temperature obtained from Eg. 2.10 requires correction for secondary decay of excited fragments. This correction can be minimized by choosing ratios characterized by large $\Delta E = E_i^* - E_j^*$.

Chapter 3

Apparatus

The PISA experimental setup consists of various types of detectors: Bragg Curve Detector (BCD), microchannelplate (MCPD), silicon and phoswich detector. Each of them was used for the detection of various particles in the different range of energy. The BCDs, MCPDs and cooled silicon detectors were intended for the identification of the intermediate mass fragments (IMFs) in low energy range (0.5–6 MeV/A), whereas silicon and phoswich detectors were intended for the detection of helium, lithium, beryllium and boron isotopes in high energy range (above 6 MeV/A). The MCPDs served for the time-of-flight measurements (TOF). All types of the PISA experiment detectors with the range of energy and charge (Z) of measured particles are presented in Tab. 3.1.

Detector	Range of energy (MeV/A)	Range of charge Z
MCPD(TOF)	0.5–6	3–16
BCD	0.5–6	3–16
silicon detectors	$\geqslant 6$	2–5
phoswich	$\geqslant 6$	2–4
cooled silicon detectors	0.5–6	2–5

Table 3.1. The detectors used in the PISA experiment. The charge and energy range (MeV/A) are indicated.

Components of the PISA experimental setup are described in the following sections. Additionally, a brief overview of the COSY (**CO**oller **SY**nchrotron) accelerator facility is presented.

3.1 COSY facility

The Forschungszentrum Jülich accelerator facility started its operation in the end of 1993. It consists of few unpolarized ion sources (H_2^+, H^-, D^-), one polarized ion source (H^-), the injector cyclotron JULIC, injection beam line (100 m of length), and the COSY accumulation ring with a circumference of 184 meters. The injector cyclotron JULIC can accelerate the H^- ions up to momentum of 300 MeV/c.

The cooler synchrotron COSY, after stripping injection of H- and D-ions, delivers beams of protons and deuterons within the momentum range from 300 MeV/c to 3600 MeV/c. Ions stripping method is based on the charge exchange of the H- and D-ions over 20 ms with linearly decreasing closed orbit bump at the position of the stripped foil of H- and D-ions. Ions beam is available for internal and external experiments [105, 106]. The intensity of the polarized beam is about 20 μA at the source exit with a measured polarization of about 85%, whereas current

of the unpolarized H-ions is about 10 μA at the exit of the transfer beam line (before injection into the COSY ring) [105].

The COSY cooler ring is divided into 4 cardinal sections. There are 2 straight telescopic and 2 half circle bending sections. The first one contains 32 quadrupole magnets grouped in 8 families, whereas second one contains 24 quadruples grouped in 6 families. For fine adjustments of the beam 40 correction dipoles and 18 sextuple magnets are used [107].

Two systems of beam cooling are applied, namely: electron cooling and stochastic cooling. These methods are applied for accumulation of the beam (reducing the beam phase space volume). In the electron cooling method, an electron beam, moving with the same average velocity as proton beam, absorbs the kinetic energy of protons, whereas stochastic cooling is the process in which the deviations of nominal energy or position of particles in a beam are measured and corrected. The electron cooling system used in the COSY ring is applied up to proton momentum of 290 MeV/c, whereas the stochastic cooling is used in the momentum range from 1.5 to 3.6 GeV/c [105]. The beam cooling with electrons decreases the initial momentum spread $\Delta p/p$ from 10^{-3} to 10^{-4}.

At the end of 2003 the COSY facility hosted few internal (COSY-11, ANKE, EDDA and PISA) and external experiments (NESSI, TOF, GEM, JESSICA). The schematic layout of the COSY facility is presented in Fig. 3.1.

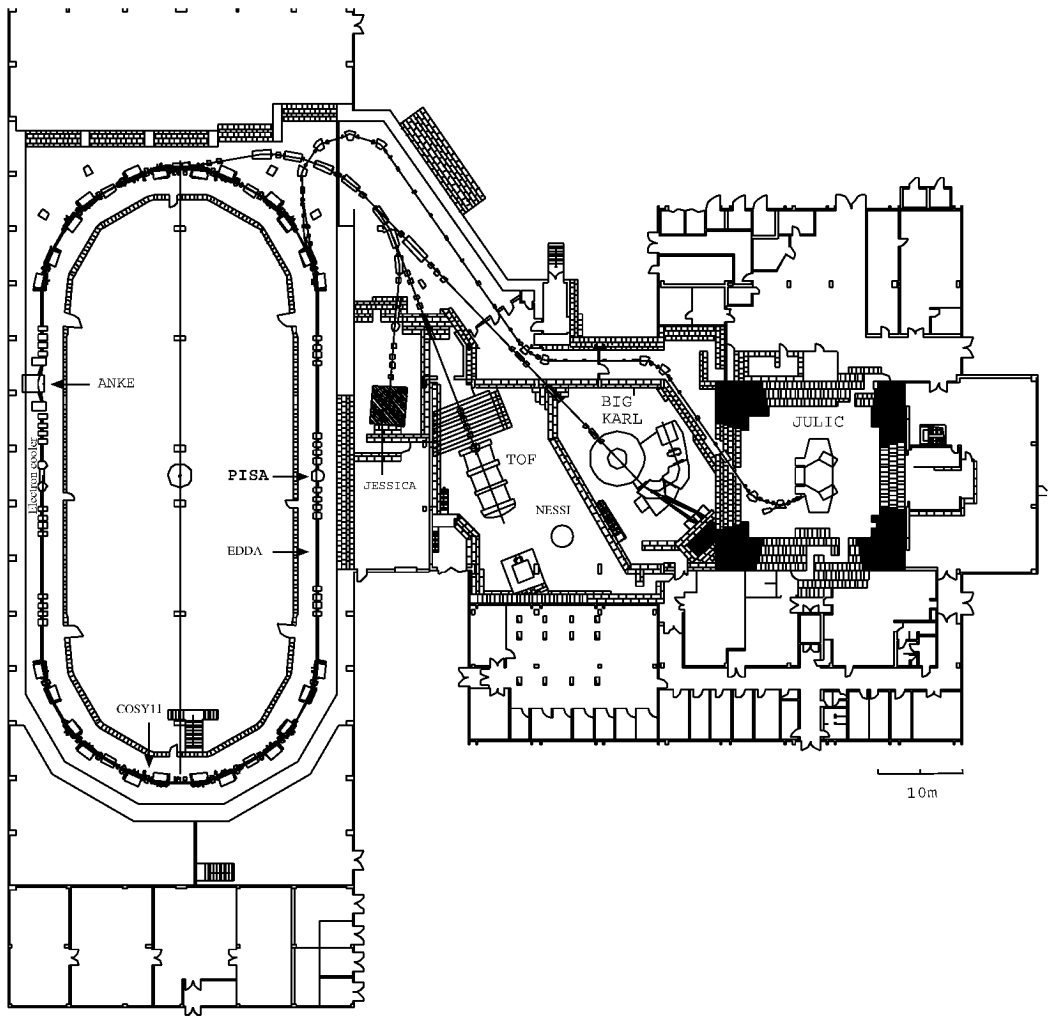

Figure 3.1. Schematic layout of the COSY facility. The places devoted to the internal and external experiments are indicated.

3.2 PISA experimental setup

The PISA experimental setup mounted on the internal beam of the COSY ring consists of the scattering chamber with target holding/changing mechanism and 8 detection arms connected to the scattering chamber. The arms are mounted in the horizontal plane at 15°, 20°, 35°, 50°, 65°, 80°, 100° and 120° with respect to the beam direction (cf. Fig 3.2 and Fig. 3.3 on the following page). The arms mounted at the most forward and backward directions (15° and 120°) consist of, in increasing distance from the target, two MCPDs working as a START and STOP for time-of-flight measurement, the BCD followed by 3 silicon detectors in a telescope geometry housed in the same vessel as BCD (silicon detectors are in isobutane atmosphere), and the double layer scintillation detector ("phoswich"). Each of the arm mounted at 35° and 100° consists of 4 silicon detectors in a telescope geometry, followed by the phoswich detector. The silicon detectors in those arms are cooled down to the temperature of –10 °C. The arms mounted at 20°, 50°, 65° and 80° consist of phoswich detectors only.

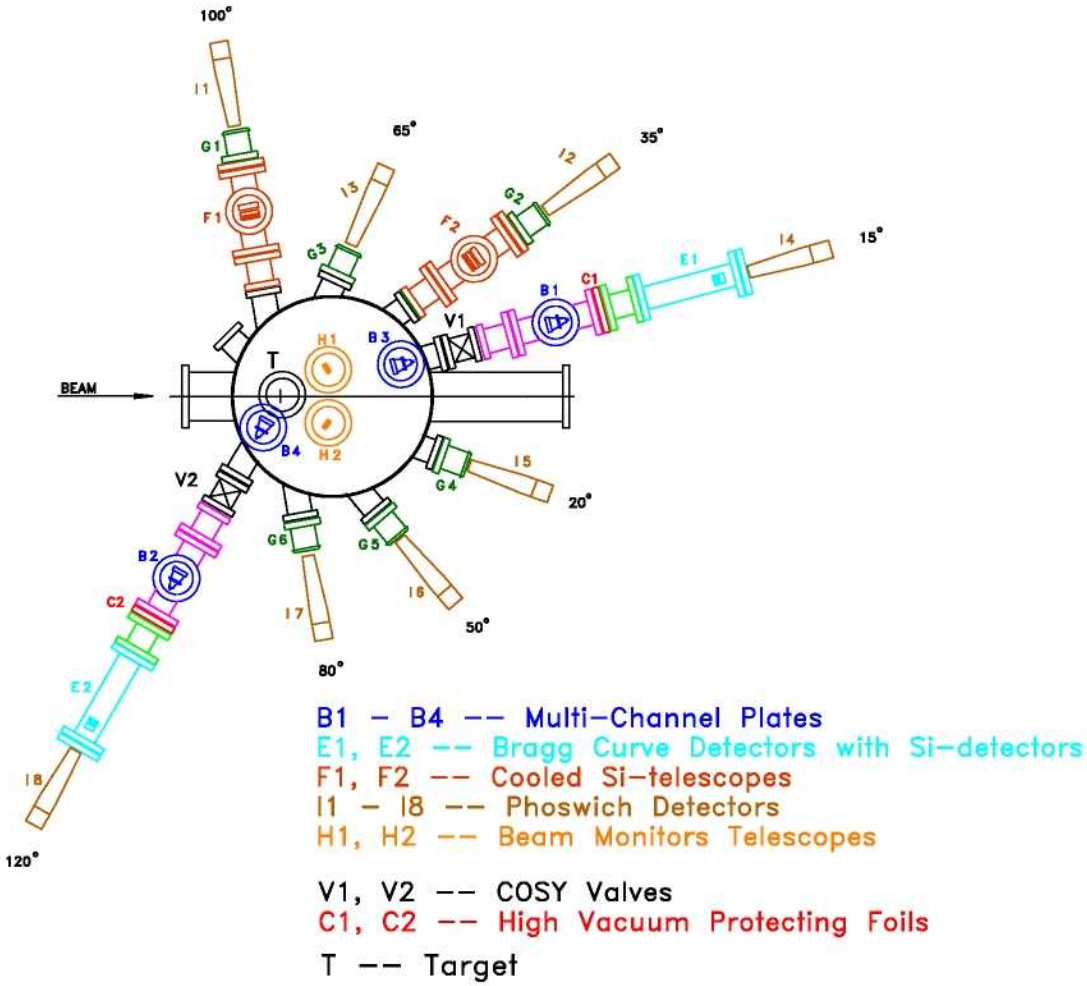

Figure 3.2. The experimental setup of the PISA apparatus. For the details see text.

A brief descriptions of the target-beam conditions and each of the detectors are presented in the following sections.

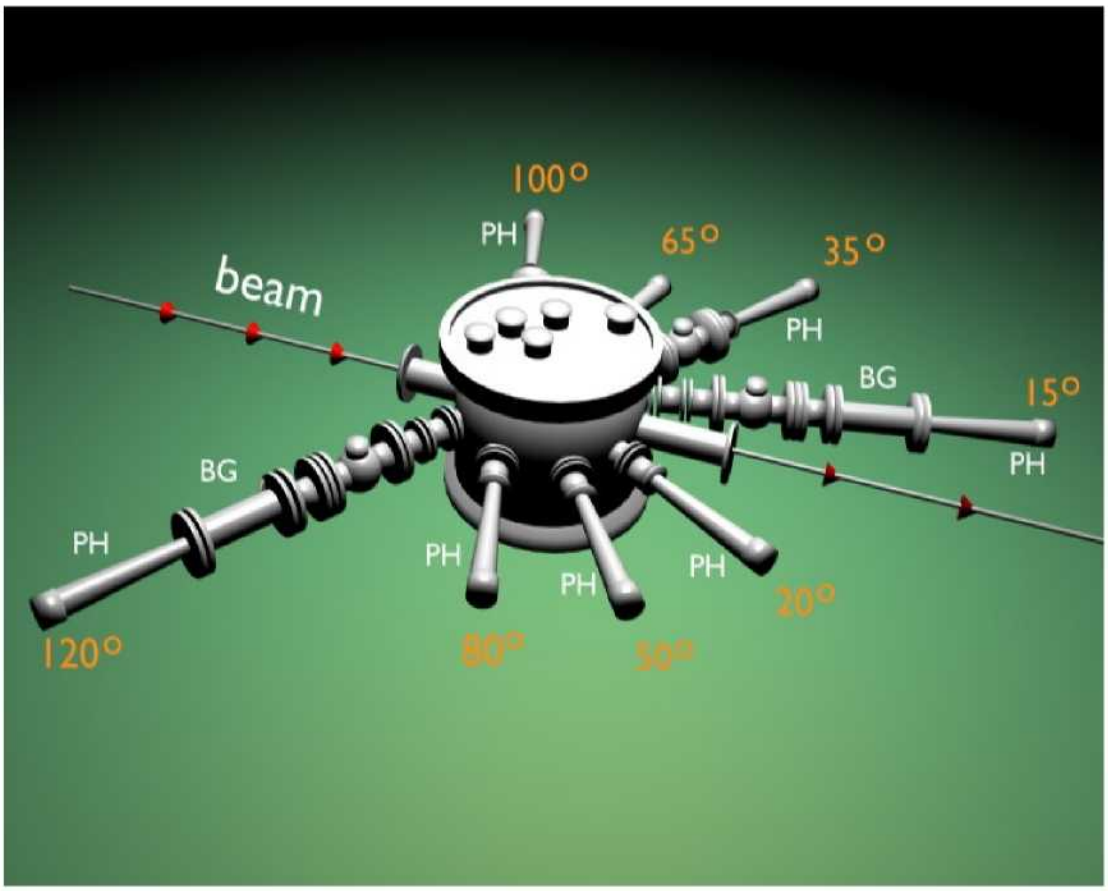

Figure 3.3. The experimental setup of the PISA apparatus; 3D presentation. For the details see text.

3.2.1 Target and beam

In order to obtain undistorted information about the reaction mechanisms the target with thickness less than 200 $\mu g/cm^2$ is required. Such thin target allows reaction products to escape from it with minimal energy loss and minimal distortion due to the scattering inside it (see appendix B on page 73). Therefore provides accurate insights into the physics of the proton-nucleus reactions which lead to the formation of the excited nucleus subsequently decaying and evaporating predominantly light particles such as n, p, and α particles. The low reaction rate due to the use of a thin targets is compensated by performing the experiment on circulating internal beam. Each of about 3×10^{10} protons stored in the COSY ring may pass through the target $10^4 - 10^5$ times before the beam is used up. Afterwards the ring is filled up again. The length of the cycle during the PISA experiment was about 28 s. It is a period between protons injection into the COSY ring and time when the beam is used up. It is named "spill". The dead time between cycles was approximately 2 s.

In order to compensate decreasing of the beam intensity during the cycle (due to the reaction of proton with target), thus also decreasing of the reaction rate, the geometrical overlapping of the target and the beam was adjusted in time. The purpose of the overlapping process was to keep the constant reaction rate during the cycle. The overlapping process begin after the beam reached the required energy and radii (see Fig. 3.4 on the facing page).

During the PISA experiment in October 2002 three thin targets were used: ^{nat}Ni (thickness: 150 $\mu g/cm^2$; strip target), ^{nat}C (thickness: 33 $\mu g/cm^2$; strip target) and ^{nat}Au (diameter: $\varnothing = 5$ μm; wire). Each of them was stretched at the fork-like shape holder. At the place devoted for the PISA target the expected horizontal and vertical radii of the beam are not larger

than about 22 and 12 mm, respectively [108]. These dimensions correspond to the beam size just after injection to the COSY accumulation ring, and before acceleration. After acceleration the beam dimensions shrink to size smaller than the horizontal size of the target holder, approximately to 1/4 of the original size of the horizontal and vertical radii. The scheme of holder and beam target geometry is shown in Figs. 3.4 and 3.5.

The horizontal target position with respect to the scattering chamber geometry is shown in Fig. 3.2 on page 15.

All strip target materials were prepared in Helmholtz - Institut für Strahlen und Kernphysik (ISKP), Rheinische Friedrich-Wilhelms-Universität Bonn, whereas the gold wire was manufactured by the Goodfellow Corporation.

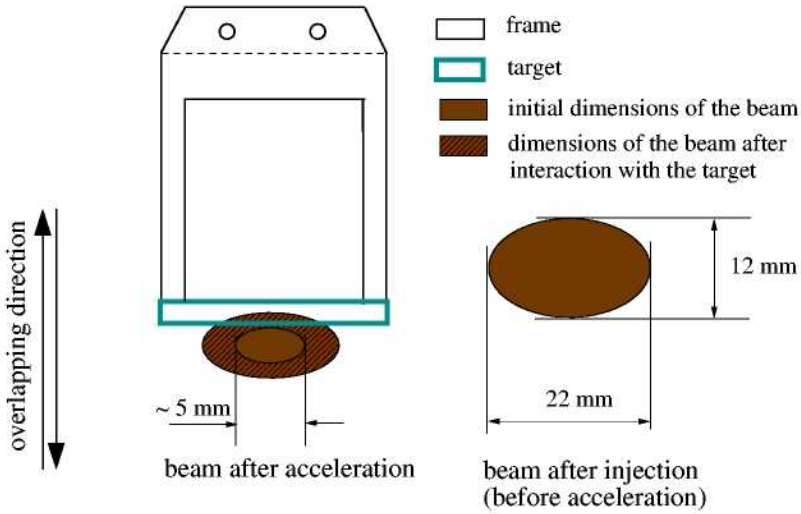

Figure 3.4. The horizontal and vertical beam dimensions at various phases of the spill at the place in the COSY ring devoted to the PISA experiment.

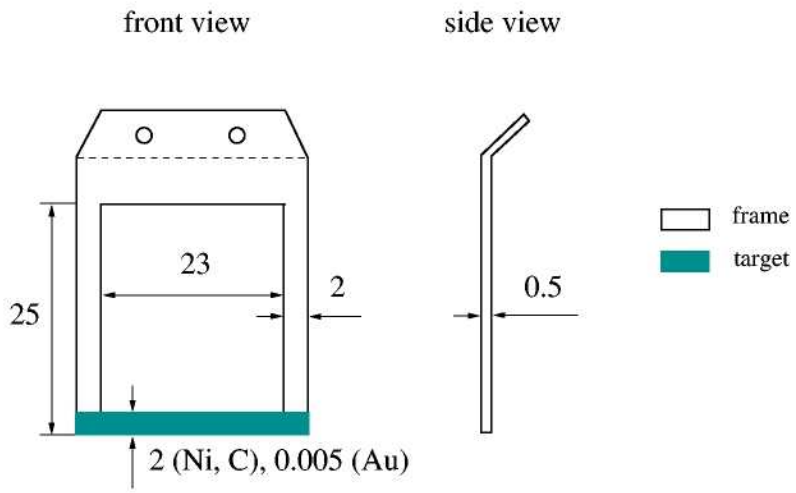

Figure 3.5. Shape of the target frame (dimensions are given in mm).

3.2.2 Microchannelplate detector (MCPD)

For the time-of-flight measurement two detectors based on the microchannelplate (MCP) were used. The first one, mounted in the scattering chamber, serves as a "start" detector, whereas

the second one, mounted inside the arm, 515 mm away from the start detector gives the "stop" signal (cf. Fig. 3.2 on page 15 and Fig. 3.3 on page 16). The layers of MCPs are connected in the Chevron configuration. The construction of the MCPD is shown in Fig. 3.6.

The particles which pass through the thin carbon foil (15–20 $\mu g/cm^2$) knock out δ electrons which are accelerated by the electric fields towards microchannelplates. These fields are applied between the foil and the accelerating grid, and between accelerating grid and the MCP itself. In order to get the best value of the electron multiplication factor ($\sim 10^7$) the following voltages were applied: –3000 V at the carbon foil, –2700 V at the accelerating grid and first layer of MCP (V2), and –300 V at the second layer of MCP (V3). The MCPs were manufactured by the Galileo Corporation.

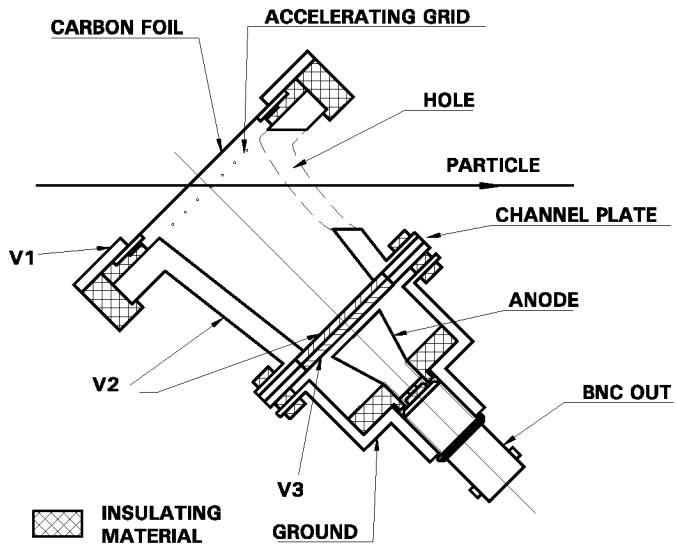

Figure 3.6. The scheme of the MCPDs (start/stop) used in the PISA experiment [109].

3.2.3 Bragg Curve Detector (BCD)

The Bragg Curve Detectors (BCDs) used in the PISA experiment were used for the detection of the low energy range (0.5–6 MeV/A) intermediate mass fragments (IMFs) produced in proton-nuclei collisions. The low energy detection threshold is one of the main advantages of the BCDs. Therefore the evaporation spectra of charged particles can be explored below the Coulomb barrier.

The BCD, proposed by Schiessl at al. [110], is an ionization chamber, with electric field parallel to the direction of incoming particles. It is composed of two foils (cathode and anode) and Frish grid placed between them. Frish grid has a value of the potential between anode and cathode potentials, and serves for the screening of the anode from positive charged ions released during ionization. Schematic view of the BCD is presented in Fig. 3.7 on the next page.

The passage of charged particles through the matter can be, in general, characterized by two major mechanisms, namely: (i) loss of energy, and (ii) deflection of a particle from its primary direction. Except for highly relativistic particles, ionization is the main electromagnetic contribution to the energy loss for charged particles. The energy loss (dE/dx) due to ionization is given by the Bethe-Bloch formula [111–113]. The dE/dx increases slowly along the particle path, because the amount of the energy which can be transfered in a single collision is only a

small portion of the particle kinetic energy. When the remaining energy of a particle is small the dE/dx increases rapidly forming so called Bragg Peak (BP) corresponding to the maximum of the ionization. The value of the maximum of the energy loss of ions in a stopping medium scales approximately with charge (Z) of ions. Therefore the BCD can be applied for the identification of the atomic number of the particles. Apart the charge dependence, the mass dependence is also observed in the stopping curve (called Bragg Curve (BC)). This can not be explained by simple application of the Bethe-Bloch formula. It is the second order correction, and depends on the details of the detector construction as discussed widely by Shenhav and Stelzer [114].

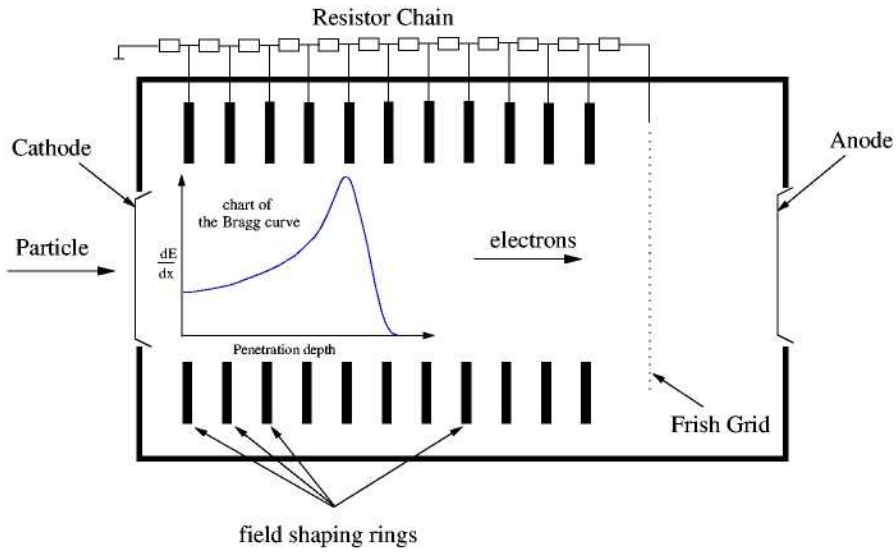

Figure 3.7. Schematic layout of the Bragg Curve Detector (BCD). A typical Bragg curve is shown. It presents variation of dE/dx as a function of the penetration depth of the particle inside the BCD volume.

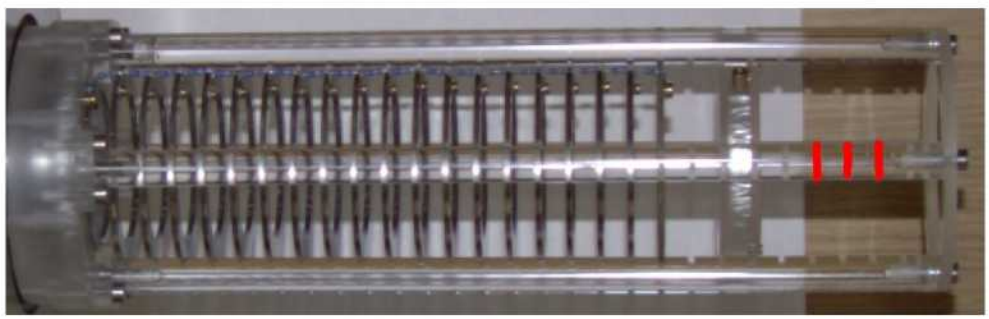

Figure 3.8. Photo of the BCD used in the PISA experiment. Red straight lines in right side of the BCD indicate the places designed for the silicon detectors.

The charged particles enter the BCD through the cathode foil (entrance window) and ionize the gas. The electrons released during ionization drift in the electric field, across the Frish grid, to the anode. They form the anode current. Due to the fact that velocities of detected charged particles are greater then velocities of released electrons, the electrons reach the anode in opposite order than they were released. Therefore the anode signal is a mirror image of the original BC (see Fig. 6.4(a) on page 36).

Each of the BCD used in the PISA experiment is constructed as a cylinder limited by the

grounded cathode (being simultaneously the entrance window), and by the anode. The last one is 218 mm away from the cathode. The cathode window is supported from the outside by the mesh of 50 μm diameter tungsten wires. The distances between neighboring wires are about 5 mm. The cathode and anode are made from 3.5 μm thick, one side metalized mylar foils. The Frish grid is a mesh of 20 μm tungsten wires, coated with gold, with distance between neighboring wires of about 1 mm. It is positioned between cathode and anode, 18 mm away from the anode. The homogeneous electric field between the cathode and Frish grid is produced by several stainless potential rings. All internal parts of the detector are mounted on an isolating skeleton made of plexiglass. The BCDs were filled with 99.9% purity isobutane gas at pressure of 200 mbar. The gas was continuously replaced. The cathode is grounded to the detector housing, whereas the Frish grid and the anode are kept at positive potentials. The possibilities of changing the applied voltages and continuous replacement of the gas cause that the BCD is practically not subjected to the radiation damages, and can be easily adjusted to the specific experimental conditions. The main parameters of the BCD used in the PISA experiment are presented in Tab. 3.2.

Parameter	Value
Active volume (Cathode to Frish grid distance)	200 mm
Width of the gap between Frish grid and anode	18 mm
Cathode voltage	grounded
Cathode supporting mesh	mesh of tungsten wire (⌀ 50 μm)
	distance between wires (5 mm)
Frish grid voltage	2400 V
Anode voltage	2900 V
Number of field shaping rings	19
Frish grid	mesh of gold coated tungsten wire (⌀ 20 μm)
	distance between wires (1 mm)
Cathode	aluminized mylar foil (3.5 μm)
Anode	aluminized mylar foil (3.5 μm)
Type of gas	isobutane (99.9% purity)
Pressure	200 mbar

Table 3.2. Main parameters of the BCD used in the PISA experiment.

In classical method of the read out of the BCD, two spectroscopy amplifiers with different time shaping constant are used. The amplifier with short shaping time gives an output signal which is proportional to the height of the BP, whereas the amplifier with long shaping time constant gives an output signal being proportional to the energy deposited by the particle in the BCD volume. However, this method does not allow to reproduce accurately shape of the Bragg curve. Therefore in the PISA experiment the anode signal is fed to the specially designed preamplifier (PA) [115,116] with two different outputs. First one, which reflects the anode current, is sampled and coded by the Flash ADC (C.A.E.N. Model V729A module [117]). Sampling is made at the rate of 10 megasamples/s (10 MHz frequency), and coding on 200 channels. The second output gives the signal amplitude which reflects the total collected charge. This method provides a new possibilities in further analysis of the Bragg curve, beyond the approaches applied previously.

The BCDs used in the PISA experiment were designed and manufactured in M. Smoluchowski Institute of Physics, Jagiellonian University, Cracow, Poland and H. Niewodniczański Institute of Nuclear Physics, Cracow, Poland. Successful tests of BCDs were performed in: (i) Heavy Ion Laboratory, Warsaw University, Warsaw, Poland, (ii) Instituto Nazionale Di Fisica Nucleare, Labolatori Nazionali Del Sud, Catania, Italia, and (iii) iThemba LABS, Somerset West, South Africa [109].

The detailed description of the BCD used in the PISA experiment is given in Ref. [116].

3.2.4 Semiconductor detector

The silicon and germanium are the most appropriate materials for semiconductor detectors. The minimum energy to crate an electron–hole pair are only 3.81 and 2.96 eV for silicon and germanium, respectively, at temperature of 77 K (3.62 eV for silicon at 300 K). This value is about 10 times smaller than the energy required for electron–ion pair creation in gases. Similarly to the BCD (in general, to ionization chamber) applied electric field "drifts" the electrons and holes (electron–ions pairs in ionization chamber) towards the surface where they are collected. The disadvantage of the semiconductor detectors is their sensitivity to the radiation damages, in contrast to the ionization chamber (cf. section 3.2.3 on page 18).

In the PISA experiment several silicons detectors were used: (i) three silicon detectors, in the telescope configuration, mounted inside each vessel of the BCD, in the isobutane atmosphere, and (ii) telescope of four silicon detectors mounted at 35° and 100° closed in high vacuum area, and cooled down to the temperature of –10 °C. Although the silicon detector, in contrast to the germanium one, does not need to be cooled down for its correct operation, the decreasing of temperature results in lower leakage of current and in reducing noise. In case of the silicon detectors used in the PISA experiment decreasing the temperature of about 10 K suppresses noise of factor 2.

The silicon detectors used in the PISA experiment were assigned for the detection of helium, lithium, beryllium and boron isotopes in both low (0.5–6 MeV/A; the cooled down silicon detectors), and high energy range ($\geqslant$ 6 MeV/A; detectors mounted behind the BCD).

The thicknesses and dimensions of silicon detectors are presented in Tab. 3.3. The cooled down silicon detectors are totally depleted surface barrier detectors.

15° behind BCD μm (⌀ mm)	35° cooled μm (⌀ mm)	100° cooled μm (⌀ mm)	120° behind BCD μm (⌀ mm)	beam monitors μm (⌀ mm)
85 (30)	50 (8)	19 (11)	107 (30)	350 (5)
315 (30)	100 (8)	50 (8)	293 (30)	350 (5)
5400 (30)	400 (8)	100 (8)	3500 (30)	
	3000 (8)	400 (8)		

Table 3.3. Thicknesses and dimensions of silicon detectors used in the PISA experiment. All thicknesses are given in μm. In the parenthesis diameters in mm are shown. The angles are given with the respect to the beam direction.

The example of mass identification spectra obtained with semiconductor detectors used in the PISA experiment are presented in appendix C on page 77.

3.2.5 Phoswich detector

The phoswich detectors (acronym of PHOSphor sandWICH technique [118]) were used for the measurement of the hydrogen and helium isotopes with energies $\geqslant$ 6 MeV/A. Phoswich detectors were mounted as the last detectors at each of the eight detection arms.

The phoswich detector is usually composed of two joined scintillators with different decay time constants. The fast (slow) front scintillator is usually thin ($\sim$ 1–2 mm) and gives dE/dx information, whereas the slow (fast) rear scintillator is relatively thick to provide the full energy signal. The light from both scintillators is collected by the photomultiplier tube connected to the last scintillator. The identification of the particle is based on the pulse shape discrimination method (PSD). The PSD method is based on the correlation between partial integrals of the signal at different time ($\Delta E - E$ method; cf. Fig. 3.9 on the next page).

Phoswich detectors used in the PISA experiment have been manufactured by the Bicron Corporation. The thin (1 mm), slow (940 ns decay time) scintillator – CaF_2(Eu) crystal is

connected to 25 mm diameter face of fast plastic scintillator – BC-412 with a 3.3 ns decay time constant. The BC-412 is a hexagonal rod extending from 25 mm to 425 mm (edge to edge) then tapering to 38 mm diameter, followed by Hamamatsu HTV R2060 photomultiplier tube. The total length of BC-412 is equal to 301 mm. The schematic view of the phoswich detector used in the PISA experiment is shown in Fig. 3.10.

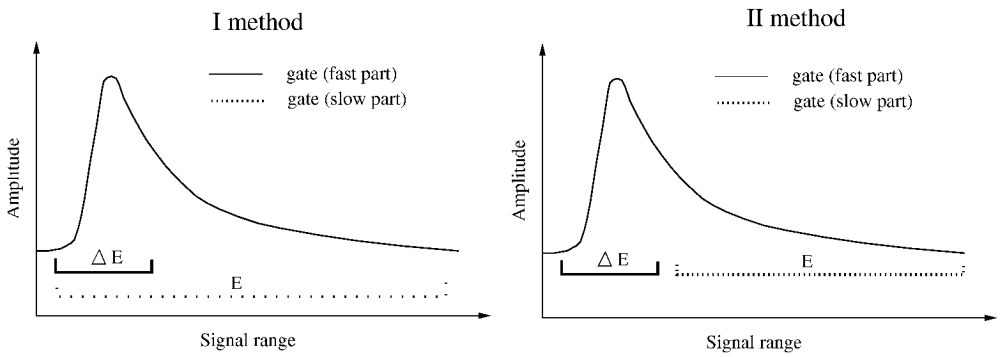

Figure 3.9. Pulse shape analysis of the phoswich detector signal. Two methods are presented.

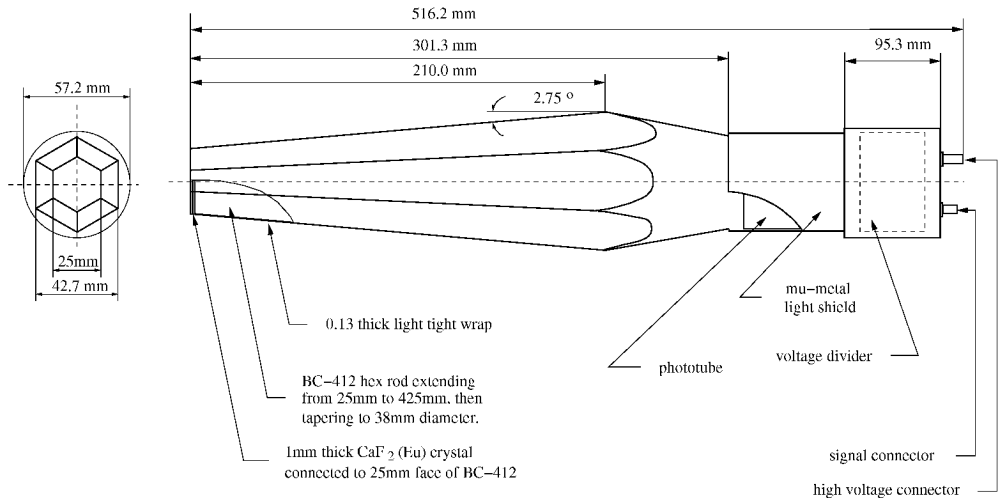

Figure 3.10. The schematic view of the phoswich detector manufactured by the Bicron Corporation and used in the PISA experiment. Front view – left, side view – right.

Chapter 4

Overview of the PISA experiment data acquisition system

A successful software is one that was used to do something undreamed of by its author.

S. C. Johnson

The PISA experiment's data acquisition system consists of two separate and independent parts: (i) the **E**xperimental **M**essage **S**pecification system (EMS[1]) developed at the Central Electronics Laboratory (ZEL - **Z**entral **L**abor für **E**lektronik), the Forschungszentrum Jülich and commonly used by different groups performing experiments at the COSY facility, and (ii) the software for on- and off-line analysis prepared specially for the PISA experiment. A brief description of EMS and the details of the PISA on- and off-line analysis packages are presented in this section.

4.1 Experimental Message Specification system

The EMS is a data acquisition system [120–122] developed at ZEL, the Forschungszentrum Jülich and used now in many experiments working at the COSY facility. The EMS is an object oriented, client-server based system establishing the communication on the application layer between the experimental control, the event builder and different front-end modular systems (CAMAC[2], FASTBUS, VME[3]). Connection of the front-end modular system is performed by transparent controllers with PCI compliant interface. During the PISA experiment performed in the 2002, this system allowed to collect up to 400 events per second[4]. The data recorded in the so called "cluster format" were later converted to the "event format" by an external program (cluster2event). The structure of the "event format" is described in chapter 4.1.1 on the next page. The created bunch of data can be redirected to various destinations such as computer hard discs, DLT[5], Exabyte[6] tapes or virtual computer's socket. The last one is mainly used during the on-line analysis.

[1] **E**xperimental **M**essage **S**pezification system according to **M**anufacturing **M**essage **S**pezification (MMS [119])

[2] **C**omputer **A**utomated **M**easurement **A**nd **C**ontrol

[3] **V**ersa **M**odule **E**urope: international 32-bit (64-bit) parallel computer bus standard [123]

[4] The limitation imposed by electronics circuit conditions.

[5] **D**igital **L**inear **T**ape. A serpentine technology introduced by Digital Equipment Corporation for tape backup/archive [124].

[6] The 8 mm video cassette recorder tape for computer data backup [124].

4.1.1 Structure of the event

The event is divided into two parts: the "header" and the "body". The header contains the following information: event size, event number, trigger number and number of subevents included in the event. The body consists of individual subevents specified in the header. The first two words of a subevent are: (i) the Instrumentary System (IS), which refers to a logically or physically grouped number of modules[7], and (ii) the number of data words inside subevent. The structure and encode methods of the individual subevent depend on the type of the module used. Each word of the event consists of four bytes. The structure of a hypothetical event is presented in Tab. 4.1 and in Fig. 4.1.

No.	Hypothetical value	Description	
0	12	event size	header
1	1	event number	
2	3	trigger type	
3	2	number of subevents	
4	9	IS number	body
5	4	number of data words	
6	24	32 bit data word (4 bytes)	
7	4	...	
8	1975	...	
9	7	IS number	
10	2	number of data words	
11	209	32 bit data word (4 bytes)	
12	20522	...	

Table 4.1. The structure of a hypothetical event with hypothetical values.

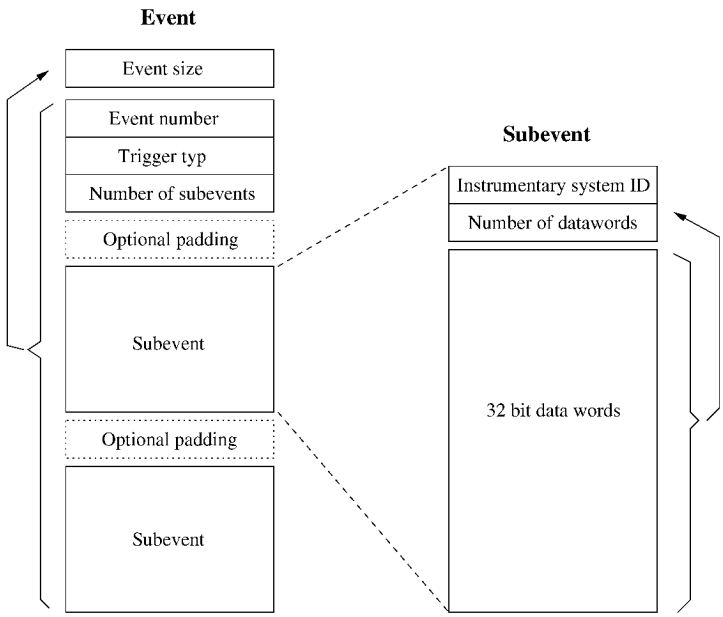

Figure 4.1. The structure of a hypothetical event. Fig. adapted from Ref. [125].

[7]The device designed for conversion of the analog signals from detectors to the digital signals acceptable by the data acquisition system

4.2 PISA software package

Among the programs used in the PISA data acquisition system (PDAQ) the following three are the most important: decoder, HistFiller and HistPresenter. They make a framework for other components of the PDAQ. Their short description, together with their abilities, methods of application and interdependencies (see Fig. 4.4 on page 28) is presented in chapters 4.2.1 to 4.2.3 on pages 25–28. The programs have been written in the object oriented C++ programming language [126], Tcl/Tk open source scripting language [127] and Bash script language [128]. The program package of the PISA software has been written from scratch and was continously developed in the framework of the presented PhD thesis.

The scheme of the data stream flow between the programs is presented in Fig. 4.2.

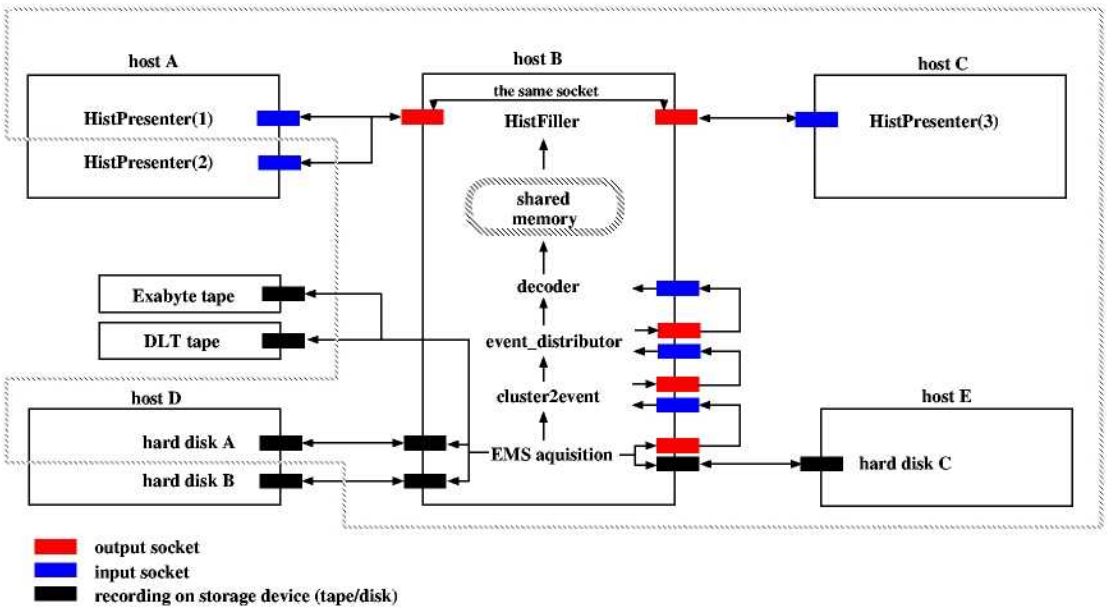

Figure 4.2. The scheme of the possible data stream flow between the PDAQ programs. The configuration used during the October 2002 data taking is indicated by dashed line.

4.2.1 Decoder program

The main goal of the decoder program is the data transformation from one coding system to another one. It also allows simultaneous access to encoded data by other programs using the shared memory[8] method. The decoder program can operate in two modes: on- or off-line. The scheme of the input-output stream flow in the decoder is shown in Fig. 4.3 on page 27.

As mentioned in chapter 4.1 on page 23, raw data can be simultaneously send by the EMS data acquisition system to various places. One of them can be a virtual socket on the host or remote computer (connected via network). The sockets may be viewed for network connections as attachment points in computer. In the on-line mode, the decoder attaches itself to a socket and

[8] "In computer programming, shared memory is a method by which program processes can exchange data more quickly than by reading and writing using the regular operating system services. For example, a client process may have data to pass to a server process that the server process is to modify and return to the client. Ordinarily, this would require the client writing to an output file (using the buffers of the operating system) and the server then reading that file as input from the buffer to its own work space. Using a designated area of shared memory, the data can be made directly accessible to both processes without having to use the system services. To put the data in shared memory, the client gets access to shared memory after checking a semaphore value, writes the data, and then resets the semaphore to signal to the server (which periodically checks shared memory for possible input) that data is waiting. In turn, the server process writes data back to the shared memory area, using the semaphore to indicate that data is ready to be read." [129]

waits for the data from the EMS data acquisition program. This is also called listening on the port [130]. If data appear on a listened socket, the decoder will start to process it and place data in required form, in required destination. There are two possible data forms: the "tree" structure derived from the ROOT software [131], and the raw ASCII[9] format. The possible destinations are: the shared memory or the hard disc. In the latter case, the data before writing on the disc are encapsulated in a wider structure, the so called "root file" [131]. The first destination (shared memory) is used mainly during the on-line mode, because the shared memory allows for easy exchange of the data between the decoder and external programs.

There is a fundamental difference between on- and off-line operating modes. During the on-line mode, the tree structure consists of only one entry (the event, see: Tab. 4.1 on page 24 and Fig. 4.1 on page 24) in a given time. The next event replaces the previous one. The reason of using such solution was to decrease the occupation of memory by unneeded events. In the off-line mode the events are appended to the existing tree. Also, in off-line mode apart from the creation of the "root file" (with the tree), the decoder can update the existing "root file" (update the existing tree).

In the on-line mode, the raw data (in the cluster format) can be fed to the decoder only via a socket, whereas in the off-line, mode the program is able to read the raw data either from disc file or from pipe[10].

The decoder program has a modular structure based on the object oriented C++ programming language [126]. In the frame of the decoder, a few specialized classes were designed. Some of them are connected with hardware modules: QDC (Charge Digital Converter), TDC (Time Digital Converter), ADC (Amplitude Digital Converter), FlashADC, Scaler and Pattern Unit. All these classes are derived from the global class Code. The short description of classes and their applications is given below:

1. **FlashADC** class
   This class is used for decoding of the data from the C.A.E.N.[11] Model V729A module. This module is a 4 channel 40 MHz ADC. "Its function is to convert and store in a buffer the input analog signals which belong to a programmable temporal window placed before or around a STOP signal." [117]. The signals from BCDs have been read by this module. It provides the information about the shape of the Bragg's signal.
2. **AQTDC** class (Amplitude, Charge and Time Digital Converter class)
   To this class belong 3 different modules with very similar type of decoding.
   - The C.A.E.N. Model V785, 32 channel peak sensing ADC module.
     "The model V785 is a 1-unit wide VME module housing 32 Peak Sensing Analog-to-Digital Conversion channel" [132]. Analog signals from all silicon detectors (including the monitor detectors), from "charge" output of the BCD's preamplifier [116], and also signals from the TAC (Time Amplitude Converter) module were fed to this module.
   - The C.A.E.N. Model V792, 32 channel QDC module [133].
     Signals from all 8 phoswich detectors were fed to it.
   - The C.A.E.N. Model V775, 32 channel TDC module.
     Signals from 4 MCPD belonging to the arms installed at 15° and 120°, with respect to the beam direction, were fed to it.
3. **ScalerV560E** class
   The class for decoding the data from the C.A.E.N. V560E module. "This is a 1-unit wide VME module provided with 16 independent 32-bit counting channels" [134].

[9] American Standard Code for Information Interchange

[10] A method for passing information from one computer process to another one. A named pipe is sometimes called a "FIFO" (first in, first out), because the first data written to the pipe is the first data that is read from it.

[11] Costruzioni Apparecchiature Elettroniche Nucleari S.p.A.

4. **ScalerV830** class
   The class for decoding the data from the C.A.E.N. V830 module. "This is a 1-unit wide VME module provided with 32 independent 32-bit counting channels" [135].
5. **V259E** class
   The class for decoding the data from the C.A.E.N. V259E module [136]. This is a 16 bit strobed multi-hit pattern unit. This module can store the input hit pattern readable via the VME bus.

In order to make the decoder program user's friendly, a frontend with the ncurses[12] library routines was written. A few screenshots of a frontend to the program are shown in Fig. A.1 on page 67.

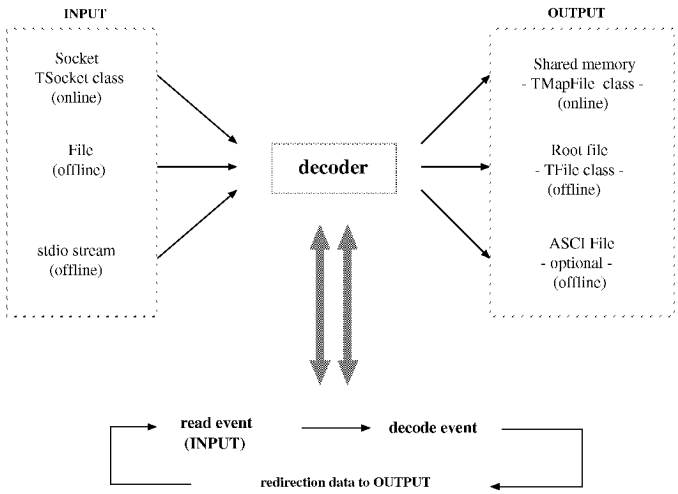

Figure 4.3. Input-output stream flow in the decoder program in on- and off-line operating modes. The classes derived from the ROOT software are also indicated.

4.2.2 HistFiller program

In flow of the processed data, the HistFiller program takes the intermediate position between the decoder and the HistPresenter. The main goals of this program are to create and fill the spectra and/or tree with the data delivered by the decoder program. The spectra present various correlations between the data. Similarly to the decoder program, the HistFiller can operate in two modes: on- and off-line. During the on-line operation the program looks for the data in shared memory, whereas in off-line mode, the data has to be read from a disc file. The created spectra can be visualized in the HistPresenter. The communication between the HistFiller and the HistPresenter is done via sockets. The HistFiller processes the data and attaches itself to a default socket on host computer and waits for the HistPresenter request. The differences between the on- and off-line modes are shown in Tab. 4.2.

	decoder		HistFiller	
	on-line mode	off-line mode	on-line mode	off-line mode
input from	TCP/IP socket	disc file or pipe	shared memory	disc file
output to	shared memory	disc file	memory	memory and/or disc
storage structure	tree	tree	histograms	tree or histograms

Table 4.2. The differences between on- and off-line modes of the decoder and the HistFiller programs.

[12]The ncurses is a library which gives the user a terminal independent method of updating character screens. It uses the terminfo format, supports pads, color, multiple highlights, forms characters and function-key mapping.

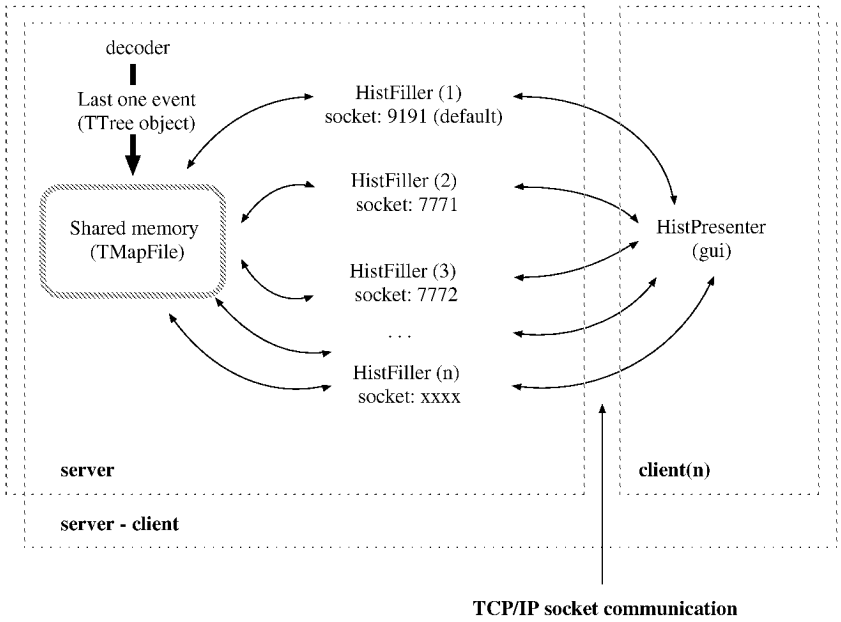

Figure 4.4. The structure of the PISA software and the relationships between the programs in the on-line operating mode. The numbers in parenthesis (**n** - HistFiller(**n**), client(**n**)) characterize possible parallel running copies of the HistFiller programs on the server, and various client computers with the HistPresenter.

4.2.3 HistPresenter program

This chapter presents the HistPresenter programs used mainly for the on-line (optionally also off-line) presentation of the collected spectra. However, it should be noted that the HistPresenter program has also other, more advanced abilities, like for example a creation of graphical cuts on spectra (determination of filling conditions of the spectra). The HistPresenter program is written in the C++ programming language [126] in the ROOT environment [131], with some libraries derived from Tcl/Tk, an open scripting language [127]. The program is divided into some sections (Start, MCP, Bragg, etc.) which in the further part of this chapter will be called "Tab". The spectra are created by the HistFiller program. The HistPresenter communicates with the HistFiller sending commands, which for example, request spectra, print, clear or save them (to a "root file"). The connection between the HistFiller and the HistPresenter is established by the socket communication (TCP/IP protocol - TSocket and TServerSocket classes derived from the ROOT software).

The Tabs which can be used in the HistFiller program are mainly associated with the detectors which were used during the experiment. Each Tab has options for printing, resetting, saving and updating (in a loop) of spectra available for use. The Tabs corresponding to the detectors are:

- **MCP** - microchannelplates (cf. Figs. A.3 to A.4 on pages 68–69),
- **Bragg** - Bragg curve detectors (cf. Fig. A.5 on page 69),
- **Silicon** - silicon detectors (cf. Fig. A.6 on page 70),
- **Phoswich** - phoswich detectors (cf. Fig. A.7 on page 70),
- **Monitor** - beam luminosity monitor detectors.

Additional Tabs:

- **Pattern Unit** - related to strobed multi-hit pattern unit module [136] (cf. Fig A.8 on page 71),
- **Scaler** - related to two scaler modules: 16-channel scaler [134] and 32-channel latching scaler [135] (cf. Fig. A.9 on page 71),

- **WhatUWant** - displays required spectrum or combination of any spectra (cf. Fig. A.10 on page 72). The previous knowledge about the existing histograms is not mandatory. The information about all existing spectra can be requested from the HistFiller program via this Tab,
- **Cut** - creates and modifies graphical cuts on selected histograms, sends cuts to the HistFiller program (cf. Fig. A.11 on page 72). The HistFiller fills the histograms with these cuts.

A few screenshots of the Tabs from the HistPresenter are presented in Figs. A.2 to A.11 on pages 68–72 in appendix A.

Chapter 5

Electronic setup

In the PISA experiment, standard NIM and VME electronics were used. The layout of the electronics circuit and the logic of connections are shown in Fig. 5.1 on the next page. The types of used VME modules together with methods of application are shown as well.

Four triggers (conditions) for the readout of the digitalizing modules were constructed. The first trigger was formed in the following way: (i) either couple MCPDs (under 15° or 120°), working in the coincidence mode, gave a signal, or (ii) the couple of the silicon detectors follow directly each other, regardless of number of arm where are mounted, were fired, or (iii) one of the phoswich detectors gave a signal. Second trigger was based on the BCDs. Irrespective which BCD gave a correct signal the condition number 2 was met. Third trigger was related to the monitor detectors working in the anti-coincidence mode. And the last one it was periodical, artificial impulse of 1 Hz frequency. The trigger conditions used in the PISA experiment are shown in Tab. 5.1.

Trigger No.	Conditions
1	$(MCP1\_15 \wedge MCP2\_15) \vee (MCP1\_120 \wedge MCP2\_120) \vee (S1 \wedge S2) \vee (S2 \wedge S3) \vee (S3 \wedge S4) \vee PH$
2	$BCD\_15 \vee BCD\_120$
3	$(ML1 \wedge \overline{ML2}) \vee (MR1 \wedge \overline{MR2})$
4	1 Hz - periodical artificial impulse

Table 5.1. The trigger conditions. MCP1_15 and MCP2_15 – microchannelplate start and stop at 15°, MCP1_120 and MCP2_120 – microchannelplate start and stop at 120°, S1, S2, S3, S4 – first, second, third and fourth silicon in telescopes independent from arm in which they are placed, ML1 and ML2 – monitor detectors (left side), MR1 and MR2 – monitor detectors (right side).

Various combinations of triggers were used for forming of the so called gates (signals) which were fed to the individual digitalizing modules. Start of the readout procedure was only permitted in the presence of a given gate. The gates has been constructed in the following way:

- In the presence of the signal gate formed from the trigger number 3, the amplitude digital converter module (Peak Sensing ADC - Model V785 [132]), which was used for monitor detectors, was read out.
- The readout of the signals from the amplitude digital converter module (ADC Model V795A [117]), used for both BCDs, was possible in the presence of the trigger number 1 or 2.
- Trigger number 1 allowed for the read out of the following modules:
  - two charge digital converter modules (QDC Model V793 [133]), serving all phoswich detectors,

- two amplitude digital converter modules, serving all silicon detectors and MCPDs (amplitude signal formed by time-to-amplitude converter (TAC)),
- time digital converter module (TDC Model V775 [137]), serving MCPDs.

• The 1 Hz artifical impulse was fed to the input gates of the scaler modules (Models V560 [134] and V830 [135]).

All digitalizing modules were produced by the C.A.E.N. Corporation.

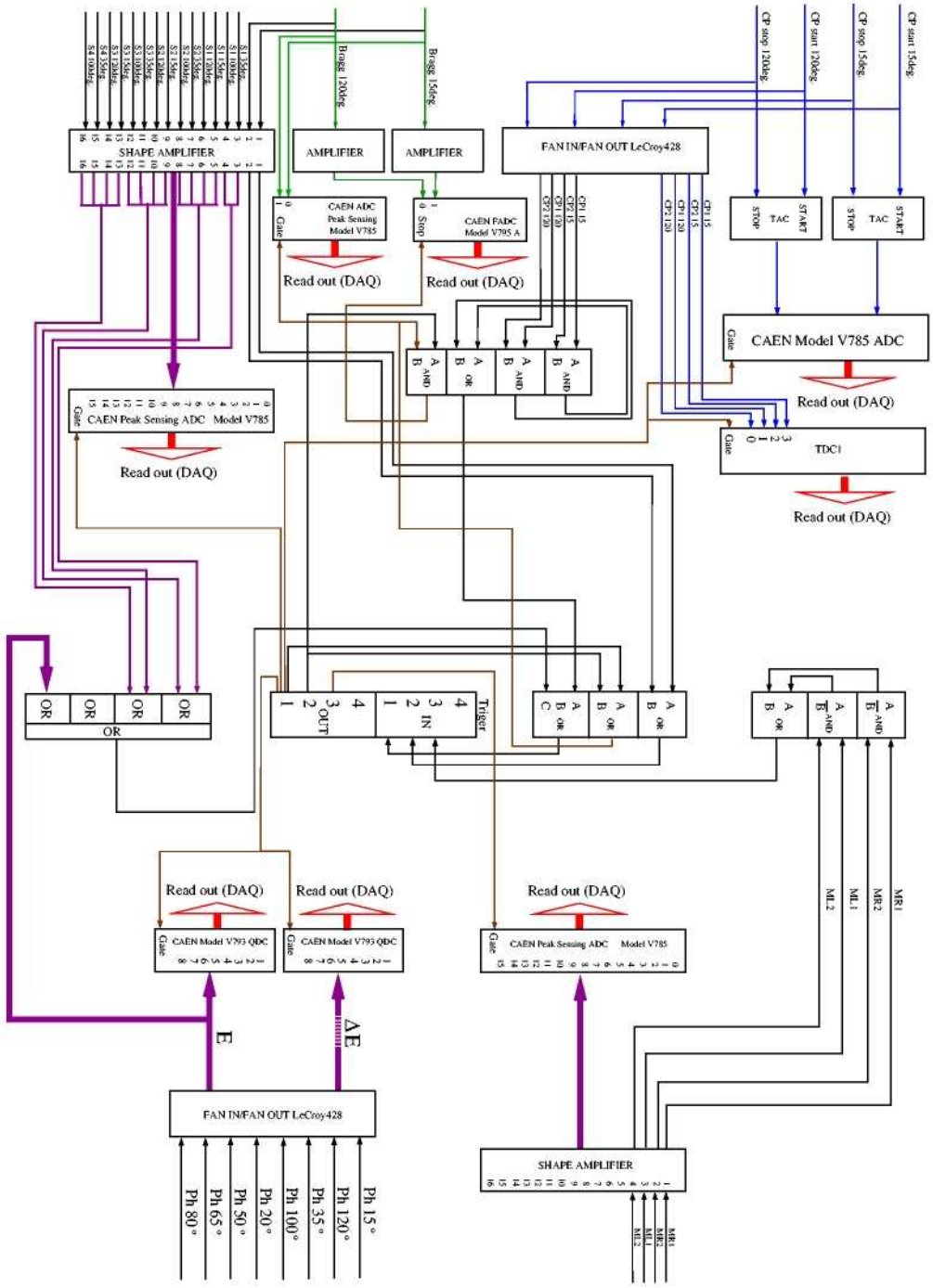

Figure 5.1. The simplified chart of the PISA electronics. Notation: S1–S4 – silicon detectors; CP – microchannelplates; Ph – phoswiches; MR – monitor right, ML – monitor left.

Chapter 6

Experimental procedures and data analysis

The identification of the intermediate mass fragments (IMFs; $3 \leqslant Z \leqslant 14$) produced in the interaction of 1.9 GeV protons with nickel (^{nat}Ni) has been a subject of interest. Energy spectra and angular distributions have been measured for isotopically separated elements. The identification of the emitted IMFs at 15° and 120° has been performed using BCDs and time-of-flight (TOF) technique. The BCDs were used for the charge identification, whereas the MCPDs together with BCDs for the mass identification. The details of the elements and isotopes identification are presented in this section. Determination of the temperature of excited nuclei by various methods, the comparison between nuclear matter thermometers, and the presentation of the obtained results in the energy-temperature diagram, the so called caloric curve (CC), are shown as well.

The analyzed data were collected during the experiment performed by the PISA collaboration in October 2002 at the COSY facility in the Forschungszentrum Jülich, Germany.

6.1 MCP detectors efficiency

The efficiency of the MCP detectors (MCPD) as a function of the kinetic energy and mass of the detected particles has been investigated.

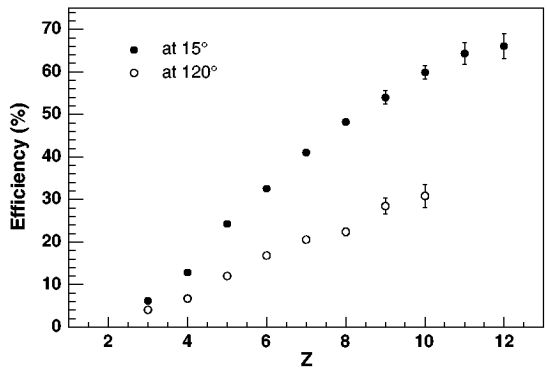

Figure 6.1. The efficiency of MCPs at 15° and 120° under assumption of 100% efficiency of the both BCDs.

The determination of the MCPD efficiency was performed assuming 100% efficiency of the BCD. It was defined as the number of particles detected by the BCD to the number of particles

detected by the MCPDs. The solid angles of both MCPD and the sticking of the particles in the foils between MCPD and BCD were taken into account. The solid angle is determined by the second MCPD (placed further away from the target; cf. Figs. 3.2 to 3.3 on pages 15–16). The second MCPD to BCD Frish grid solid angle ratio is equal to 0.34 ± 0.02. However the solid angle of the MCPD's housing is bigger than BCD one. Therefore particles observed inside the BCD should cross the MCPDs ("start" and "stop"). The efficiency of the MCPDs at 15° and 120° assuming 100% efficiency of the BCD is shown in Fig. 6.1 on the page before.

The efficiency of the MCPD varies from 6.65 ± 0.02 % to 59.87 ± 1.56 %, and from 4.32 ± 0.02 % to 30.80 ± 2.63 for $3 \leqslant Z \leqslant 10$, for 15° and 120°, respectively. The efficiency of the MCPD is a function of the charge of the detected particle and increases with increasing Z.

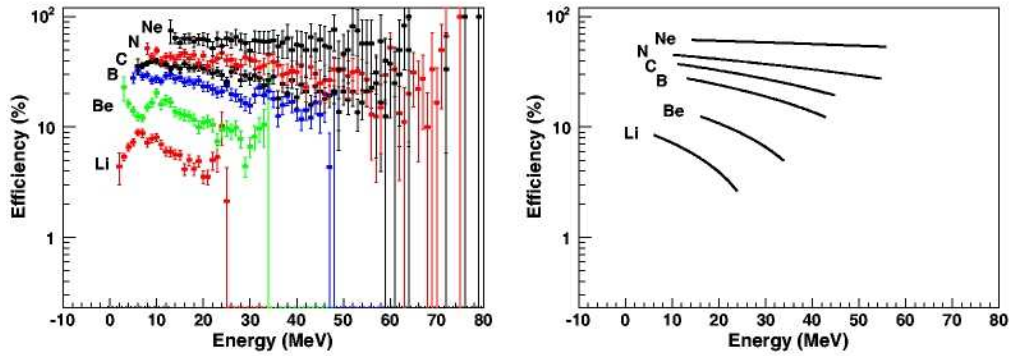

(a) MCPD at 15°

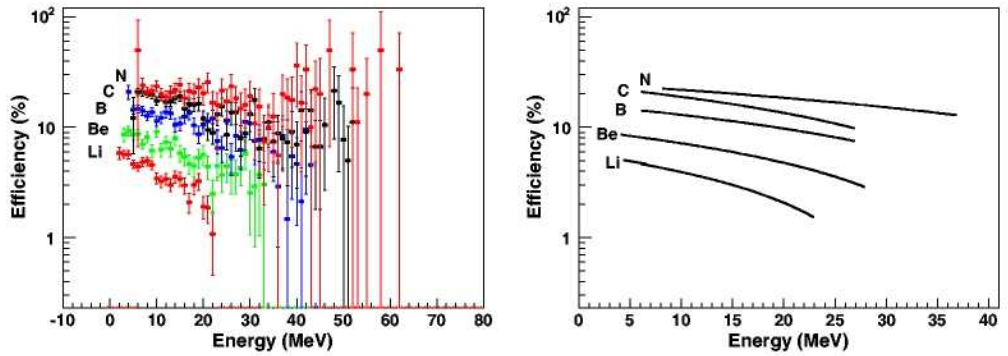

(b) MCPD at 120°

Figure 6.2. The efficiency of MCPDs as a function of the kinetic energy deposited inside the BCD volume assuming 100% efficiency of the BCD. The lines represent fit curves to the experimental data points.

The MCPD efficiency as a function of the energy deposited inside the BCD volume at 15° and 120° assuming 100% efficiency of the BCD is shown in Fig. 6.2. The lines in Figs. 6.2(a) and 6.2(b) are drawn only to guide the eyes, and represent fit curves to the experimental data points. The determination of the efficiency was performed for particles stopped inside the BCD volume. The efficiency of the MCPD for all particles decreases with increasing energy deposited inside the BCD or in general, with incident particle energy. The relationship between particles incident energy and energy deposited inside the BCD volume, obtained from the Geant4 [63] simulations, are shown in appendix B on page 73. The observed decreasing MCPD efficiency with energy and various slopes of the efficiency curves are effect of the three following facts: (i)

the energy loss dE/dx strongly decreases with increasing incident particle energy [138], (ii) the energy loss increases with increasing atomic and mass number of the incident particle [138], and (iii) the δ-electron production increases with increasing energy loss.

6.2 Bragg curve and microchannelplate detectors analysis

There is no excellent beauty that has not some strangeness in the proportion

Francis Bacon 1561–1626

6.2.1 Shape of the Bragg curve

A particle which crosses the BCD creates the ionization along its track. Electrons produced along the track drift through the Frish grid to the anode, where they are collected and observed as an anode current. The anode signal is amplified by specially designed preamplifier (PA) [115, 116] with two different outputs. The output signal from the PA, which reflects the anode current, is sampled by the Flash ADC (C.E.A.N. Model V729A module [117]). Sampling is made at the rate of 10 MHz and consists of 200 samples. As result one obtains the shape of the Bragg curve (BC). The shape of the BC can be characterized by the following parameters: the range of the particle (RG), the amplitude of the Bragg peak (BP), and the energy of the particle (E). The RG is associated to the depth of the particle's penetration inside the BCD volume. The BP corresponds to the maximum of the energy loss (maximal value of dE/dx) at the end of the particle's path, and is a direct measurement of the particle charge. The E is a kinetic energy deposited by the particle in the BCD volume and can be obtained from the area under the BC.

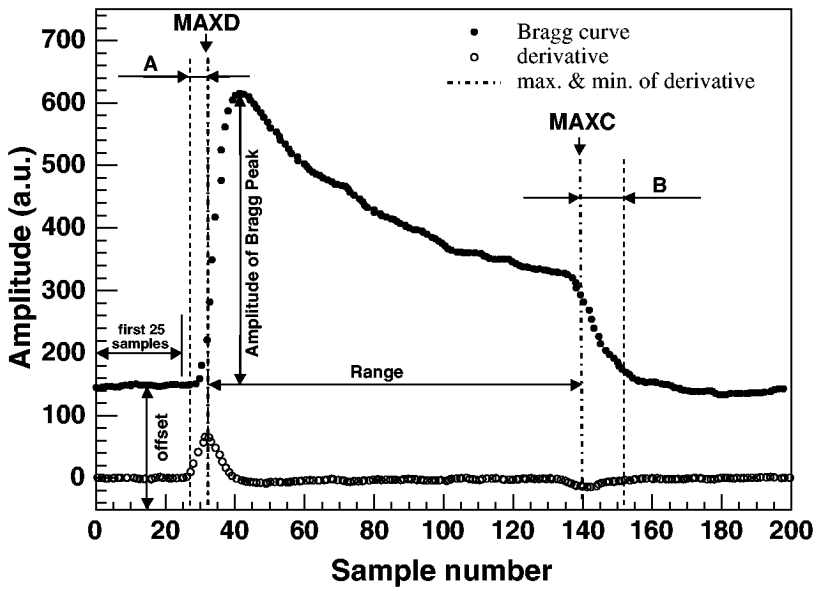

Figure 6.3. Example of the BC with marked parameters: range (RG) and amplitude of Bragg Peak (BP). The presented curve is a mirror image of the real curve (for explanation see section 3.2.3 on page 18). The derivatives of the BC are also presented. The areas "A", "B", positions of maximum (MAXD) and minimum (MAXC) values of the derivative are indicated – for details see text. The amplitude axis is chosen for the best presentation of the BC and its derivative.

A typical shape of the BC is presented in Fig. 6.3 on the preceding page. More examples are presented in Fig. 6.4, where BCs are created by lithium isotopes which sticked inside the BCD volume mounted at 15°. In Fig. 6.4(a) the BC positions are normalized to the end of the curve ("common end" mode), whereas in Fig. 6.4(b) the BCs were inverted and positions were normalized to the curves beginning ("common start" mode).

The charge identification of the nuclei stopped inside the BCD volume is possible by careful inspection of various relationships between the BC parameters. This is presented in the following section.

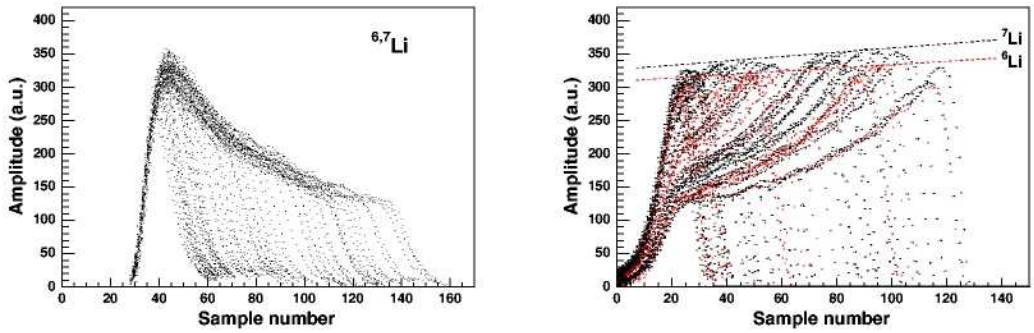

(a) The BCs in "common end" mode

(b) The inverted BCs in "common start" mode

Figure 6.4. Example of BCs in "common end" and "common start" modes (for explanation see text). The presented BCs describe the energy loss of Li particles inside BCD volume at 15°. In figure (b) the effect of increasing of the BC amplitude with particle's range is visible (for explanation see section 6.2.6 on page 39). The straight dashed-lines are drawn to guide the eye. The figures (a) and (b) depict the same curves.

6.2.2 Bragg curve smoothing methods

The anode signal of the BCD was fed to the specially designed amplifier [115,116]. During the amplification process the signal is also smoothed. The integral constant of the amplifier was fitted in order to keep balance between correct reconstruction of the signal and the noise suppression. The decreasing of the integral constant value allows for more precise signal reconstruction, but unfortunately increases the noise [115]. The relations between curve's parameters are retained. The BCs after this raw smoothing operation are still considerably disturbed by noise. In order to suppress noise two methods in the off-line analysis were tested: the running (moving) average method (RAM) [139,140], and approximated harmonic analysis (AHA) [141–150]. It was found that both smoothing methods give similar results and only slightly improve particles identification. Nevertheless even small improvement was welcomed and desired. Since the RAM method is much faster then AHA it has been chosen for the shape analysis of the BC. Details of the mathematical backgrounds of RAM and AHA methods can be found in Ref. [139–150].

6.2.3 Offset value determination

Due to an unavoidable low frequency oscillation of the signal, caused by the electronics, the baseline offset of the signal slightly changes its position, and influences the determination of the BC amplitude. In order to minimize this effect the offset's baseline subtraction was performed by applying the following procedure. The offset value was found separately for each BC as an average value from the first 25 samples of the signal (see Fig. 6.3 on the preceding page). The choice of the first 25 samples was determined by almost constant value of the offset in that region in contrary to the behavior of the offset for sample number greater than 160.

The offset values was different for a given isotope, and were stable during the whole data taking period. The overall offset value can be well approximated by the Gaussian distributions. The results for BCD mounted at 15° are presented in Fig. 6.5. The efficiency of the MCPDs were not taken into account.

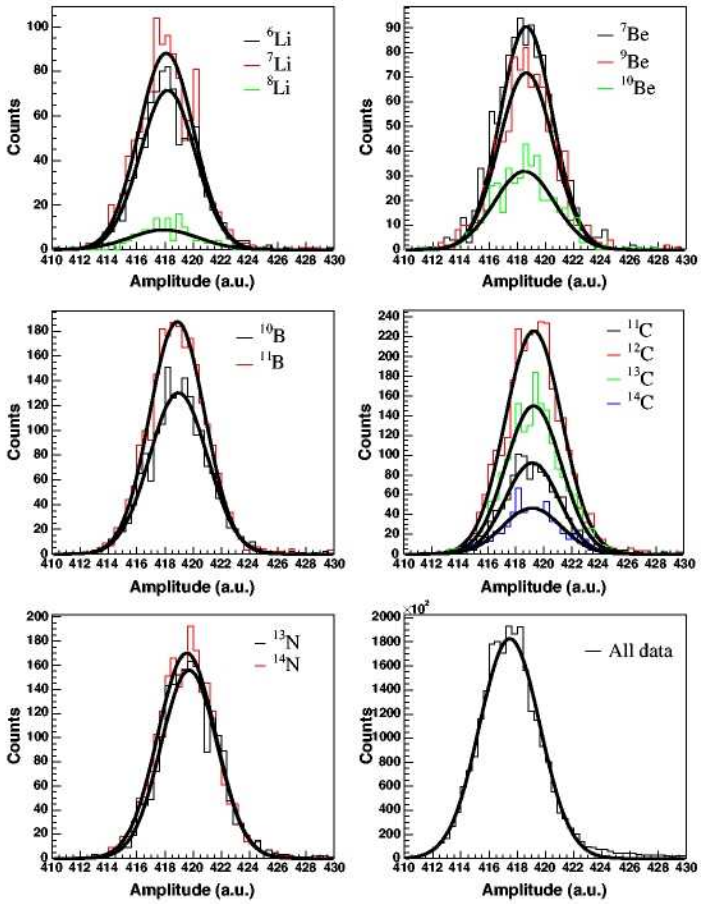

Figure 6.5. The distribution of the offset values for BCs (BCD mounted at 15°).

6.2.4 Particle's energy determination

The correct determination of the energy deposited by the particles inside the BCD volume is crucial for the particle's identification and the determination of the production cross section.

Several methods for particle's energy evaluation were tested. In the simplest approach particle's energy was obtained from the BC integration over all 200 samples. However, the discrepancy between simulated and measured value of the energy deposition was significant. Therefore more sophisticated method has been used. It is based on the BC derivatives. The maximum and minimum values of the derivative of each BC were found. The maximum of the derivative in the "common end" mode (see Fig. 6.4(a) on the facing page) corresponds to the place where particle was stopped in the BCD (MAXD), whereas minimum correspond to the beginning of the BC (MAXC). Difference between the MAXD and MAXC gives the range of a particle in the BCD (see Fig. 6.3 on page 35). The energy deposited by a particle in the BCD volume was obtained from the BC integration between MAXD and MAXC. Although obtained results were much better then previously, nevertheless were still not satisfactory (if one compares experimental values of deposited energy to the simulation). The additional corrections were needed. It was done by adding contributions to the deposited energy from regions "A" and "B" shown in Fig. 6.3 on

page 35. It was particularly important for the region "B" due to its large contribution at small energies deposited inside BCD volume. After adding contributions from regions "A" and "B" results from the simulation and measurement become consistent.

6.2.5 Detector calibration

Depending on the detector used in the experiment, different calibration methods have been applied. They are presented in this section.

6.2.5.1 Time calibration of the MCPDs

Time-of-flight measurements were performed between two MCPD working as "start" and "stop" detectors. The "stop" MCPD was installed 515 mm away from the "start" MCPD. Signals from both detectors, after discrimination, were sent to the Time to Amplitude Converter (TAC). This module gives an output signal which is proportional to the time difference between input signals. The calibration was performed by use of the pulse generator and delay lines. Two signals from pulse generator, one delayed with respect to the second one by known value (these signals simulate the signals from MCPDs) were fed to the TAC module. The calibration points were obtained by sequential delaying one of them by a known time value. This method allows to find the relation (calibration function) between the amplitude of the output signal from TAC module and the time difference.

6.2.5.2 Energy calibration of the BCDs

The energy calibration of the BCDs was based on the knowledge of the so called "punch through points" (PTPs). The PTPs define the maximal value of the total energy deposited by a given element or isotope in the BCD volume. The PTPs were found for both experimental and simulated data from two relations: (i) maximum of the amplitude of the BCD (so called Bragg Peak) versus energy deposited by a particle inside the BCD volume (one point for each element), and (ii) deposited energy versus time-of-flight (one point for each distinguishable isotope of a given element). The time-of-flight was measured between two microchannelplate detectors situated in the front of the BCD.

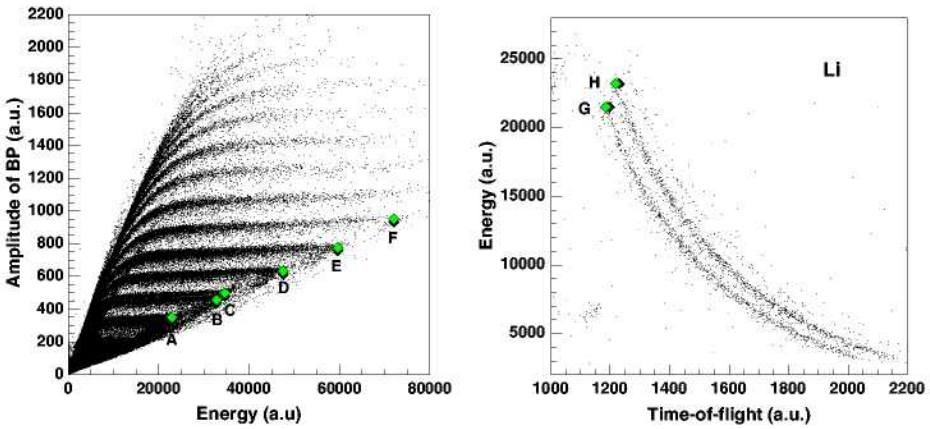

(a) amplitude vs deposited energy (b) deposited energy vs time-of-flight

Figure 6.6. The positions of the "punch through points" (PTPs). The PTPs are marked by diamonds. The capital letters correspond to: **A**: (^{6,7}Li), **B**: (^{7}Be), **C**: (^{9,10}Be), **D**: (^{10,11}B), **E**: (^{11,12,13,14}C), **F**: (^{13,14}N), **G**: (^{6}Li) and **H**: (^{7}Li)). The data are from BCD and MCPDs at 15° from p(1.9 GeV) + ^{nat}Ni reaction. In figure (b) only data for lithium are shown.

4.2 PISA software package

Among the programs used in the PISA data acquisition system (PDAQ) the following three are the most important: decoder, HistFiller and HistPresenter. They make a framework for other components of the PDAQ. Their short description, together with their abilities, methods of application and interdependencies (see Fig. 4.4 on page 28) is presented in chapters 4.2.1 to 4.2.3 on pages 25–28. The programs have been written in the object oriented C++ programming language [126], Tcl/Tk open source scripting language [127] and Bash script language [128]. The program package of the PISA software has been written from scratch and was continously developed in the framework of the presented PhD thesis.

The scheme of the data stream flow between the programs is presented in Fig. 4.2.

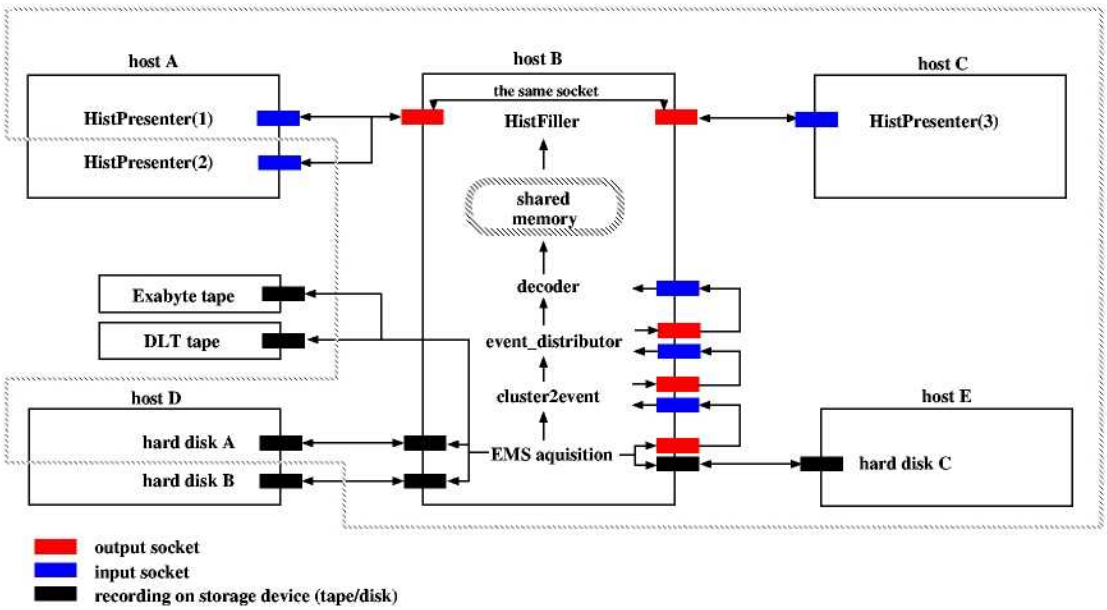

Figure 4.2. The scheme of the possible data stream flow between the PDAQ programs. The configuration used during the October 2002 data taking is indicated by dashed line.

4.2.1 Decoder program

The main goal of the decoder program is the data transformation from one coding system to another one. It also allows simultaneous access to encoded data by other programs using the shared memory[8] method. The decoder program can operate in two modes: on- or off-line. The scheme of the input-output stream flow in the decoder is shown in Fig. 4.3 on page 27.

As mentioned in chapter 4.1 on page 23, raw data can be simultaneously send by the EMS data acquisition system to various places. One of them can be a virtual socket on the host or remote computer (connected via network). The sockets may be viewed for network connections as attachment points in computer. In the on-line mode, the decoder attaches itself to a socket and

[8] "In computer programming, shared memory is a method by which program processes can exchange data more quickly than by reading and writing using the regular operating system services. For example, a client process may have data to pass to a server process that the server process is to modify and return to the client. Ordinarily, this would require the client writing to an output file (using the buffers of the operating system) and the server then reading that file as input from the buffer to its own work space. Using a designated area of shared memory, the data can be made directly accessible to both processes without having to use the system services. To put the data in shared memory, the client gets access to shared memory after checking a semaphore value, writes the data, and then resets the semaphore to signal to the server (which periodically checks shared memory for possible input) that data is waiting. In turn, the server process writes data back to the shared memory area, using the semaphore to indicate that data is ready to be read." [129]

waits for the data from the EMS data acquisition program. This is also called listening on the port [130]. If data appear on a listened socket, the decoder will start to process it and place data in required form, in required destination. There are two possible data forms: the "tree" structure derived from the ROOT software [131], and the raw ASCII[9] format. The possible destinations are: the shared memory or the hard disc. In the latter case, the data before writing on the disc are encapsulated in a wider structure, the so called "root file" [131]. The first destination (shared memory) is used mainly during the on-line mode, because the shared memory allows for easy exchange of the data between the decoder and external programs.

There is a fundamental difference between on- and off-line operating modes. During the on-line mode, the tree structure consists of only one entry (the event, see: Tab. 4.1 on page 24 and Fig. 4.1 on page 24) in a given time. The next event replaces the previous one. The reason of using such solution was to decrease the occupation of memory by unneeded events. In the off-line mode the events are appended to the existing tree. Also, in off-line mode apart from the creation of the "root file" (with the tree), the decoder can update the existing "root file" (update the existing tree).

In the on-line mode, the raw data (in the cluster format) can be fed to the decoder only via a socket, whereas in the off-line, mode the program is able to read the raw data either from disc file or from pipe[10].

The decoder program has a modular structure based on the object oriented C++ programming language [126]. In the frame of the decoder, a few specialized classes were designed. Some of them are connected with hardware modules: QDC (Charge Digital Converter), TDC (Time Digital Converter), ADC (Amplitude Digital Converter), FlashADC, Scaler and Pattern Unit. All these classes are derived from the global class Code. The short description of classes and their applications is given below:

1. **FlashADC** class
   This class is used for decoding of the data from the C.A.E.N.[11] Model V729A module. This module is a 4 channel 40 MHz ADC. "Its function is to convert and store in a buffer the input analog signals which belong to a programmable temporal window placed before or around a STOP signal." [117]. The signals from BCDs have been read by this module. It provides the information about the shape of the Bragg's signal.
2. **AQTDC** class (Amplitude, Charge and Time Digital Converter class)
   To this class belong 3 different modules with very similar type of decoding.
   - The C.A.E.N. Model V785, 32 channel peak sensing ADC module.
     "The model V785 is a 1-unit wide VME module housing 32 Peak Sensing Analog-to-Digital Conversion channel" [132]. Analog signals from all silicon detectors (including the monitor detectors), from "charge" output of the BCD's preamplifier [116], and also signals from the TAC (Time Amplitude Converter) module were fed to this module.
   - The C.A.E.N. Model V792, 32 channel QDC module [133].
     Signals from all 8 phoswich detectors were fed to it.
   - The C.A.E.N. Model V775, 32 channel TDC module.
     Signals from 4 MCPD belonging to the arms installed at 15° and 120°, with respect to the beam direction, were fed to it.
3. **ScalerV560E** class
   The class for decoding the data from the C.A.E.N. V560E module. "This is a 1-unit wide VME module provided with 16 independent 32-bit counting channels" [134].

[9] American Standard Code for Information Interchange

[10] A method for passing information from one computer process to another one. A named pipe is sometimes called a "FIFO" (first in, first out), because the first data written to the pipe is the first data that is read from it.

[11] Costruzioni Apparecchiature Elettroniche Nucleari S.p.A.

Chapter 5

Electronic setup

In the PISA experiment, standard NIM and VME electronics were used. The layout of the electronics circuit and the logic of connections are shown in Fig. 5.1 on the next page. The types of used VME modules together with methods of application are shown as well.

Four triggers (conditions) for the readout of the digitalizing modules were constructed. The first trigger was formed in the following way: (i) either couple MCPDs (under 15° or 120°), working in the coincidence mode, gave a signal, or (ii) the couple of the silicon detectors follow directly each other, regardless of number of arm where are mounted, were fired, or (iii) one of the phoswich detectors gave a signal. Second trigger was based on the BCDs. Irrespective which BCD gave a correct signal the condition number 2 was met. Third trigger was related to the monitor detectors working in the anti-coincidence mode. And the last one it was periodical, artificial impulse of 1 Hz frequency. The trigger conditions used in the PISA experiment are shown in Tab. 5.1.

Trigger No.	Conditions
1	$(MCP1\_15 \wedge MCP2\_15) \vee (MCP1\_120 \wedge MCP2\_120) \vee (S1 \wedge S2) \vee (S2 \wedge S3) \vee (S3 \wedge S4) \vee PH$
2	$BCD\_15 \vee BCD\_120$
3	$(ML1 \wedge \overline{ML2}) \vee (MR1 \wedge \overline{MR2})$
4	1 Hz - periodical artificial impulse

Table 5.1. The trigger conditions. MCP1_15 and MCP2_15 – microchannelplate start and stop at 15°, MCP1_120 and MCP2_120 – microchannelplate start and stop at 120°, S1, S2, S3, S4 – first, second, third and fourth silicon in telescopes independent from arm in which they are placed, ML1 and ML2 – monitor detectors (left side), MR1 and MR2 – monitor detectors (right side).

Various combinations of triggers were used for forming of the so called gates (signals) which were fed to the individual digitalizing modules. Start of the readout procedure was only permitted in the presence of a given gate. The gates has been constructed in the following way:

- In the presence of the signal gate formed from the trigger number 3, the amplitude digital converter module (Peak Sensing ADC - Model V785 [132]), which was used for monitor detectors, was read out.
- The readout of the signals from the amplitude digital converter module (ADC Model V795A [117]), used for both BCDs, was possible in the presence of the trigger number 1 or 2.
- Trigger number 1 allowed for the read out of the following modules:
  - two charge digital converter modules (QDC Model V793 [133]), serving all phoswich detectors,

- two amplitude digital converter modules, serving all silicon detectors and MCPDs (amplitude signal formed by time-to-amplitude converter (TAC)),
- time digital converter module (TDC Model V775 [137]), serving MCPDs.

• The 1 Hz artifical impulse was fed to the input gates of the scaler modules (Models V560 [134] and V830 [135]).

All digitalizing modules were produced by the C.A.E.N. Corporation.

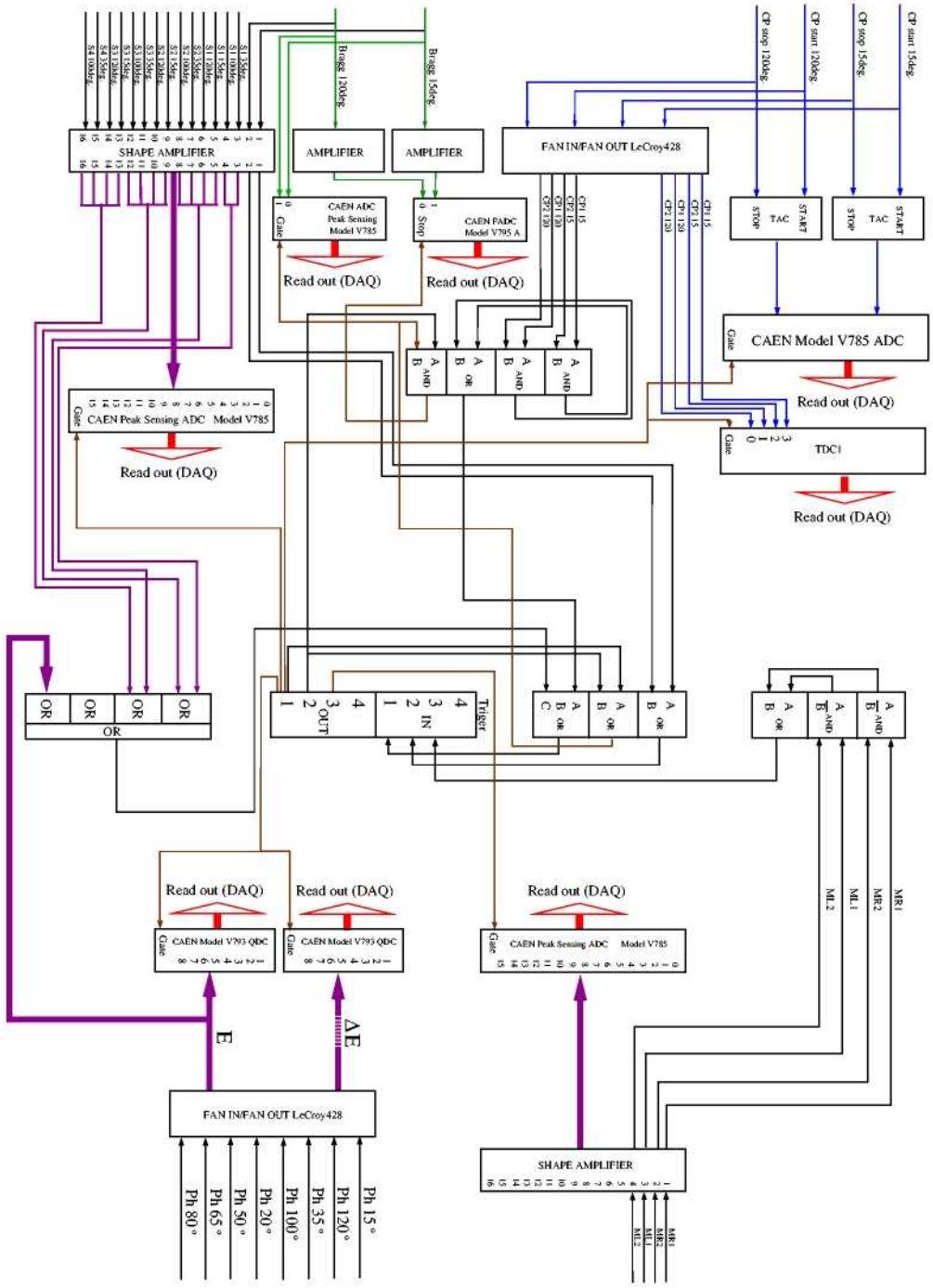

Figure 5.1. The simplified chart of the PISA electronics. Notation: S1–S4 – silicon detectors; CP – microchannelplates; Ph – phoswiches; MR – monitor right, ML – monitor left.

Chapter 6

Experimental procedures and data analysis

The identification of the intermediate mass fragments (IMFs; $3 \leqslant Z \leqslant 14$) produced in the interaction of 1.9 GeV protons with nickel (^{nat}Ni) has been a subject of interest. Energy spectra and angular distributions have been measured for isotopically separated elements. The identification of the emitted IMFs at 15° and 120° has been performed using BCDs and time-of-flight (TOF) technique. The BCDs were used for the charge identification, whereas the MCPDs together with BCDs for the mass identification. The details of the elements and isotopes identification are presented in this section. Determination of the temperature of excited nuclei by various methods, the comparison between nuclear matter thermometers, and the presentation of the obtained results in the energy-temperature diagram, the so called caloric curve (CC), are shown as well.

The analyzed data were collected during the experiment performed by the PISA collaboration in October 2002 at the COSY facility in the Forschungszentrum Jülich, Germany.

6.1 MCP detectors efficiency

The efficiency of the MCP detectors (MCPD) as a function of the kinetic energy and mass of the detected particles has been investigated.

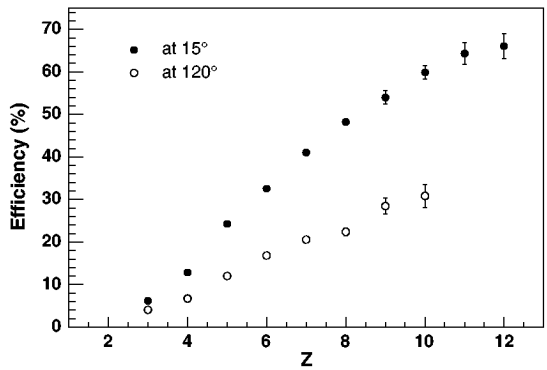

Figure 6.1. The efficiency of MCPs at 15° and 120° under assumption of 100% efficiency of the both BCDs.

The determination of the MCPD efficiency was performed assuming 100% efficiency of the BCD. It was defined as the number of particles detected by the BCD to the number of particles

detected by the MCPDs. The solid angles of both MCPD and the sticking of the particles in the foils between MCPD and BCD were taken into account. The solid angle is determined by the second MCPD (placed further away from the target; cf. Figs. 3.2 to 3.3 on pages 15–16). The second MCPD to BCD Frish grid solid angle ratio is equal to 0.34 ± 0.02. However the solid angle of the MCPD's housing is bigger than BCD one. Therefore particles observed inside the BCD should cross the MCPDs ("start" and "stop"). The efficiency of the MCPDs at 15° and 120° assuming 100% efficiency of the BCD is shown in Fig. 6.1 on the page before.

The efficiency of the MCPD varies from 6.65 ± 0.02 % to 59.87 ± 1.56 %, and from 4.32 ± 0.02 % to 30.80 ± 2.63 for $3 \leqslant Z \leqslant 10$, for 15° and 120°, respectively. The efficiency of the MCPD is a function of the charge of the detected particle and increases with increasing Z.

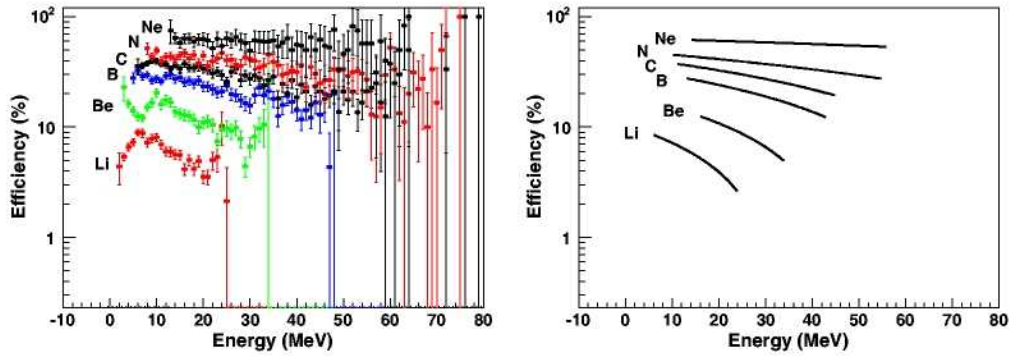

(a) MCPD at 15°

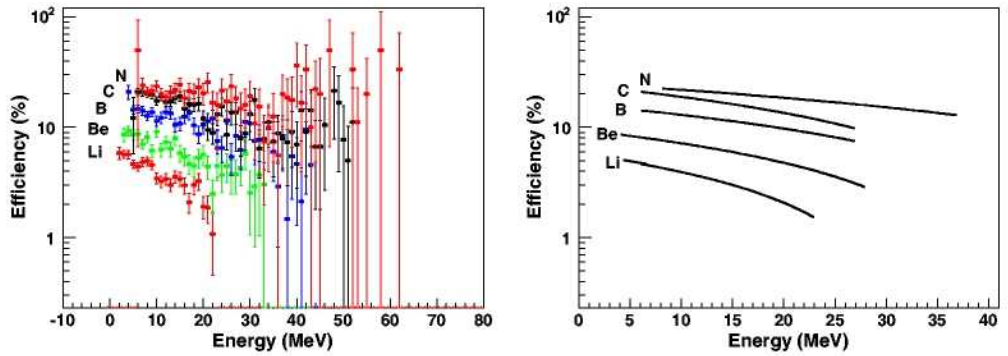

(b) MCPD at 120°

Figure 6.2. The efficiency of MCPDs as a function of the kinetic energy deposited inside the BCD volume assuming 100% efficiency of the BCD. The lines represent fit curves to the experimental data points.

The MCPD efficiency as a function of the energy deposited inside the BCD volume at 15° and 120° assuming 100% efficiency of the BCD is shown in Fig. 6.2. The lines in Figs. 6.2(a) and 6.2(b) are drawn only to guide the eyes, and represent fit curves to the experimental data points. The determination of the efficiency was performed for particles stopped inside the BCD volume. The efficiency of the MCPD for all particles decreases with increasing energy deposited inside the BCD or in general, with incident particle energy. The relationship between particles incident energy and energy deposited inside the BCD volume, obtained from the Geant4 [63] simulations, are shown in appendix B on page 73. The observed decreasing MCPD efficiency with energy and various slopes of the efficiency curves are effect of the three following facts: (i)

the energy loss dE/dx strongly decreases with increasing incident particle energy [138], (ii) the energy loss increases with increasing atomic and mass number of the incident particle [138], and (iii) the δ-electron production increases with increasing energy loss.

6.2 Bragg curve and microchannelplate detectors analysis

There is no excellent beauty that has not some strangeness in the proportion

Francis Bacon 1561–1626

6.2.1 Shape of the Bragg curve

A particle which crosses the BCD creates the ionization along its track. Electrons produced along the track drift through the Frish grid to the anode, where they are collected and observed as an anode current. The anode signal is amplified by specially designed preamplifier (PA) [115, 116] with two different outputs. The output signal from the PA, which reflects the anode current, is sampled by the Flash ADC (C.E.A.N. Model V729A module [117]). Sampling is made at the rate of 10 MHz and consists of 200 samples. As result one obtains the shape of the Bragg curve (BC). The shape of the BC can be characterized by the following parameters: the range of the particle (RG), the amplitude of the Bragg peak (BP), and the energy of the particle (E). The RG is associated to the depth of the particle's penetration inside the BCD volume. The BP corresponds to the maximum of the energy loss (maximal value of dE/dx) at the end of the particle's path, and is a direct measurement of the particle charge. The E is a kinetic energy deposited by the particle in the BCD volume and can be obtained from the area under the BC.

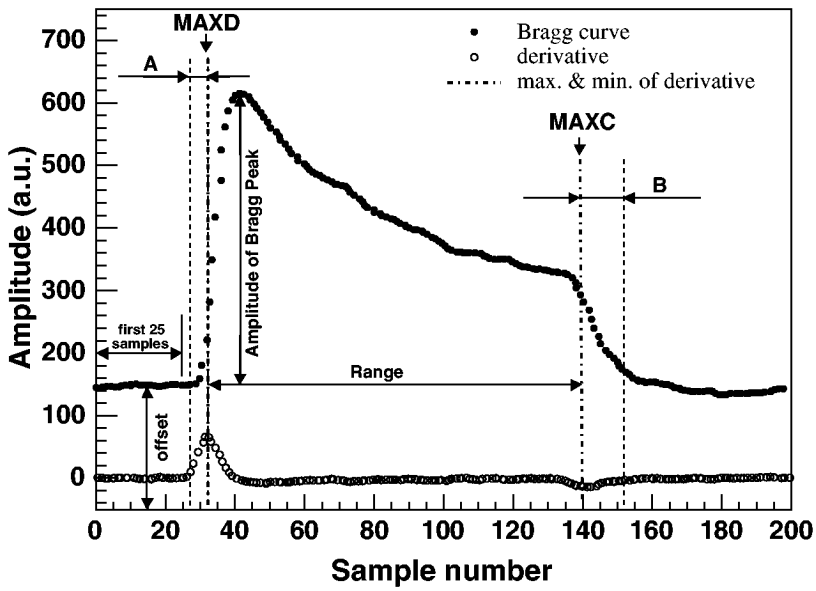

Figure 6.3. Example of the BC with marked parameters: range (RG) and amplitude of Bragg Peak (BP). The presented curve is a mirror image of the real curve (for explanation see section 3.2.3 on page 18). The derivatives of the BC are also presented. The areas "A", "B", positions of maximum (MAXD) and minimum (MAXC) values of the derivative are indicated – for details see text. The amplitude axis is chosen for the best presentation of the BC and its derivative.

A typical shape of the BC is presented in Fig. 6.3 on the preceding page. More examples are presented in Fig. 6.4, where BCs are created by lithium isotopes which sticked inside the BCD volume mounted at 15°. In Fig. 6.4(a) the BC positions are normalized to the end of the curve ("common end" mode), whereas in Fig. 6.4(b) the BCs were inverted and positions were normalized to the curves beginning ("common start" mode).

The charge identification of the nuclei stopped inside the BCD volume is possible by careful inspection of various relationships between the BC parameters. This is presented in the following section.

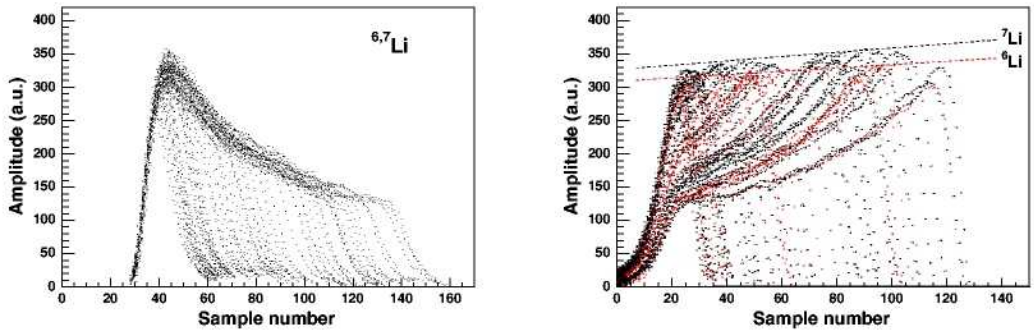

(a) The BCs in "common end" mode

(b) The inverted BCs in "common start" mode

Figure 6.4. Example of BCs in "common end" and "common start" modes (for explanation see text). The presented BCs describe the energy loss of Li particles inside BCD volume at 15°. In figure (b) the effect of increasing of the BC amplitude with particle's range is visible (for explanation see section 6.2.6 on page 39). The straight dashed-lines are drawn to guide the eye. The figures (a) and (b) depict the same curves.

6.2.2 Bragg curve smoothing methods

The anode signal of the BCD was fed to the specially designed amplifier [115,116]. During the amplification process the signal is also smoothed. The integral constant of the amplifier was fitted in order to keep balance between correct reconstruction of the signal and the noise suppression. The decreasing of the integral constant value allows for more precise signal reconstruction, but unfortunately increases the noise [115]. The relations between curve's parameters are retained. The BCs after this raw smoothing operation are still considerably disturbed by noise. In order to suppress noise two methods in the off-line analysis were tested: the running (moving) average method (RAM) [139,140], and approximated harmonic analysis (AHA) [141–150]. It was found that both smoothing methods give similar results and only slightly improve particles identification. Nevertheless even small improvement was welcomed and desired. Since the RAM method is much faster then AHA it has been chosen for the shape analysis of the BC. Details of the mathematical backgrounds of RAM and AHA methods can be found in Ref. [139–150].

6.2.3 Offset value determination

Due to an unavoidable low frequency oscillation of the signal, caused by the electronics, the baseline offset of the signal slightly changes its position, and influences the determination of the BC amplitude. In order to minimize this effect the offset's baseline subtraction was performed by applying the following procedure. The offset value was found separately for each BC as an average value from the first 25 samples of the signal (see Fig. 6.3 on the preceding page). The choice of the first 25 samples was determined by almost constant value of the offset in that region in contrary to the behavior of the offset for sample number greater than 160.

The offset values was different for a given isotope, and were stable during the whole data taking period. The overall offset value can be well approximated by the Gaussian distributions. The results for BCD mounted at 15° are presented in Fig. 6.5. The efficiency of the MCPDs were not taken into account.

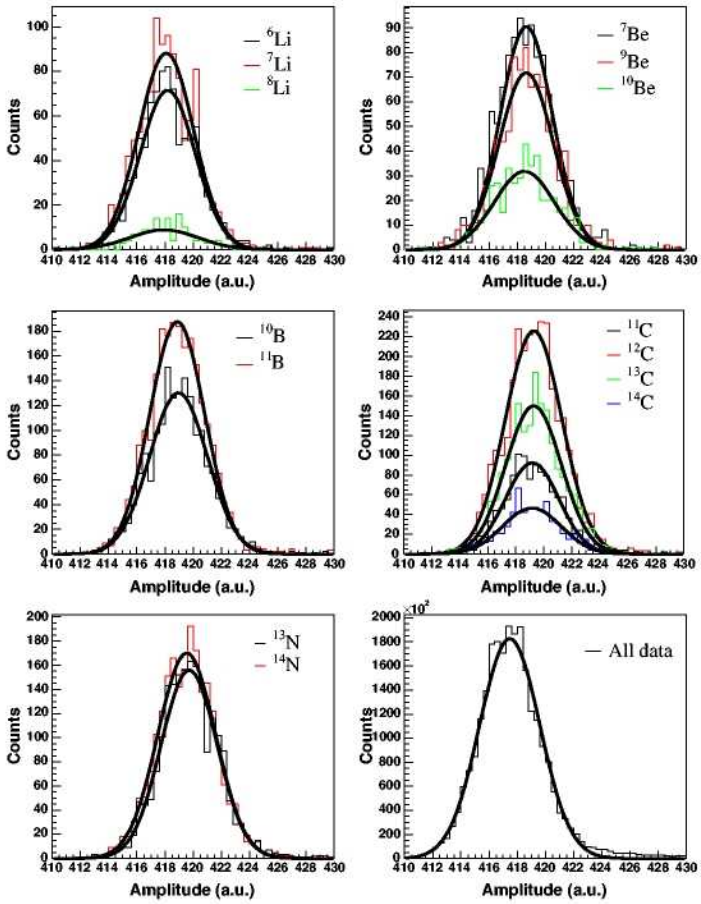

Figure 6.5. The distribution of the offset values for BCs (BCD mounted at 15°).

6.2.4 Particle's energy determination

The correct determination of the energy deposited by the particles inside the BCD volume is crucial for the particle's identification and the determination of the production cross section.

Several methods for particle's energy evaluation were tested. In the simplest approach particle's energy was obtained from the BC integration over all 200 samples. However, the discrepancy between simulated and measured value of the energy deposition was significant. Therefore more sophisticated method has been used. It is based on the BC derivatives. The maximum and minimum values of the derivative of each BC were found. The maximum of the derivative in the "common end" mode (see Fig. 6.4(a) on the facing page) corresponds to the place where particle was stopped in the BCD (MAXD), whereas minimum correspond to the beginning of the BC (MAXC). Difference between the MAXD and MAXC gives the range of a particle in the BCD (see Fig. 6.3 on page 35). The energy deposited by a particle in the BCD volume was obtained from the BC integration between MAXD and MAXC. Although obtained results were much better then previously, nevertheless were still not satisfactory (if one compares experimental values of deposited energy to the simulation). The additional corrections were needed. It was done by adding contributions to the deposited energy from regions "A" and "B" shown in Fig. 6.3 on

page 35. It was particularly important for the region "B" due to its large contribution at small energies deposited inside BCD volume. After adding contributions from regions "A" and "B" results from the simulation and measurement become consistent.

6.2.5 Detector calibration

Depending on the detector used in the experiment, different calibration methods have been applied. They are presented in this section.

6.2.5.1 Time calibration of the MCPDs

Time-of-flight measurements were performed between two MCPD working as "start" and "stop" detectors. The "stop" MCPD was installed 515 mm away from the "start" MCPD. Signals from both detectors, after discrimination, were sent to the Time to Amplitude Converter (TAC). This module gives an output signal which is proportional to the time difference between input signals. The calibration was performed by use of the pulse generator and delay lines. Two signals from pulse generator, one delayed with respect to the second one by known value (these signals simulate the signals from MCPDs) were fed to the TAC module. The calibration points were obtained by sequential delaying one of them by a known time value. This method allows to find the relation (calibration function) between the amplitude of the output signal from TAC module and the time difference.

6.2.5.2 Energy calibration of the BCDs

The energy calibration of the BCDs was based on the knowledge of the so called "punch through points" (PTPs). The PTPs define the maximal value of the total energy deposited by a given element or isotope in the BCD volume. The PTPs were found for both experimental and simulated data from two relations: (i) maximum of the amplitude of the BCD (so called Bragg Peak) versus energy deposited by a particle inside the BCD volume (one point for each element), and (ii) deposited energy versus time-of-flight (one point for each distinguishable isotope of a given element). The time-of-flight was measured between two microchannelplate detectors situated in the front of the BCD.

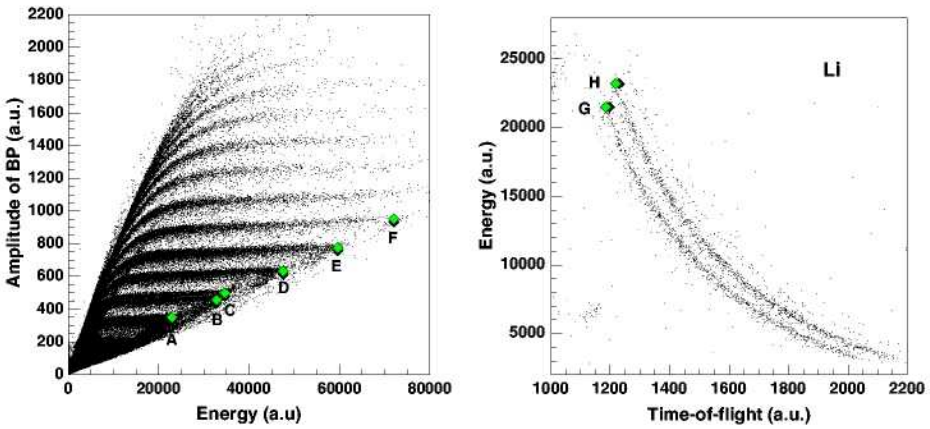

(a) amplitude vs deposited energy (b) deposited energy vs time-of-flight

Figure 6.6. The positions of the "punch through points" (PTPs). The PTPs are marked by diamonds. The capital letters correspond to: **A**: (^{6,7}Li), **B**: (^{7}Be), **C**: (^{9,10}Be), **D**: (^{10,11}B), **E**: (^{11,12,13,14}C), **F**: (^{13,14}N), **G**: (^{6}Li) and **H**: (^{7}Li)). The data are from BCD and MCPDs at 15° from p(1.9 GeV) + ^{nat}Ni reaction. In figure (b) only data for lithium are shown.

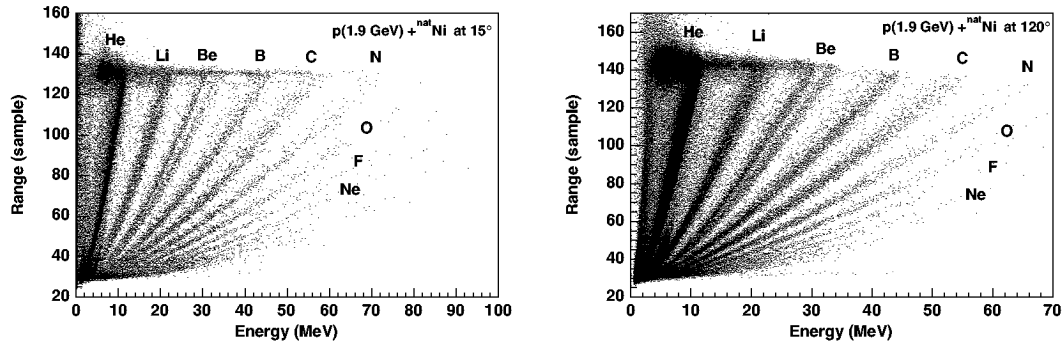

(a) The BCD at 15°

(b) The BCD at 120°

Figure 6.10. Scatter plot of the range versus deposited energy of the particles measured inside the BCD volume mounted at 15° and 120° (cf. Fig. B.3(c) on page 75). The identified reaction products are indicated.

The low energy cutoff in the identification of the particles arises from the detectors thresholds, and from particles energy losses in the foils placed in the front of the BCD. The detector energy threshold is about 0.5 MeV/A and is common for all detected Z (see Fig. 6.12(b) on the following page and Fig. 6.14 on page 43). The dependence of the energy deposited in the BCD volume on the particle incident energy is shown in section B.1 on page 73.

The charge resolution of the BCD at 15° for the fragments stopped inside BCD volume is presented in Fig. 6.11. Because the width of the distribution along the COGs is not constant (width increases with energy) the produced spectra have no Gaussian distribution. The width of the distribution is a function of energy. This effect is shown in Fig. 6.13 on page 43, where the spectra of C and N elements (BCD at 15°), divided into two energy regions, are presented. The energy division is made at 15 MeV for C and 18 MeV for N element. The broadening of the distributions with energy is also shown in Fig. 6.14 on page 43, where the standard deviation of the Gaussian distribution as a function of energy for Li, B, C and N nuclei are presented.

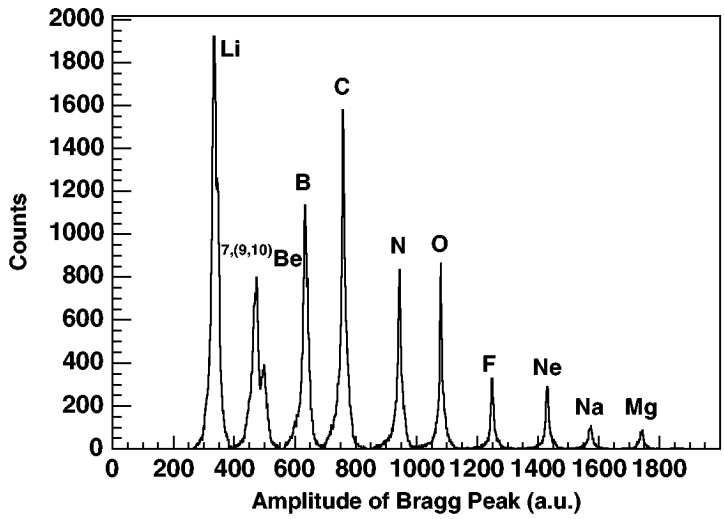

Figure 6.11. Charged products of the p(1.9 GeV) + ^{nat}Ni reaction measured at 15°. The projection of the Z distribution along the centers of gravities is presented (see also Fig. 6.12 on the next page). The beryllium isotopes ($^{7,(9,10)}$Be) are separated thanks to the absence of ^{8}Be.

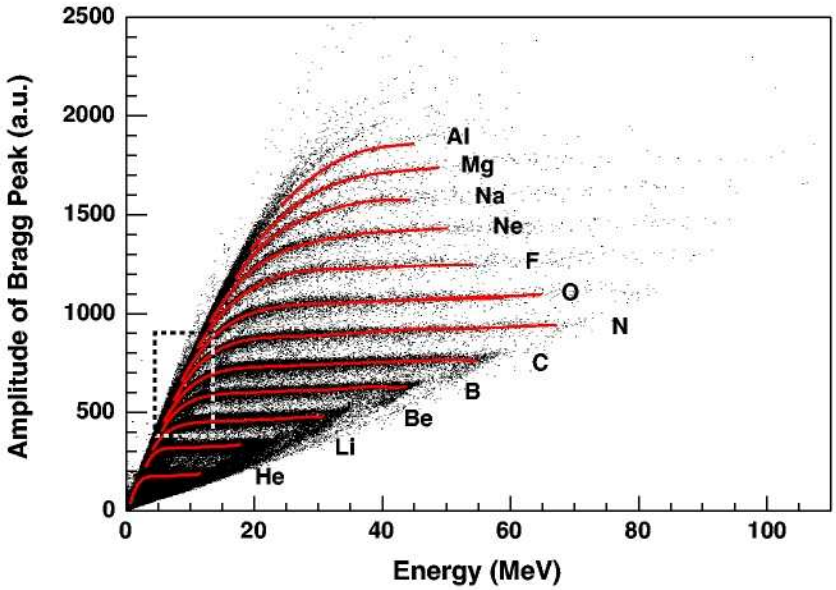

(a) The total area.

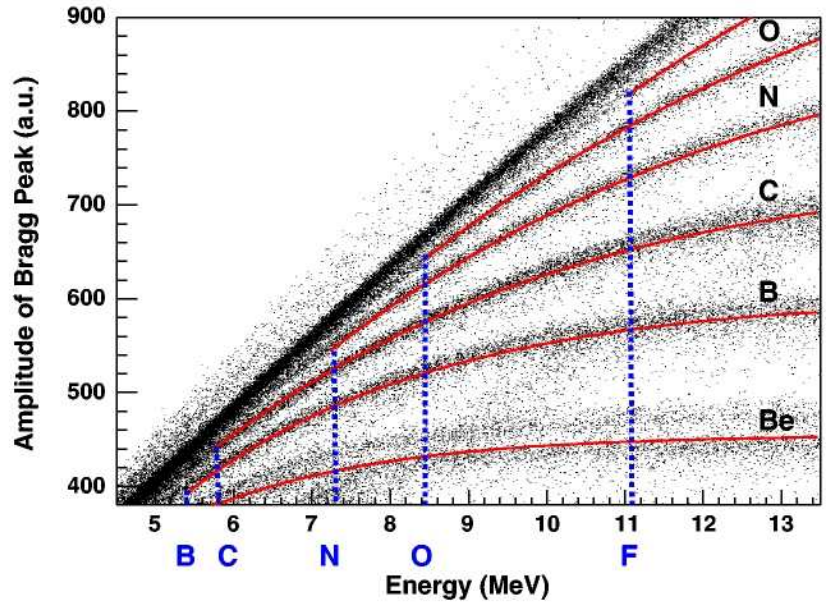

(b) Zoom: the area marked by black-white dashed line in Fig. 6.12(a).

Figure 6.12. (a) Scatter plot of the amplitude of the BP versus the kinetic energy of the registered particles. The p(1.9 GeV) + ^{nat}Ni reaction products were measured at 15°. The line fitted to the centers of gravity of the individual Z distribution are plotted (red continuous lines). For heavier elements, due to the poor statistics at higher energies, the fitted lines do not cover the full stopping energy range of the detector. Both the lower, as well as the upper energy limits used for histogramming (cf. Fig. 6.11 on the preceding page) correspond to the left and right ends of the fitted curve, respectively. (b) The zoom of the rectangular part stressed by dashed-line in figure (a). The lower energy limits, above which the individual elements can be resolved are shown as vertical dashed lines.

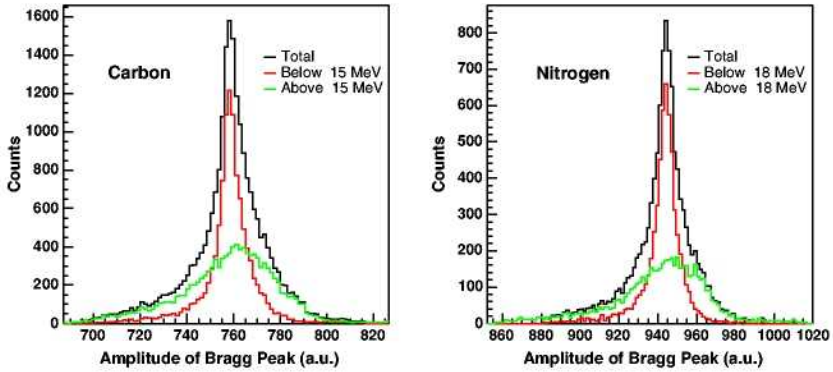

Figure 6.13. The total and partial charge identification spectra for C and N elements. The partial Z identification spectra present the data below and above certain energy (15 MeV for C and 18 MeV for N element). The data are from p(1.9 GeV) + ^{nat}Ni reaction products detected in the BCD at 15°.

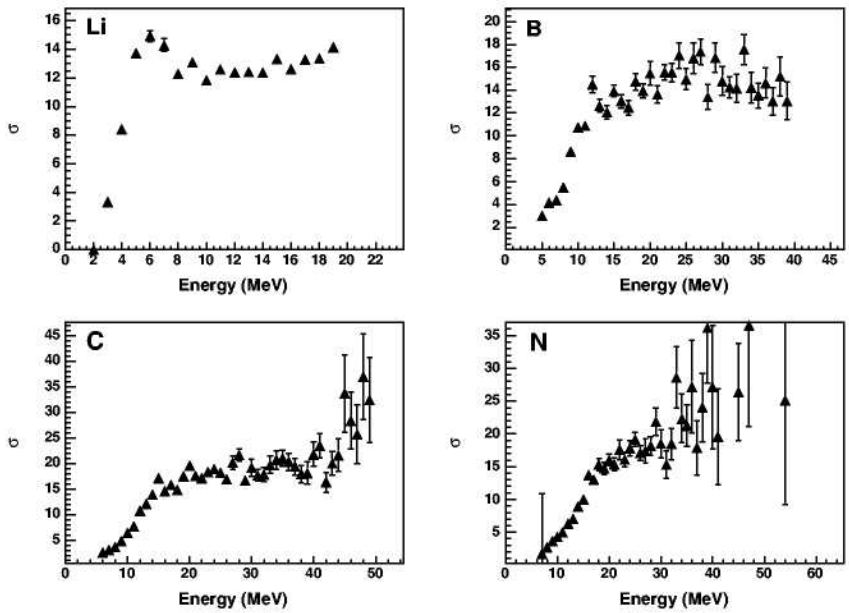

Figure 6.14. The standard deviation of the partial Gaussian charge identification spectrum as a function of energy for Li, B, C and N elements. The data are from p(1.9 GeV) + ^{nat}Ni reaction products detected in BCD at 15°.

6.2.6.2 Identification of the mass number with MCPDs and BCD

The mass separation was done by combining the informations from the MCPDs (time-of-flight) and the BCD (energy deposited inside the BCD volume). With the experimental set-up used and by applying methods described above, separation of following isotopes was possible: ^{6}Li, ^{7}Li, ^{8}Li; ^{7}Be, ^{9}Be, ^{10}Be; ^{10}B, ^{11}B; ^{11}C, ^{12}C, ^{13}C, ^{14}C and ^{13}N, ^{14}N. The energy deposited inside the BCD as a function of the time-of-flight is presented in Figs. 6.15 to 6.16 on the next page together with isotopes separation for 15° and 120°.

In order to obtain the isotope identification spectra, the projections along the line fitted to the COGs of each elements' distribution were performed. The example of lines fitted to the COGs

for Be isotopes, identified at 15° and produced in p(1.9 GeV) + ^{nat}Ni reaction, are shown in Fig. 6.17 on the facing page.

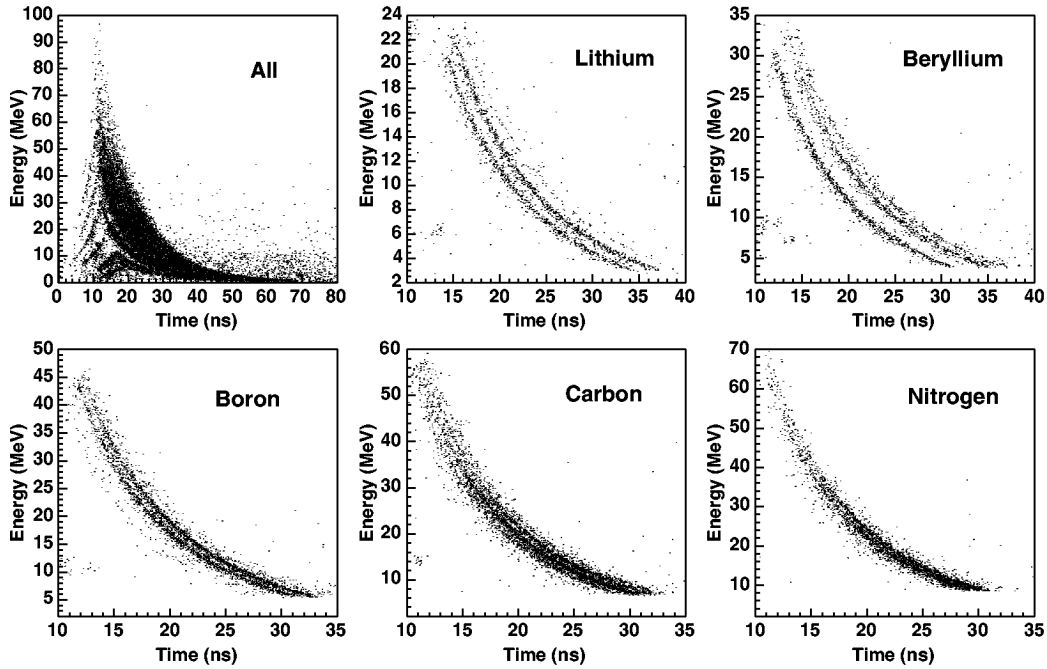

Figure 6.15. Energy deposited inside the BCD volume versus the time-of-flight measured at 15° in p(1.9 GeV) + ^{nat}Ni reaction. The isotope separation is shown.

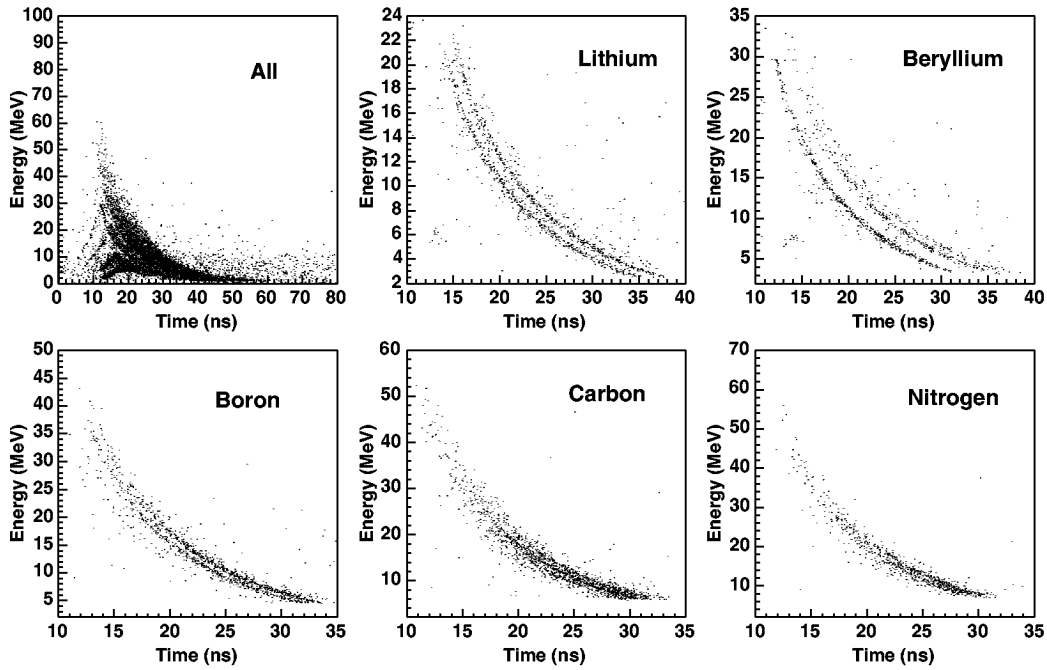

Figure 6.16. Energy deposited inside the BCD volume versus the time-of-flight measured at 120° in p(1.9 GeV) + ^{nat}Ni reaction. The isotope separation is shown.

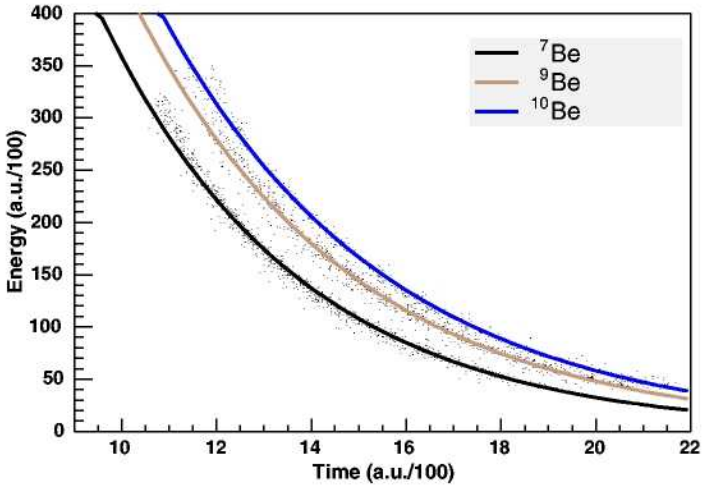

Figure 6.17. The separation of three beryllium isotopes detected at 15° and produced in the p(1.9 GeV) + ^{nat}Ni reaction. The fits to COGs are plotted.

Due to the fact that the lines fitted to the isotopes' COGs of a given element are not parallel (see Fig. 6.17), the projections along various centers of gravity are not the same. Therefore, in order to obtain identification spectra of different isotopes, the projections were performed along each COG of a given element separately. The final choice of the COG was done by the inspection of each projection. The best possible isotope separation was obtained when the projections along the COGs of ^{7}Li, ^{9}Be, ^{11}B, ^{12}C and ^{14}N were chosen. The results are shown in Fig. 6.18 and Fig. 6.19 on the next page.

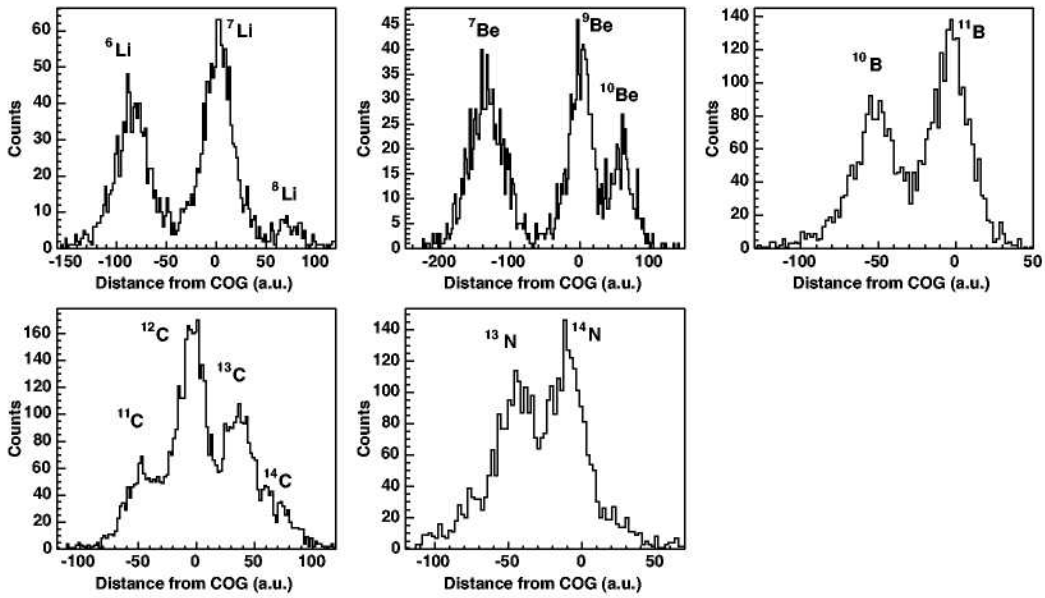

Figure 6.18. The mass identification spectra of the p(1.9 GeV) + ^{nat}Ni reaction products measured at 15° obtained by the projection of the mass distributions along the centers of gravities of ^{7}Li, ^{9}Be, ^{11}B, ^{12}C and ^{14}N.

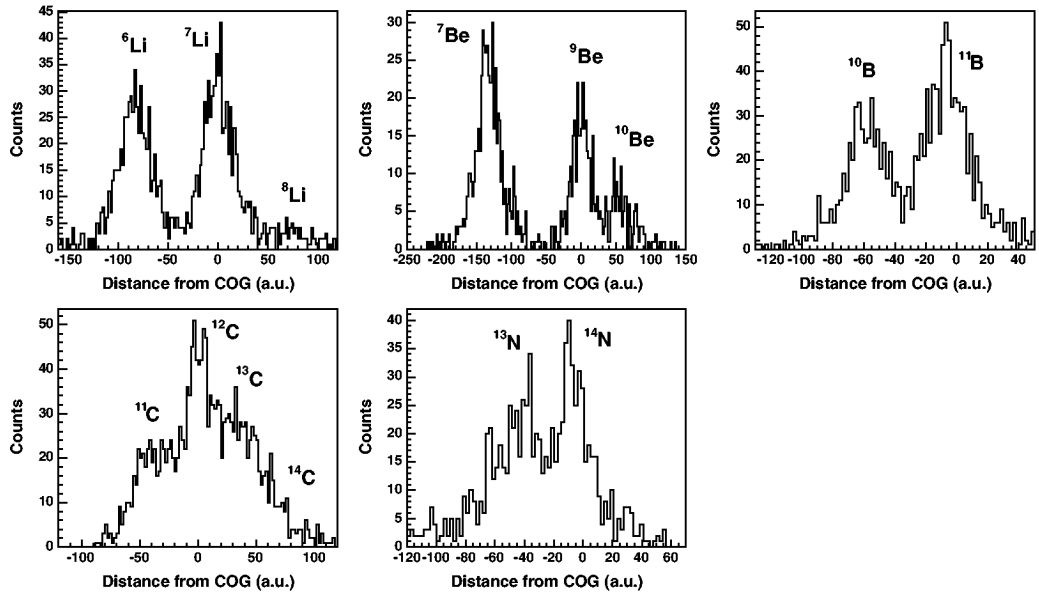

Figure 6.19. The mass identification spectra of the p(1.9 GeV) + ^{nat}Ni reaction products measured at 120° obtained by the projection of the mass distribution along the centers of gravities of ^{7}Li, ^{9}Be, ^{11}B, ^{12}C and ^{14}N.

6.2.6.3 Identification of the mass number with BCD

As it has been discussed in section 6.1 on page 33 the MCPDs efficiency in the charge range $2 \leqslant Z \leqslant 10$ varies from about 1.5% to 60% and 30% for 15° and 120°, respectively (assuming 100% efficiency of the BCD). Therefore it is extremely important to find a method which allows to distinguish particles' masses with the BCD only, even if there are no signals from MCPDs. The following methods have been tested: (i) the pulse shape discrimination method (PSD) was used for the data when only events from the BCD exist, and (ii) the reference shape method (RSM) for the data from both BCD and MCPD. Both methods are described below.

Pulse shape discrimination method

The pulse shape discrimination (PSD) technique, usual applied to scintillator detectors, can be also used in the BC analysis. Fig. 6.20 on the next page shows the relations between ΔE and E, where E is the total energy obtained by the integration of the whole area under the BC, whereas ΔE is the energy integrated over the restricted area of the BC. The resolving power of the PSD strongly depends on the area chosen for the ΔE integration. The best isotopes identification was obtained for $(\mathrm{MAXC} - 45) < \Delta E < (\mathrm{MAXC} - 10)$, where MAXC is sample's number for the minimum of the derivative (see Fig. 6.3 on page 35). This method allows for the separation of Li, Be and B isotopes within certain range of energy. Due to the lack of the mass identification, the elements heavier than $Z = 6$ are not shown in Fig. 6.20 on the next page.

Reference shape method

The reference shape method relies on looking for the average BC (reference BC (RBC), reference shape) for a given isotope. It was assumed that the RBCs are different for each isotope. In contrast to the PSD, this method can not be applied by using the BCD data only. For the determination of the reference curves the isotope distinction is required. Therefore signals registered by both MCPDs and BCD are needed.

In order to create the RBCs two different methods were tested:

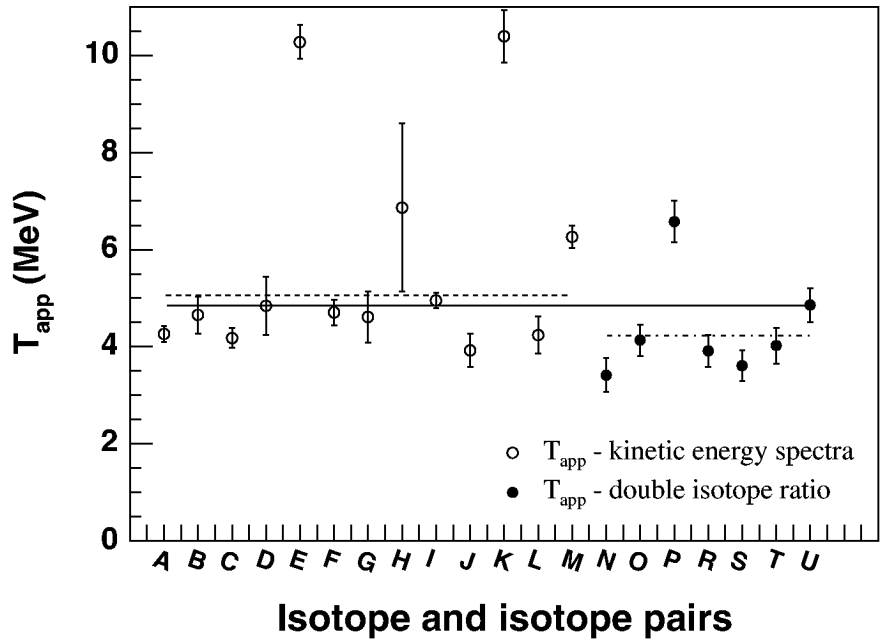

Figure 6.32. Comparison of apparent temperatures evaluated from two different methods. The open circles are T_{app} obtained from the slopes of the kinetic energy spectra, whereas full circles are from the double isotope ratio method. The straight lines are fits curves. The dashed line is the fit to the data extracted from the slope of the kinetic energy spectra, the dot-dashed line is the fit to the T_{app} values evaluated from the double isotope ratio and the solid line is the fit to temperatures from both methods. Letters on the x axis indicate the isotope or isotope ratio used **A**: (^{6}Li), **B**: (^{7}Li), **C**: (^{7}Be), **D**: (^{9}Be), **E**: (^{10}Be), **F**: (^{10}B), **G**: (^{11}B), **H**: (^{11}C), **I**: (^{12}C), **J**: (^{13}C), **K**: (^{14}C), **L**: (^{13}N), **M**: (^{14}N), **N**: (^{13}C/^{14}C)/(^{11}C/^{12}C), **O**: (^{6}Li/^{7}Li)/(^{11}C/^{12}C), **P**: (^{9}Be/^{10}Be)/(^{11}C/^{12}C), **R**: (^{12}C/^{13}C)/(^{11}C/^{12}C), **S**: (^{7}Li/^{8}Li)/(^{11}C/^{12}C), **T**: (^{7}Li/^{8}Li)/(^{13}C/^{14}C), **U**: (^{10}B/^{11}B)/(^{11}C/^{12}C).

6.5 Caloric curve

The caloric curve (CC) which relates the excitation energy of nucleus at thermodynamic equilibrium to its temperature is the simplest experimental tool to look for the existence of the phase transition. The CC shows the feature of the first order liquid-gas phase transition, with almost constant temperature of nuclear matter for excitation energies between 3 and 10 MeV/A. The CC presented in Fig. 6.33 on the next page was obtained from numerous data from Refs. [25, 27, 55, 56, 164, 169–177]. The data from the PISA measurement are included as well. Both values of apparent temperature which were used for the enrichment of the existing CC are average temperatures (T_{ave}) extracted from the slope of the kinetic energy spectra and the double yields ratio of emitted particles (cf. section 6.4.3 on the facing page). It has to be noticed, that we extracted the apparent temperature, which is not exactly the temperature of the nuclear matter, but it is only related to it.

The values of the excitation energy E^* of residues in the p(1.9 GeV) + ^{nat}Ni reaction was obtained by calculations performed with the theoretical Liège intranuclear cascade (INCL) model [46, 47], version 4.2 [178]. In this version of the code a new method of the determination of the time at which the intranuclear cascade stops (t_{stop}), and gives way to the evaporation, is proposed. At t_{stop} many physical quantities as E^*, average kinetic energy of ejectiles, or asymmetry of the participant momentum distribution are determined. This new method of the t_{stop} determination gives approximately two times larger value of the t_{stop} than obtained in the previous code version. Moreover, some physical observables as neutron or proton multiplicity, or E^* seems to be not correctly determined at this new value of t_{stop} [179]. Therefore in our

calculations the excitation energy was determined after $t_{stop}/2$, which is according to the author of the INCL code more realistic.

The yield distributions of the excitation energy per nucleon E^*/A are presented in Fig. 6.34. The average value of $E^*/A = 3.8 \pm 0.1$, indicated in Fig. 6.34 by dashed line was used for the construction of the caloric curve.

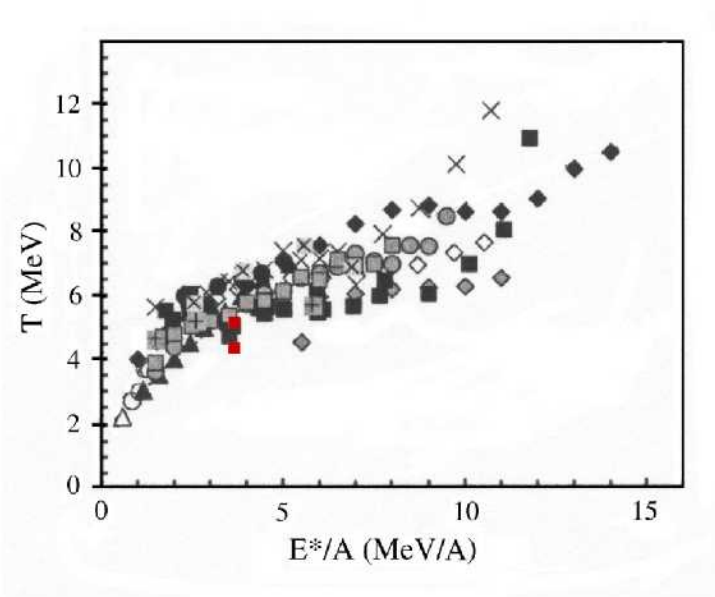

Figure 6.33. Caloric curve: temperature of the nucleus versus excitation energy per nucleon. The symbols correspond as follow: open circles - Ref. [55]; solid black circles - Ref. [164]; solid black diamonds - Ref. [56]; open square - Ref. [169]; solid black squares - Ref. [170]; solid black diamonds (^{84}Kr), open diamonds (^{134}La) and shaded diamonds (^{197}Au) - Ref. [171]; shaded triangles - Ref. [27]; cross in shaded squares - Ref. [25] and references therein; shaded circles (Ag) and shaded squares (^{197}Au) - Refs. [172–174]; $\times$ in shaded squares - Refs. [175, 176]; $\times$s - Ref. [177]. The results of the PISA measurement are presented by the solid red squares.

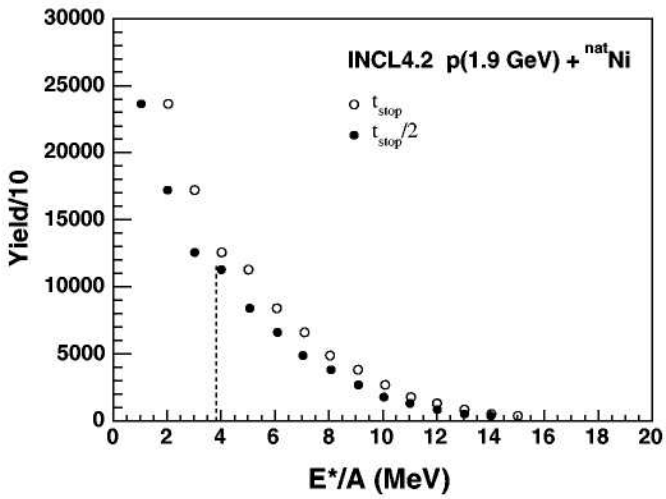

Figure 6.34. Population of the excitation energy per nucleon (E^*/A) calculated within the Liège intranuclear cascade model (INCL). Calculations from the INCL4.2 (t_{stop}) and INCL4.2-modified ($t_{stop}/2$) are shown.

Appendix A

Screenshots from the HistPresenter and the decoder programs.

In the present section a few screenshots from the decoder and HistPresenter program are shown. The screenshots from decoder program are shown in Fig. A.1, whereas in Figs. A.2 to A.11 on pages 68–72 the screenshots from HistPresenter program are presented. Both programs belong to the PISA software package. More details about applicability and functionality of the programs can be found in section 4.2.1 on page 25 and 4.2.3 on page 28.

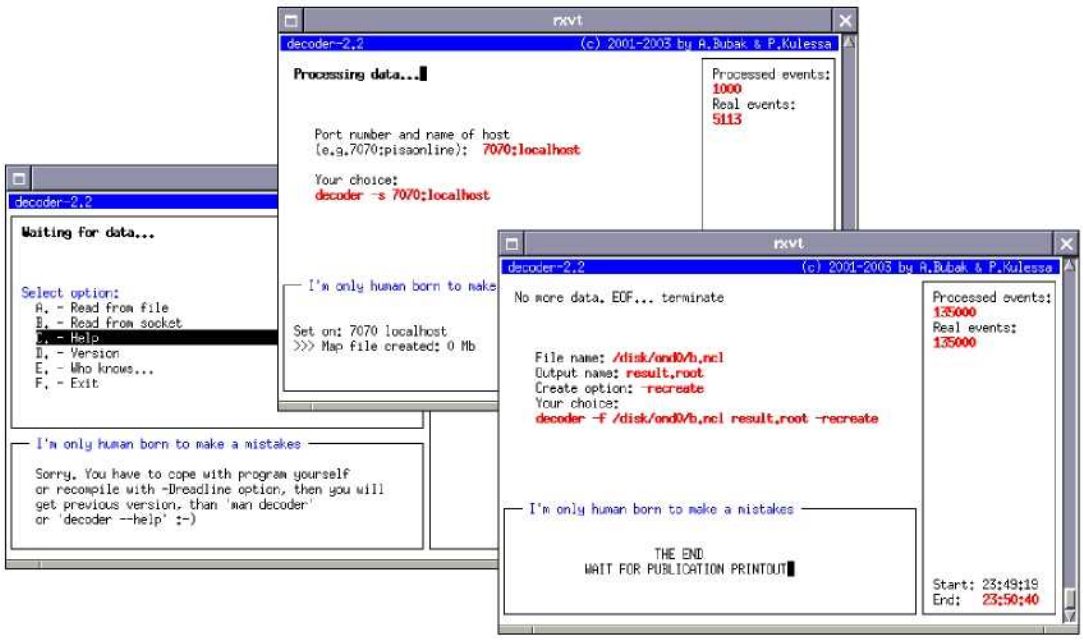

Figure A.1. The screenshots of frontend to the decoder program. Three panels from left-bottom to right-top: the start panel; panel associated with the on-line mode; panel associated with the off-line mode. The frontend is written with ncurses library routines.

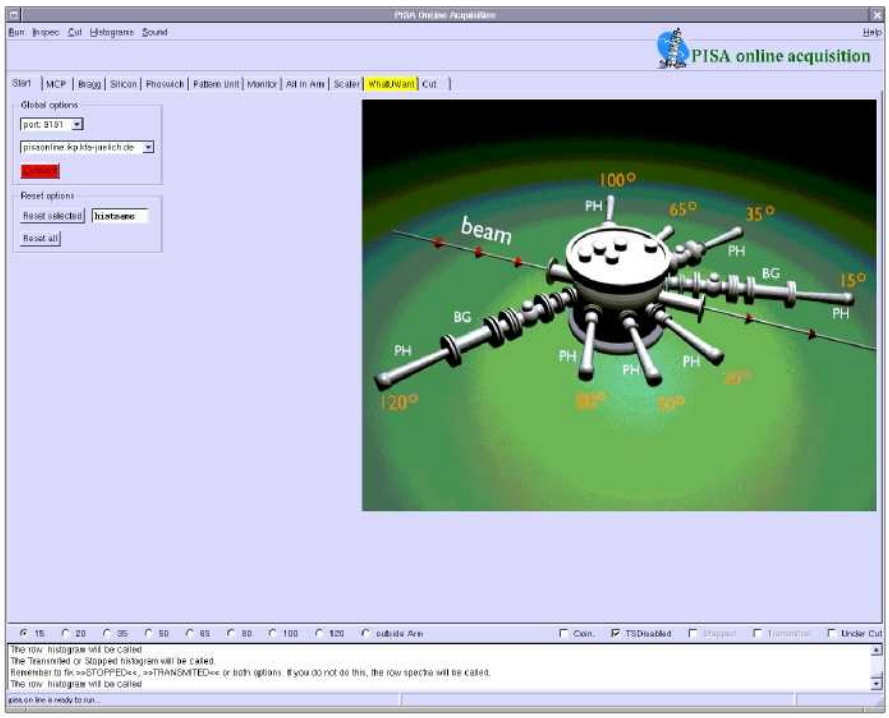

Figure A.2. The screenshot of the "Start" Tab of the HistPresenter program.

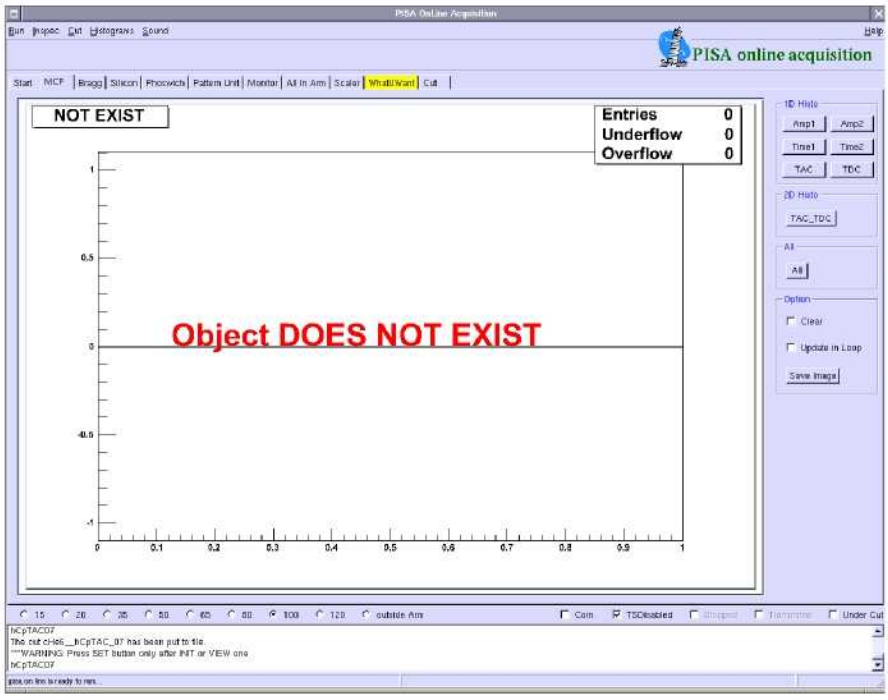

Figure A.3. The screenshot of the "MCP" Tab of the HistPresenter program. The information about lack of requested spectrum is displayed.

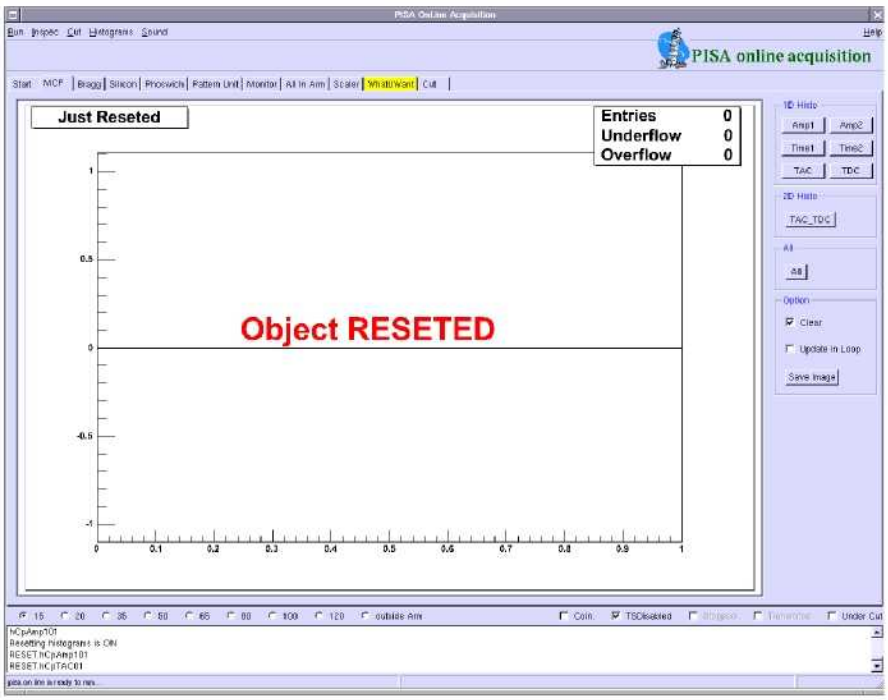

Figure A.4. The screenshot of the "MCP" Tab of the HistPresenter program. The information about reseting of spectrum is displayed.

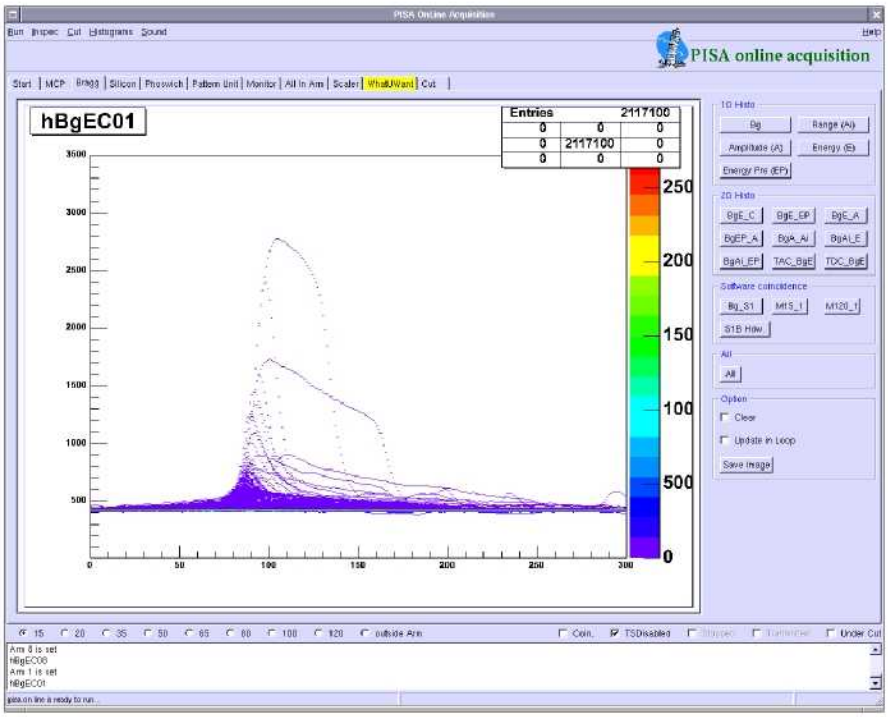

Figure A.5. The screenshot of the "Bragg" Tab of the HistPresenter program. Inside canvas the BC's from the BCD mounted at 15° are shown.

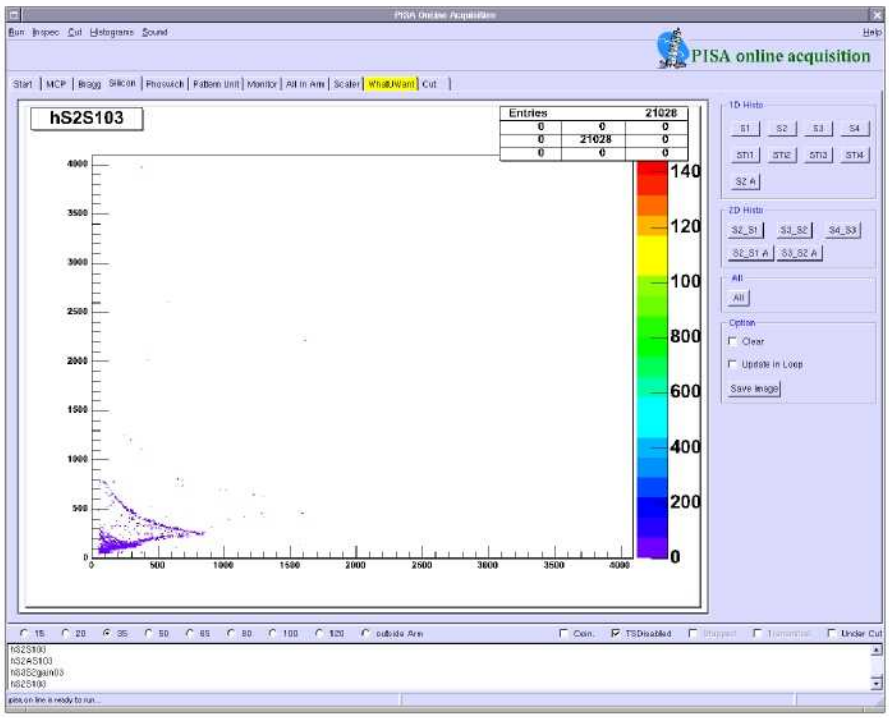

Figure A.6. The screenshot of the "Silicon" Tab of the HistPresenter program. Inside canvas the spectrum of ΔE versus E from two silicon detectors mounted at 35° is shown.

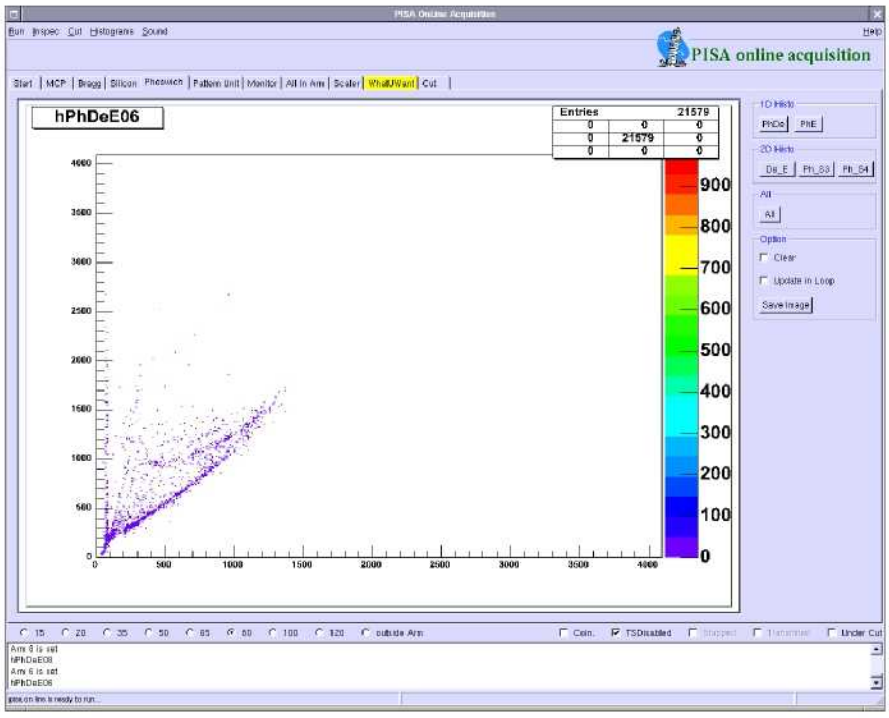

Figure A.7. The screenshot of the the "Phoswich" Tab of the HistPresenter program. Inside canvas the spectrum of ΔE versus E from the phoswich detector mounted at 80° is shown.

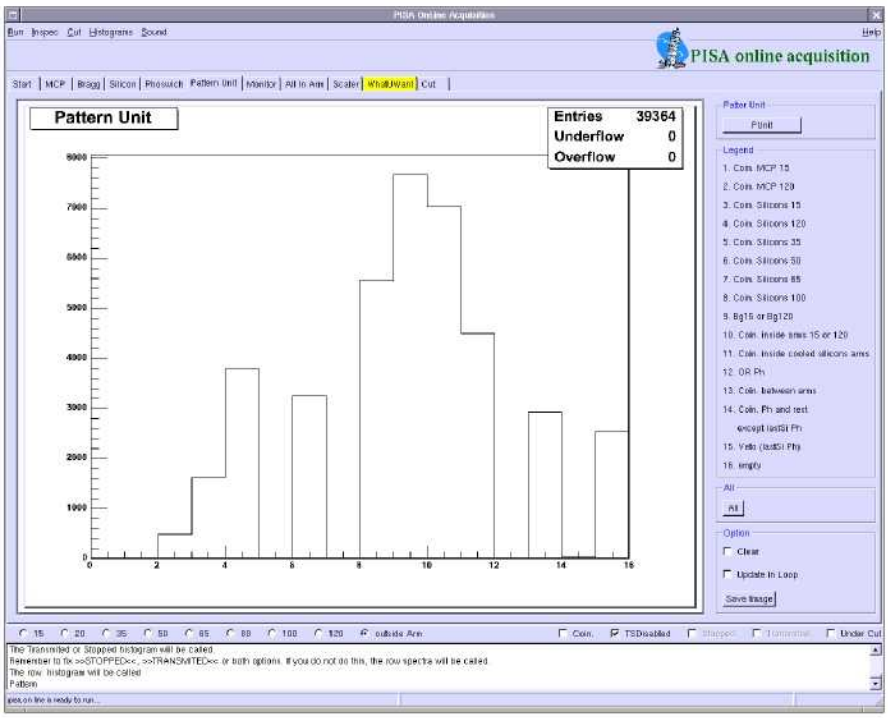

Figure A.8. The screenshot of the "Pattern Unit" Tab of the HistPresenter program.

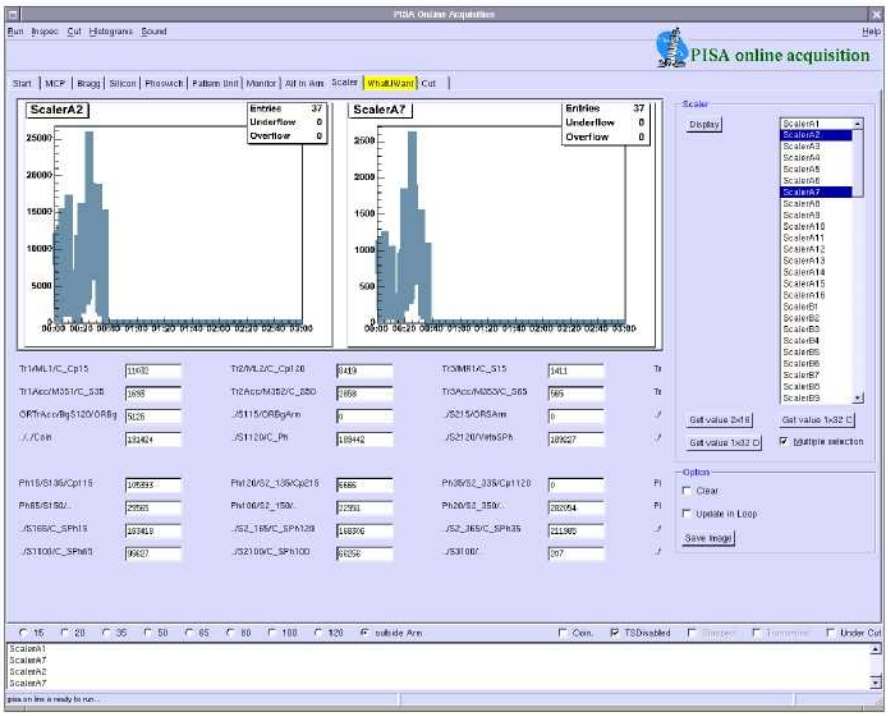

Figure A.9. The screenshot of the "Scaler" Tab of the HistPresenter program.

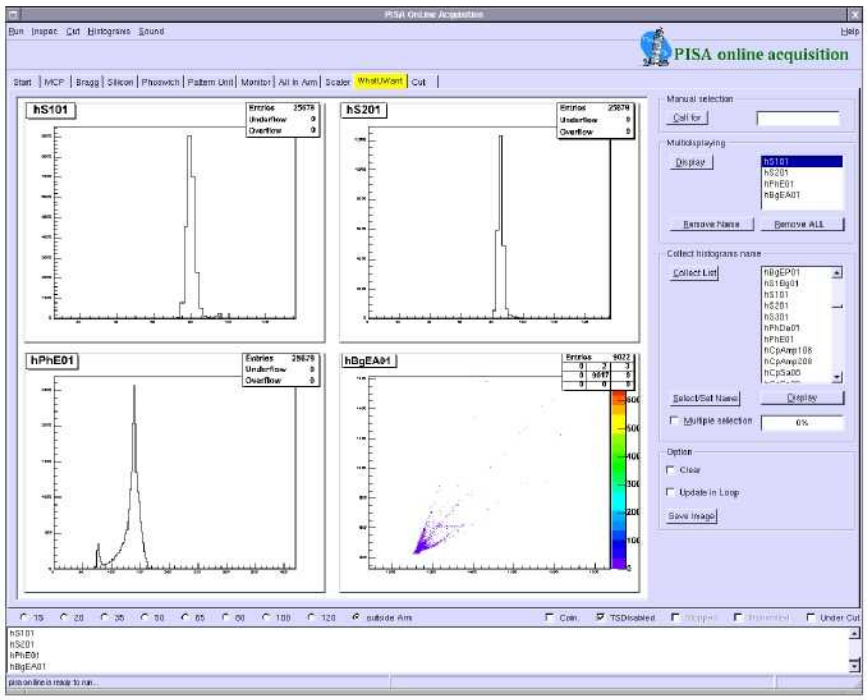

Figure A.10. The screenshot of the "WhatUWant" Tab of the HistPresenter program. Four spectra from various detectors mounted at 15° are shown. Starting from top-left picture in clockwise: spectrum from the first silicon detector mounted directly behind the BCD; spectrum from the second silicon detector; spectrum of E from the phoswich detector; spectrum of the amplitude of the BP versus energy deposited inside the BCD volume.

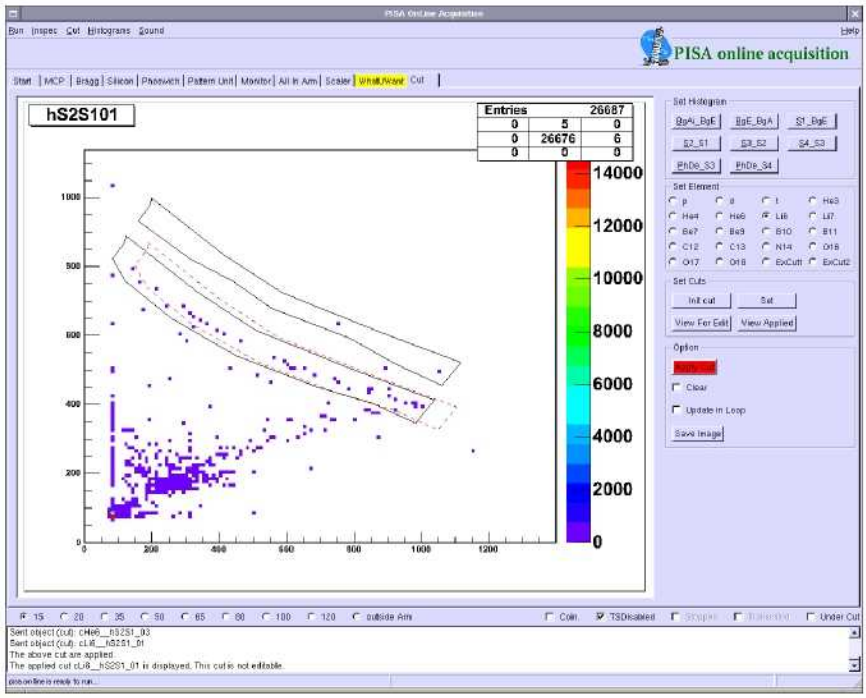

Figure A.11. The screenshot of the "Cut" Tab of the HistPresenter program. An example of graphical cuts on $\Delta E - E$ spectrum from two silicon detectors mounted at 15° are shown.

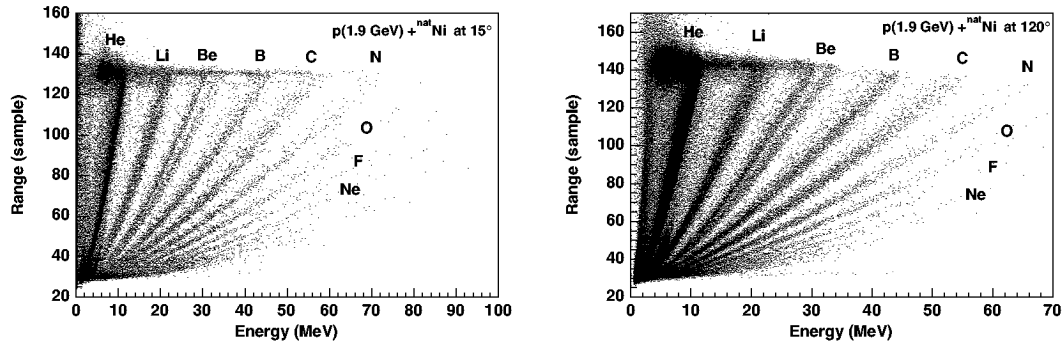

(a) The BCD at 15°

(b) The BCD at 120°

Figure 6.10. Scatter plot of the range versus deposited energy of the particles measured inside the BCD volume mounted at 15° and 120° (cf. Fig. B.3(c) on page 75). The identified reaction products are indicated.

The low energy cutoff in the identification of the particles arises from the detectors thresholds, and from particles energy losses in the foils placed in the front of the BCD. The detector energy threshold is about 0.5 MeV/A and is common for all detected Z (see Fig. 6.12(b) on the following page and Fig. 6.14 on page 43). The dependence of the energy deposited in the BCD volume on the particle incident energy is shown in section B.1 on page 73.

The charge resolution of the BCD at 15° for the fragments stopped inside BCD volume is presented in Fig. 6.11. Because the width of the distribution along the COGs is not constant (width increases with energy) the produced spectra have no Gaussian distribution. The width of the distribution is a function of energy. This effect is shown in Fig. 6.13 on page 43, where the spectra of C and N elements (BCD at 15°), divided into two energy regions, are presented. The energy division is made at 15 MeV for C and 18 MeV for N element. The broadening of the distributions with energy is also shown in Fig. 6.14 on page 43, where the standard deviation of the Gaussian distribution as a function of energy for Li, B, C and N nuclei are presented.

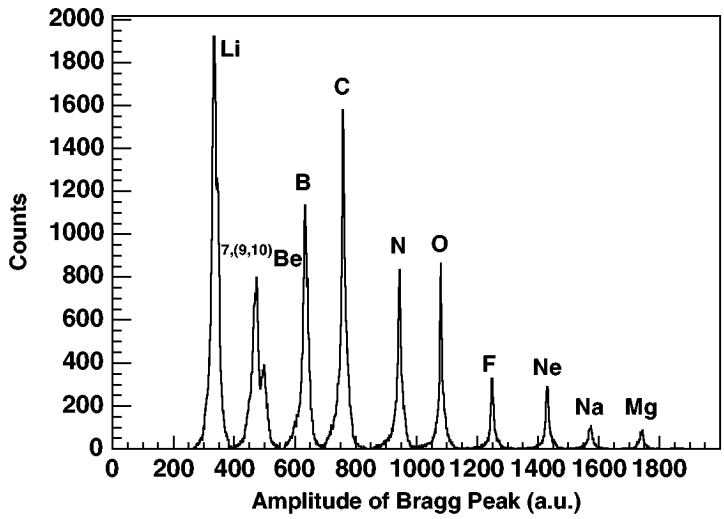

Figure 6.11. Charged products of the p(1.9 GeV) + ^{nat}Ni reaction measured at 15°. The projection of the Z distribution along the centers of gravities is presented (see also Fig. 6.12 on the next page). The beryllium isotopes ($^{7,(9,10)}$Be) are separated thanks to the absence of ^{8}Be.

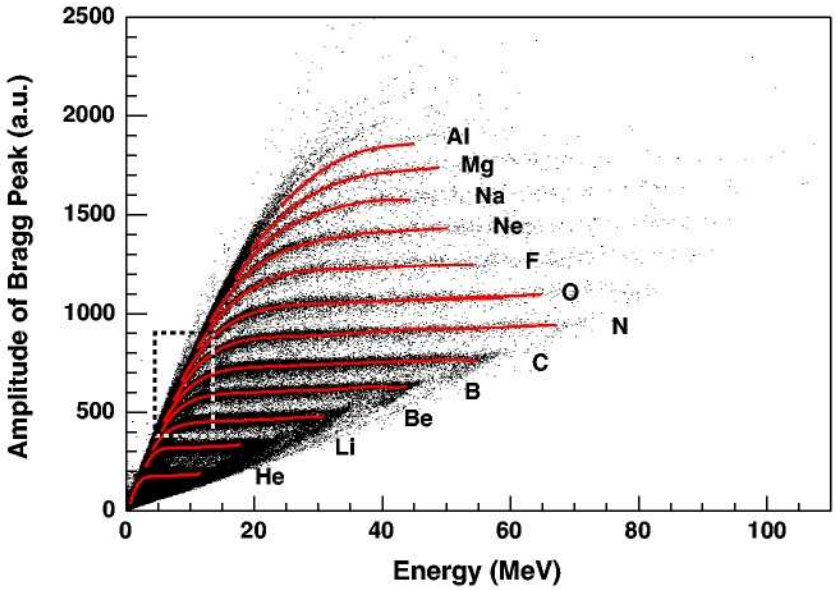

(a) The total area.

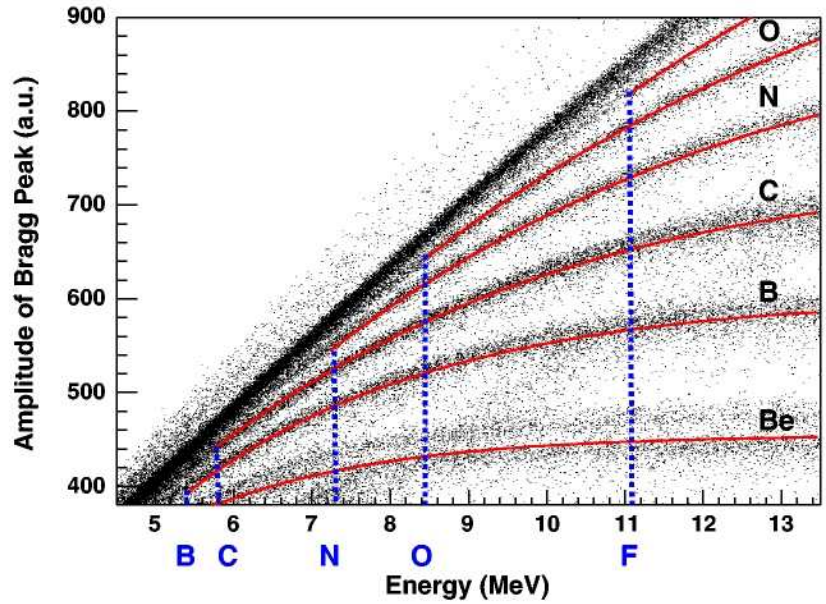

(b) Zoom: the area marked by black-white dashed line in Fig. 6.12(a).

Figure 6.12. (a) Scatter plot of the amplitude of the BP versus the kinetic energy of the registered particles. The p(1.9 GeV) + ^{nat}Ni reaction products were measured at 15°. The line fitted to the centers of gravity of the individual Z distribution are plotted (red continuous lines). For heavier elements, due to the poor statistics at higher energies, the fitted lines do not cover the full stopping energy range of the detector. Both the lower, as well as the upper energy limits used for histogramming (cf. Fig. 6.11 on the preceding page) correspond to the left and right ends of the fitted curve, respectively. (b) The zoom of the rectangular part stressed by dashed-line in figure (a). The lower energy limits, above which the individual elements can be resolved are shown as vertical dashed lines.

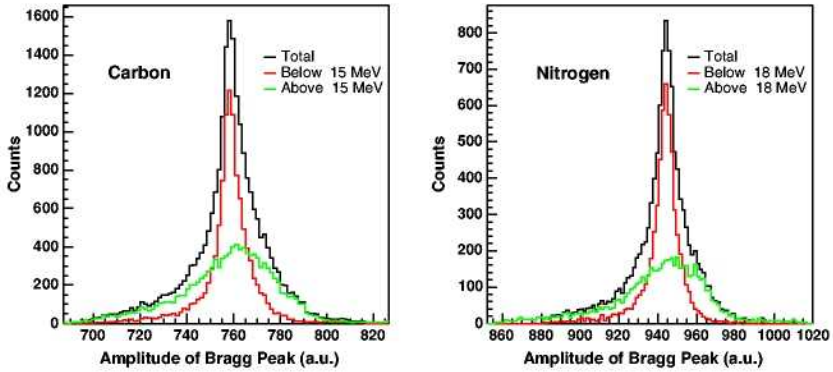

Figure 6.13. The total and partial charge identification spectra for C and N elements. The partial Z identification spectra present the data below and above certain energy (15 MeV for C and 18 MeV for N element). The data are from p(1.9 GeV) + ^{nat}Ni reaction products detected in the BCD at 15°.

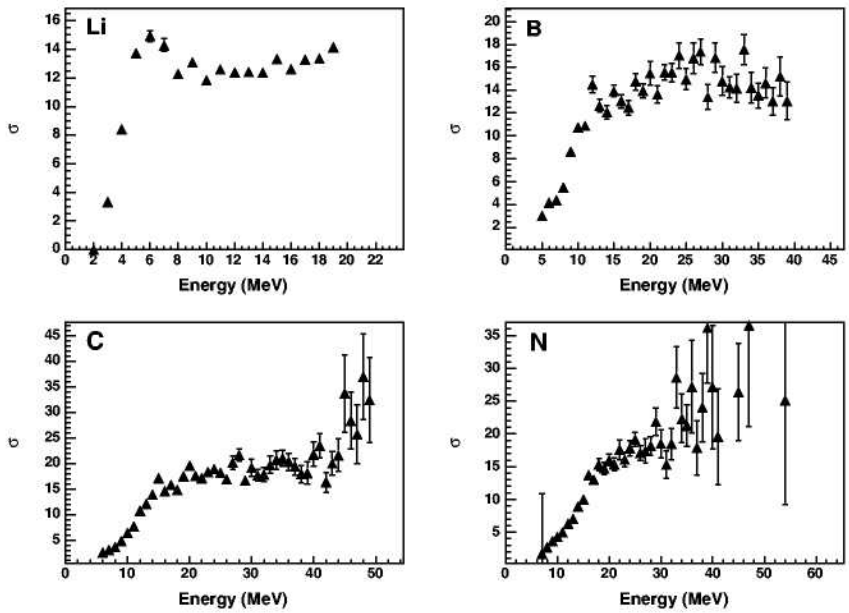

Figure 6.14. The standard deviation of the partial Gaussian charge identification spectrum as a function of energy for Li, B, C and N elements. The data are from p(1.9 GeV) + ^{nat}Ni reaction products detected in BCD at 15°.

6.2.6.2 Identification of the mass number with MCPDs and BCD

The mass separation was done by combining the informations from the MCPDs (time-of-flight) and the BCD (energy deposited inside the BCD volume). With the experimental set-up used and by applying methods described above, separation of following isotopes was possible: ^{6}Li, ^{7}Li, ^{8}Li; ^{7}Be, ^{9}Be, ^{10}Be; ^{10}B, ^{11}B; ^{11}C, ^{12}C, ^{13}C, ^{14}C and ^{13}N, ^{14}N. The energy deposited inside the BCD as a function of the time-of-flight is presented in Figs. 6.15 to 6.16 on the next page together with isotopes separation for 15° and 120°.

In order to obtain the isotope identification spectra, the projections along the line fitted to the COGs of each elements' distribution were performed. The example of lines fitted to the COGs

for Be isotopes, identified at 15° and produced in p(1.9 GeV) + ^{nat}Ni reaction, are shown in Fig. 6.17 on the facing page.

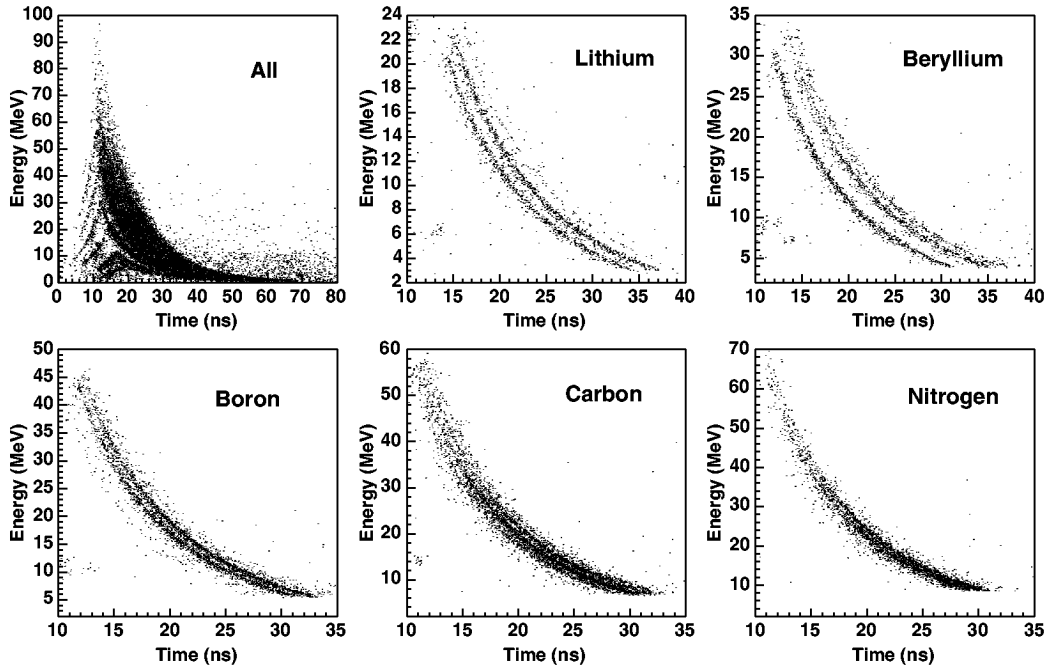

Figure 6.15. Energy deposited inside the BCD volume versus the time-of-flight measured at 15° in p(1.9 GeV) + ^{nat}Ni reaction. The isotope separation is shown.

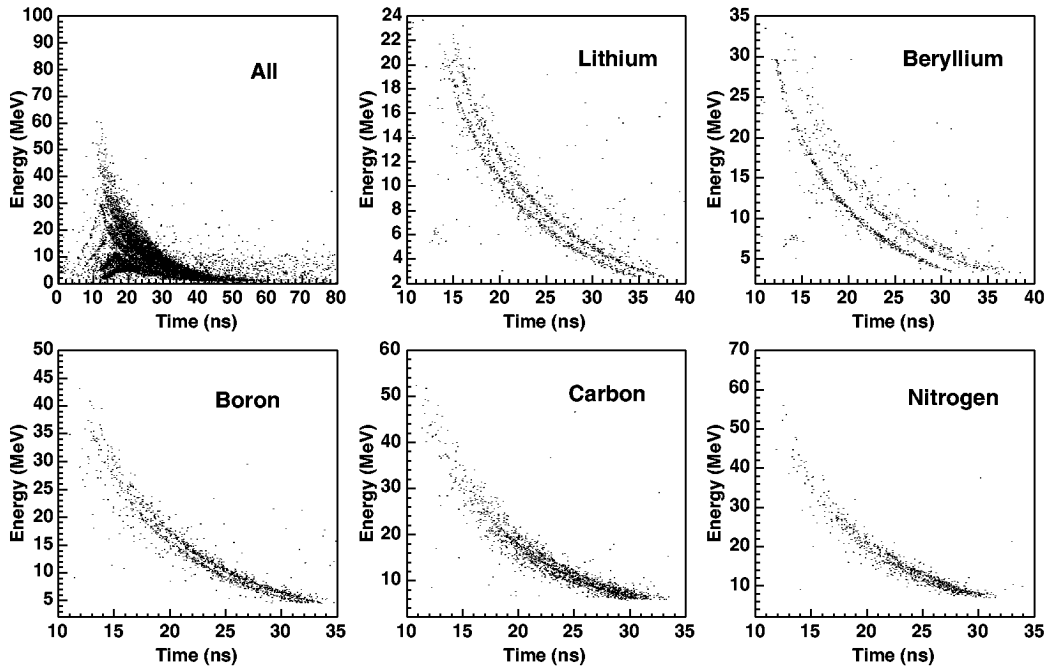

Figure 6.16. Energy deposited inside the BCD volume versus the time-of-flight measured at 120° in p(1.9 GeV) + ^{nat}Ni reaction. The isotope separation is shown.

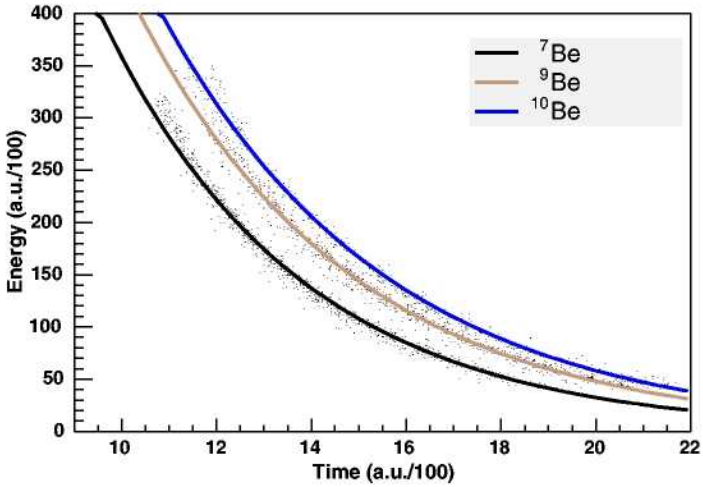

Figure 6.17. The separation of three beryllium isotopes detected at 15° and produced in the p(1.9 GeV) + ^{nat}Ni reaction. The fits to COGs are plotted.

Due to the fact that the lines fitted to the isotopes' COGs of a given element are not parallel (see Fig. 6.17), the projections along various centers of gravity are not the same. Therefore, in order to obtain identification spectra of different isotopes, the projections were performed along each COG of a given element separately. The final choice of the COG was done by the inspection of each projection. The best possible isotope separation was obtained when the projections along the COGs of ^{7}Li, ^{9}Be, ^{11}B, ^{12}C and ^{14}N were chosen. The results are shown in Fig. 6.18 and Fig. 6.19 on the next page.

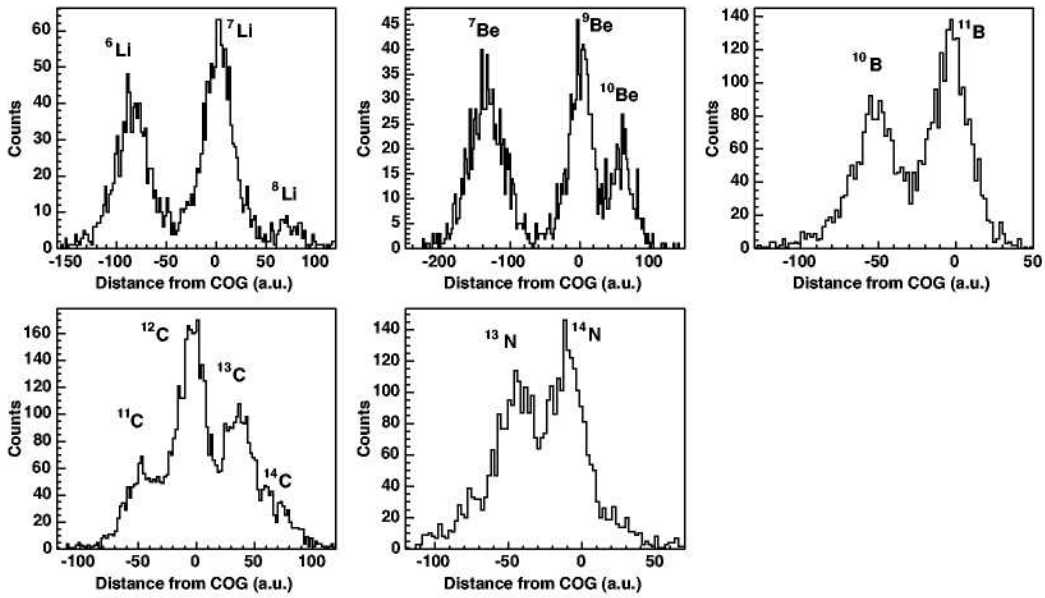

Figure 6.18. The mass identification spectra of the p(1.9 GeV) + ^{nat}Ni reaction products measured at 15° obtained by the projection of the mass distributions along the centers of gravities of ^{7}Li, ^{9}Be, ^{11}B, ^{12}C and ^{14}N.

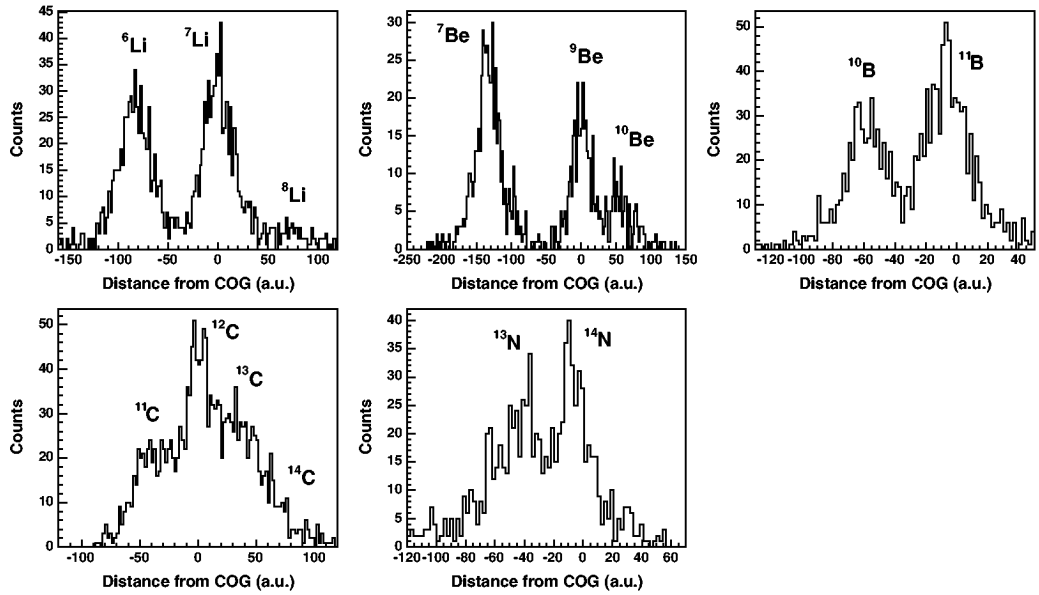

Figure 6.19. The mass identification spectra of the p(1.9 GeV) + ^{nat}Ni reaction products measured at 120° obtained by the projection of the mass distribution along the centers of gravities of ^{7}Li, ^{9}Be, ^{11}B, ^{12}C and ^{14}N.

6.2.6.3 Identification of the mass number with BCD

As it has been discussed in section 6.1 on page 33 the MCPDs efficiency in the charge range $2 \leqslant Z \leqslant 10$ varies from about 1.5% to 60% and 30% for 15° and 120°, respectively (assuming 100% efficiency of the BCD). Therefore it is extremely important to find a method which allows to distinguish particles' masses with the BCD only, even if there are no signals from MCPDs. The following methods have been tested: (i) the pulse shape discrimination method (PSD) was used for the data when only events from the BCD exist, and (ii) the reference shape method (RSM) for the data from both BCD and MCPD. Both methods are described below.

Pulse shape discrimination method

The pulse shape discrimination (PSD) technique, usual applied to scintillator detectors, can be also used in the BC analysis. Fig. 6.20 on the next page shows the relations between ΔE and E, where E is the total energy obtained by the integration of the whole area under the BC, whereas ΔE is the energy integrated over the restricted area of the BC. The resolving power of the PSD strongly depends on the area chosen for the ΔE integration. The best isotopes identification was obtained for $(\mathrm{MAXC} - 45) < \Delta E < (\mathrm{MAXC} - 10)$, where MAXC is sample's number for the minimum of the derivative (see Fig. 6.3 on page 35). This method allows for the separation of Li, Be and B isotopes within certain range of energy. Due to the lack of the mass identification, the elements heavier than $Z = 6$ are not shown in Fig. 6.20 on the next page.

Reference shape method

The reference shape method relies on looking for the average BC (reference BC (RBC), reference shape) for a given isotope. It was assumed that the RBCs are different for each isotope. In contrast to the PSD, this method can not be applied by using the BCD data only. For the determination of the reference curves the isotope distinction is required. Therefore signals registered by both MCPDs and BCD are needed.

In order to create the RBCs two different methods were tested:

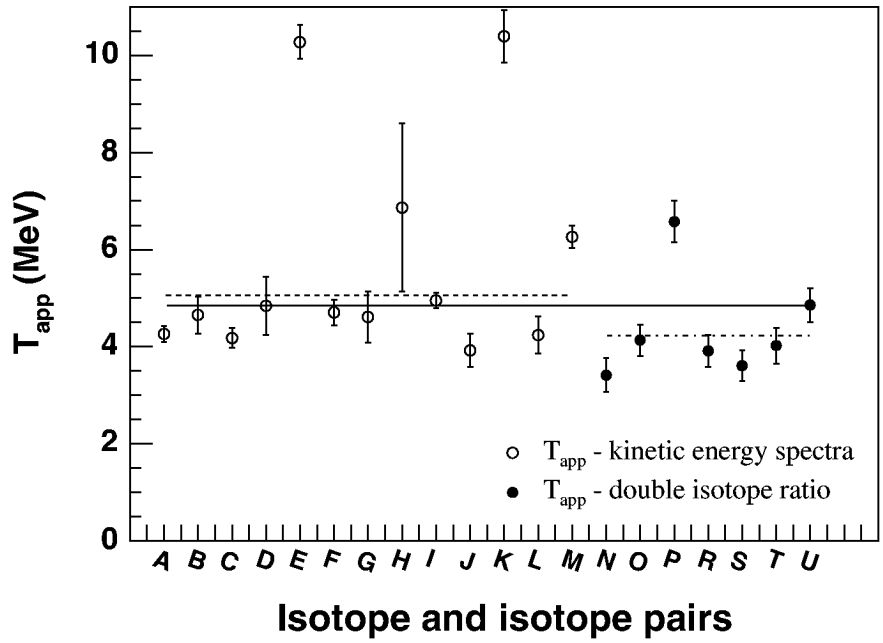

Figure 6.32. Comparison of apparent temperatures evaluated from two different methods. The open circles are T_{app} obtained from the slopes of the kinetic energy spectra, whereas full circles are from the double isotope ratio method. The straight lines are fits curves. The dashed line is the fit to the data extracted from the slope of the kinetic energy spectra, the dot-dashed line is the fit to the T_{app} values evaluated from the double isotope ratio and the solid line is the fit to temperatures from both methods. Letters on the x axis indicate the isotope or isotope ratio used **A**: (^{6}Li), **B**: (^{7}Li), **C**: (^{7}Be), **D**: (^{9}Be), **E**: (^{10}Be), **F**: (^{10}B), **G**: (^{11}B), **H**: (^{11}C), **I**: (^{12}C), **J**: (^{13}C), **K**: (^{14}C), **L**: (^{13}N), **M**: (^{14}N), **N**: (^{13}C/^{14}C)/(^{11}C/^{12}C), **O**: (^{6}Li/^{7}Li)/(^{11}C/^{12}C), **P**: (^{9}Be/^{10}Be)/(^{11}C/^{12}C), **R**: (^{12}C/^{13}C)/(^{11}C/^{12}C), **S**: (^{7}Li/^{8}Li)/(^{11}C/^{12}C), **T**: (^{7}Li/^{8}Li)/(^{13}C/^{14}C), **U**: (^{10}B/^{11}B)/(^{11}C/^{12}C).

6.5 Caloric curve

The caloric curve (CC) which relates the excitation energy of nucleus at thermodynamic equilibrium to its temperature is the simplest experimental tool to look for the existence of the phase transition. The CC shows the feature of the first order liquid-gas phase transition, with almost constant temperature of nuclear matter for excitation energies between 3 and 10 MeV/A. The CC presented in Fig. 6.33 on the next page was obtained from numerous data from Refs. [25, 27, 55, 56, 164, 169–177]. The data from the PISA measurement are included as well. Both values of apparent temperature which were used for the enrichment of the existing CC are average temperatures (T_{ave}) extracted from the slope of the kinetic energy spectra and the double yields ratio of emitted particles (cf. section 6.4.3 on the facing page). It has to be noticed, that we extracted the apparent temperature, which is not exactly the temperature of the nuclear matter, but it is only related to it.

The values of the excitation energy E^* of residues in the p(1.9 GeV) + ^{nat}Ni reaction was obtained by calculations performed with the theoretical Liège intranuclear cascade (INCL) model [46, 47], version 4.2 [178]. In this version of the code a new method of the determination of the time at which the intranuclear cascade stops (t_{stop}), and gives way to the evaporation, is proposed. At t_{stop} many physical quantities as E^*, average kinetic energy of ejectiles, or asymmetry of the participant momentum distribution are determined. This new method of the t_{stop} determination gives approximately two times larger value of the t_{stop} than obtained in the previous code version. Moreover, some physical observables as neutron or proton multiplicity, or E^* seems to be not correctly determined at this new value of t_{stop} [179]. Therefore in our

calculations the excitation energy was determined after $t_{stop}/2$, which is according to the author of the INCL code more realistic.

The yield distributions of the excitation energy per nucleon E^*/A are presented in Fig. 6.34. The average value of $E^*/A = 3.8 \pm 0.1$, indicated in Fig. 6.34 by dashed line was used for the construction of the caloric curve.

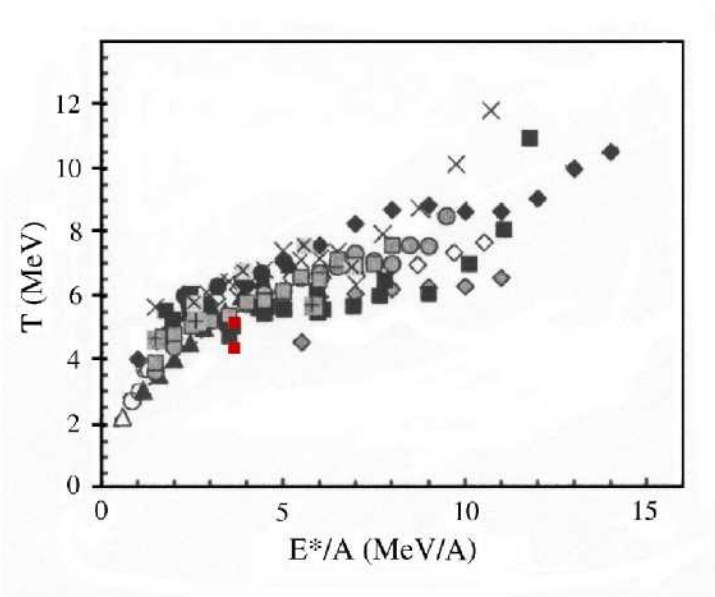

Figure 6.33. Caloric curve: temperature of the nucleus versus excitation energy per nucleon. The symbols correspond as follow: open circles - Ref. [55]; solid black circles - Ref. [164]; solid black diamonds - Ref. [56]; open square - Ref. [169]; solid black squares - Ref. [170]; solid black diamonds (^{84}Kr), open diamonds (^{134}La) and shaded diamonds (^{197}Au) - Ref. [171]; shaded triangles - Ref. [27]; cross in shaded squares - Ref. [25] and references therein; shaded circles (Ag) and shaded squares (^{197}Au) - Refs. [172–174]; $\times$ in shaded squares - Refs. [175, 176]; $\times$s - Ref. [177]. The results of the PISA measurement are presented by the solid red squares.

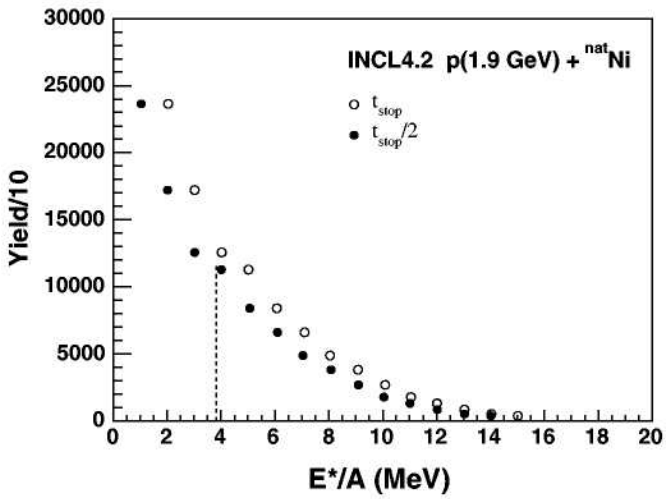

Figure 6.34. Population of the excitation energy per nucleon (E^*/A) calculated within the Liège intranuclear cascade model (INCL). Calculations from the INCL4.2 (t_{stop}) and INCL4.2-modified ($t_{stop}/2$) are shown.

Appendix A

Screenshots from the HistPresenter and the decoder programs.

In the present section a few screenshots from the decoder and HistPresenter program are shown. The screenshots from decoder program are shown in Fig. A.1, whereas in Figs. A.2 to A.11 on pages 68–72 the screenshots from HistPresenter program are presented. Both programs belong to the PISA software package. More details about applicability and functionality of the programs can be found in section 4.2.1 on page 25 and 4.2.3 on page 28.

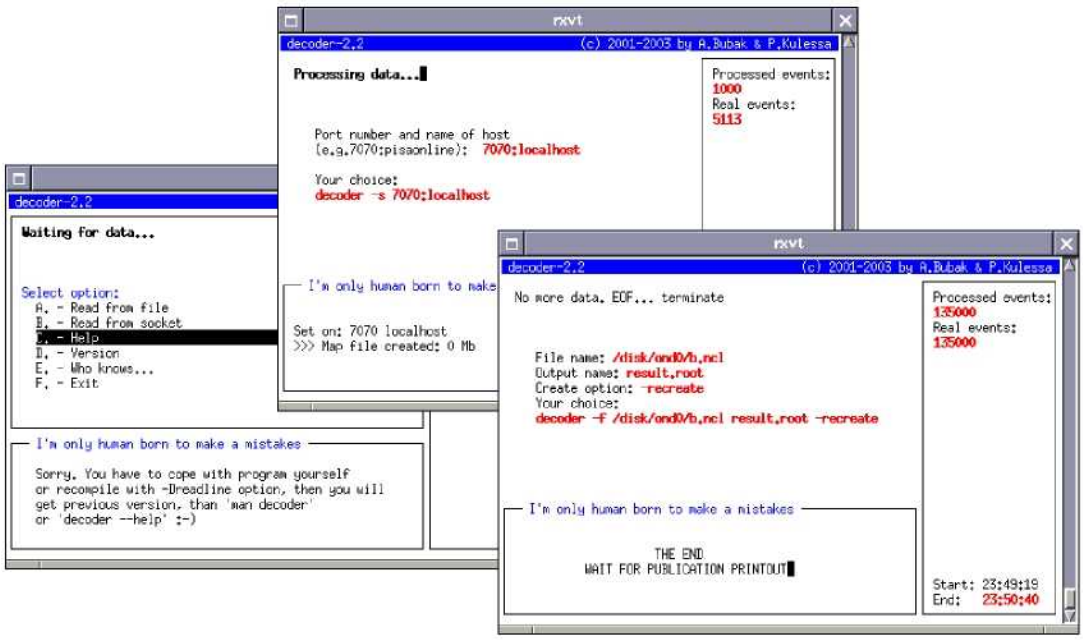

Figure A.1. The screenshots of frontend to the decoder program. Three panels from left-bottom to right-top: the start panel; panel associated with the on-line mode; panel associated with the off-line mode. The frontend is written with ncurses library routines.

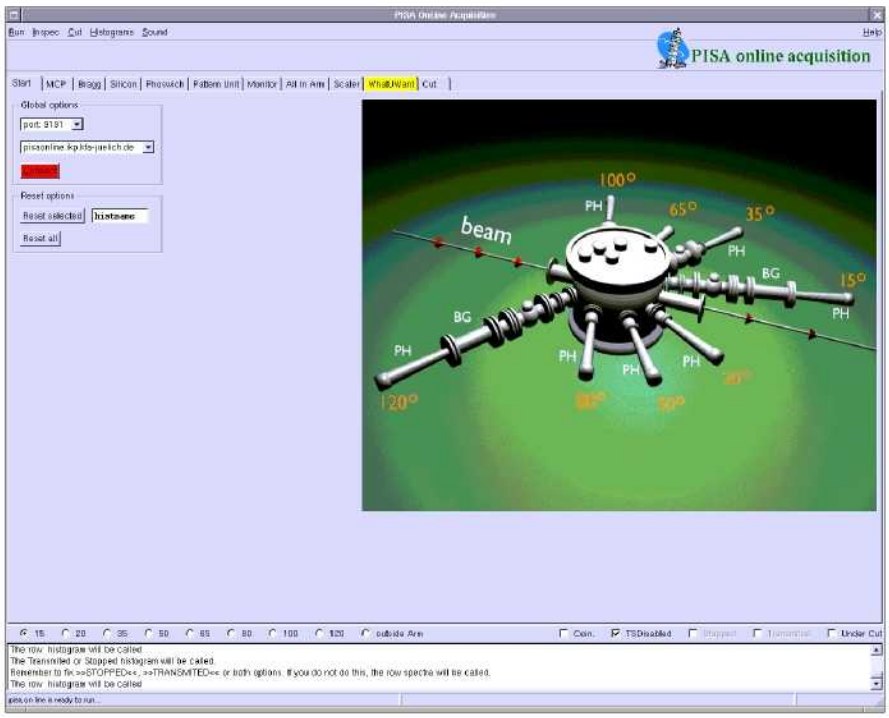

Figure A.2. The screenshot of the "Start" Tab of the HistPresenter program.

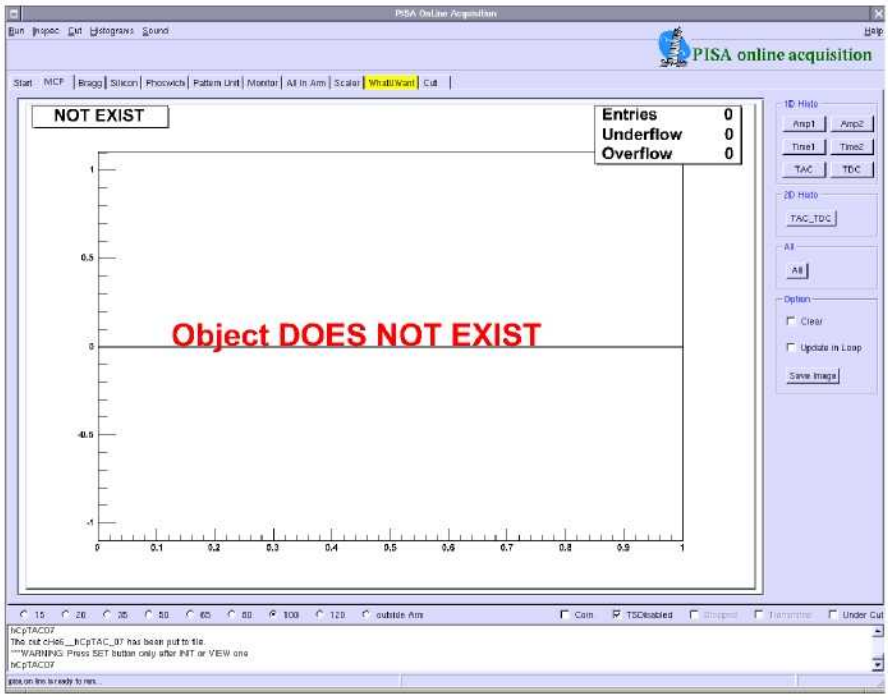

Figure A.3. The screenshot of the "MCP" Tab of the HistPresenter program. The information about lack of requested spectrum is displayed.

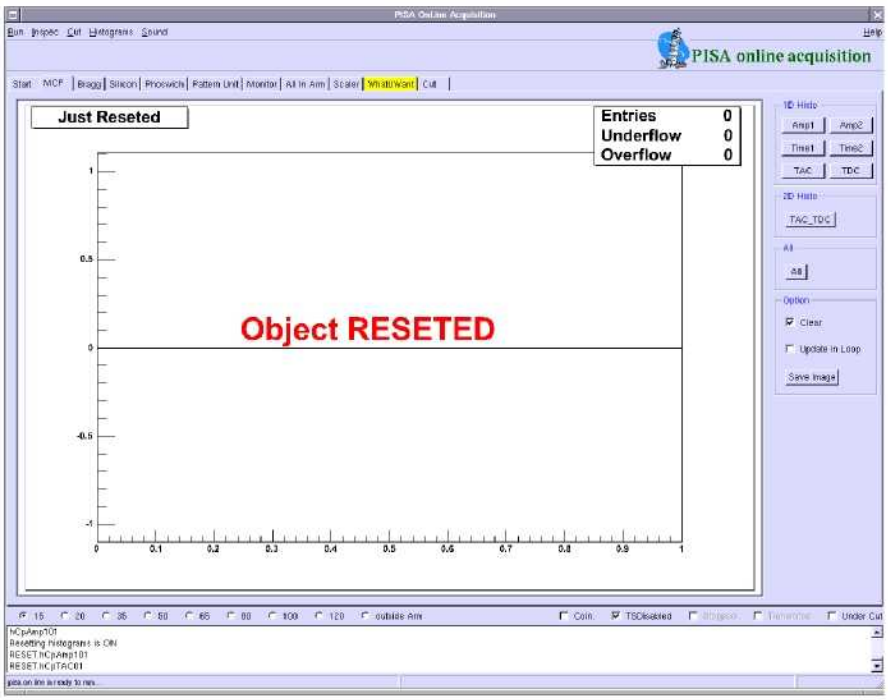

Figure A.4. The screenshot of the "MCP" Tab of the HistPresenter program. The information about reseting of spectrum is displayed.

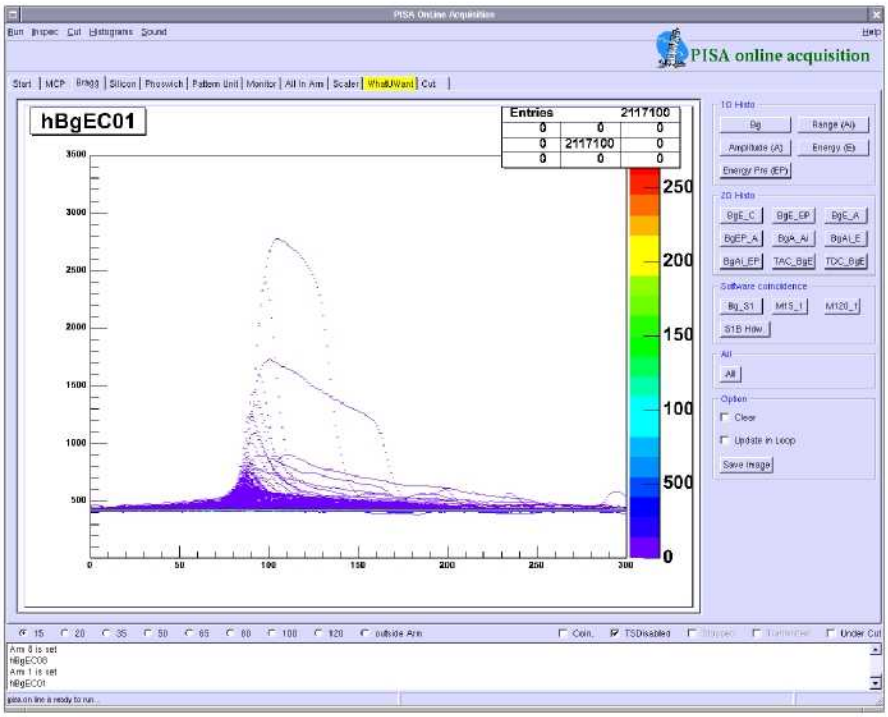

Figure A.5. The screenshot of the "Bragg" Tab of the HistPresenter program. Inside canvas the BC's from the BCD mounted at 15° are shown.

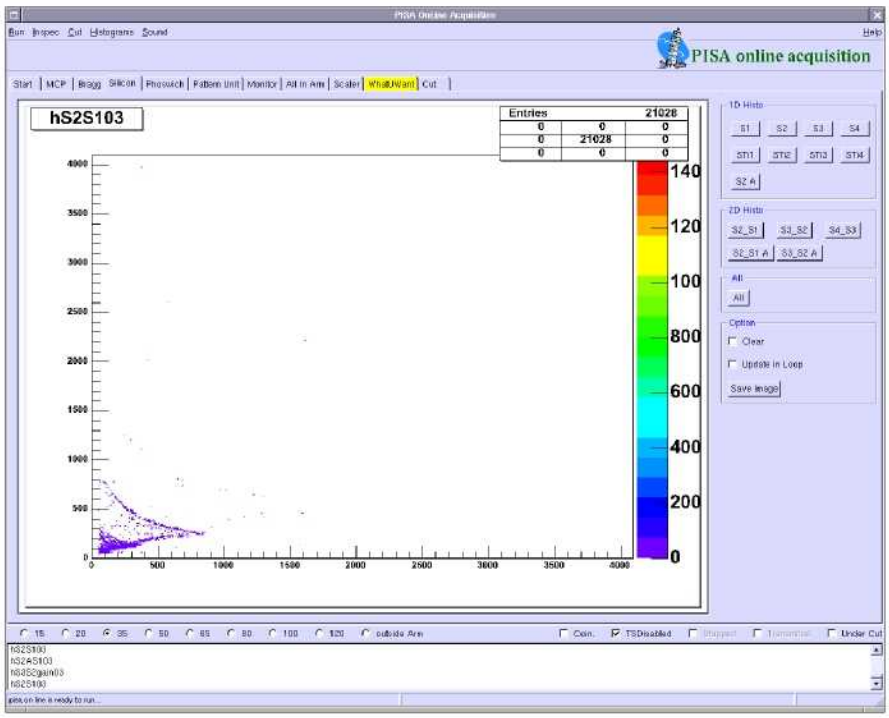

Figure A.6. The screenshot of the "Silicon" Tab of the HistPresenter program. Inside canvas the spectrum of ΔE versus E from two silicon detectors mounted at 35° is shown.

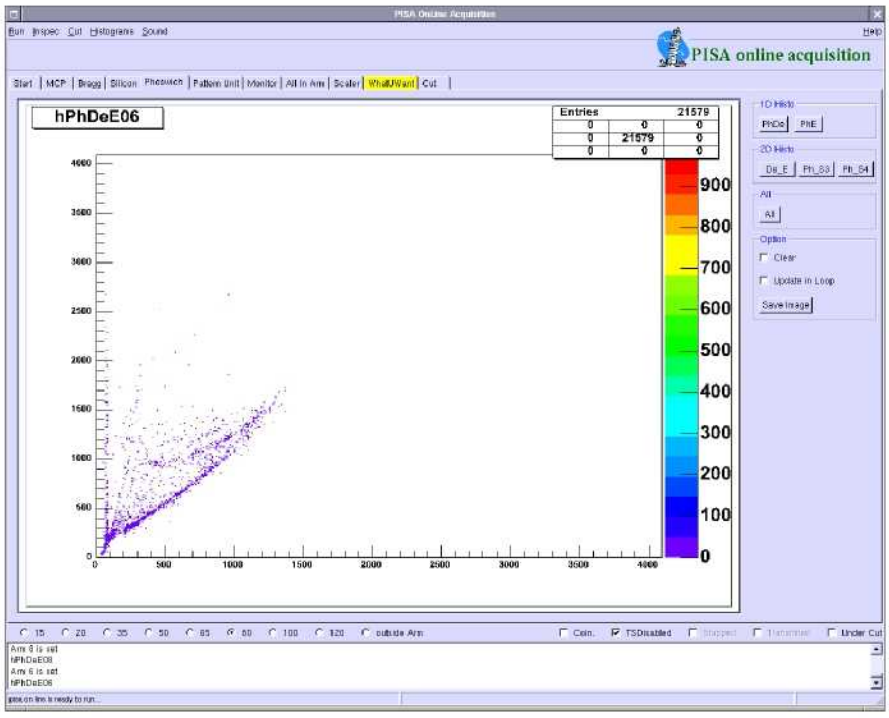

Figure A.7. The screenshot of the the "Phoswich" Tab of the HistPresenter program. Inside canvas the spectrum of ΔE versus E from the phoswich detector mounted at 80° is shown.

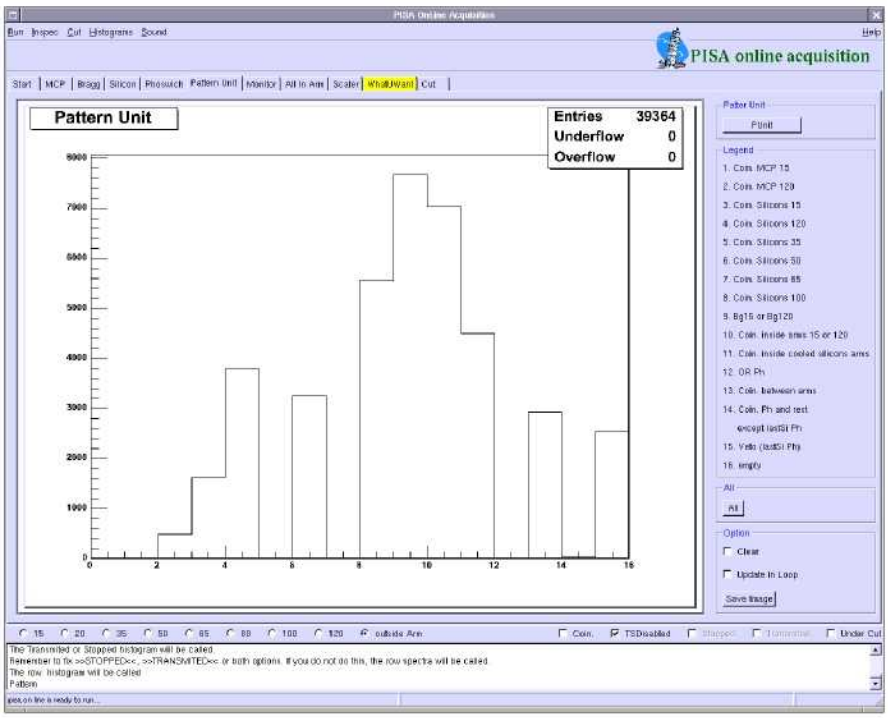

Figure A.8. The screenshot of the "Pattern Unit" Tab of the HistPresenter program.

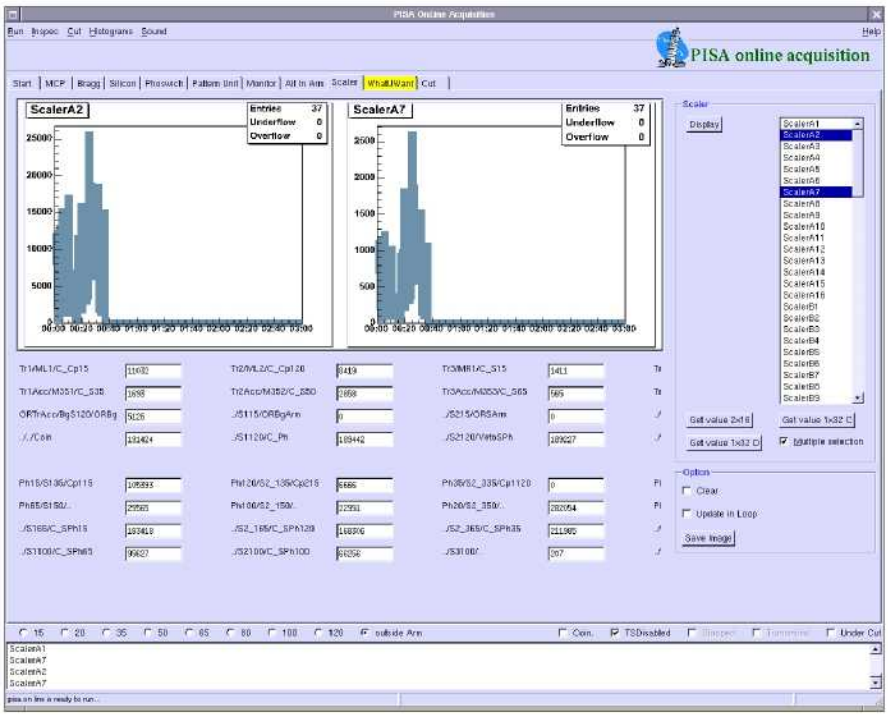

Figure A.9. The screenshot of the "Scaler" Tab of the HistPresenter program.

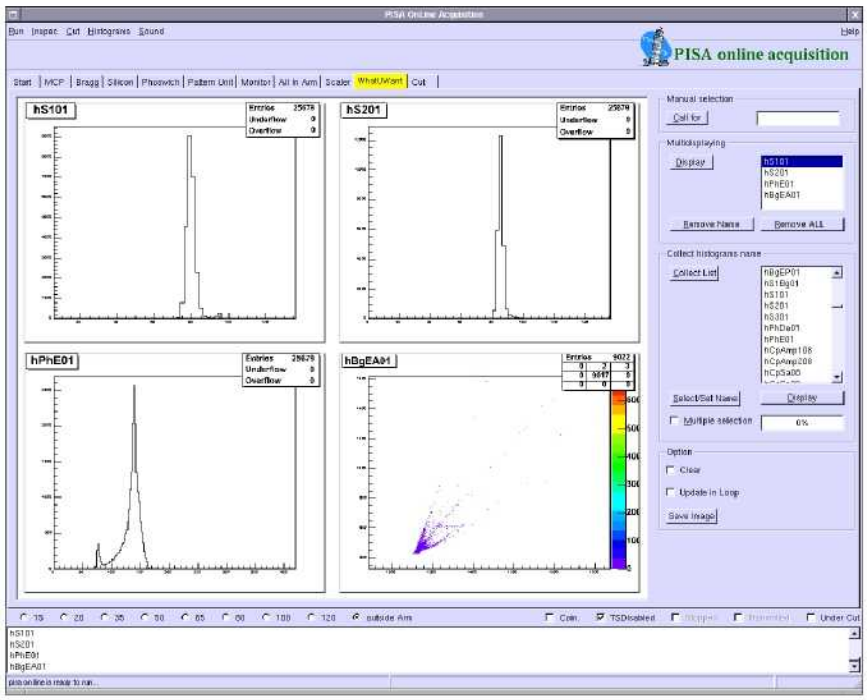

Figure A.10. The screenshot of the "WhatUWant" Tab of the HistPresenter program. Four spectra from various detectors mounted at 15° are shown. Starting from top-left picture in clockwise: spectrum from the first silicon detector mounted directly behind the BCD; spectrum from the second silicon detector; spectrum of E from the phoswich detector; spectrum of the amplitude of the BP versus energy deposited inside the BCD volume.

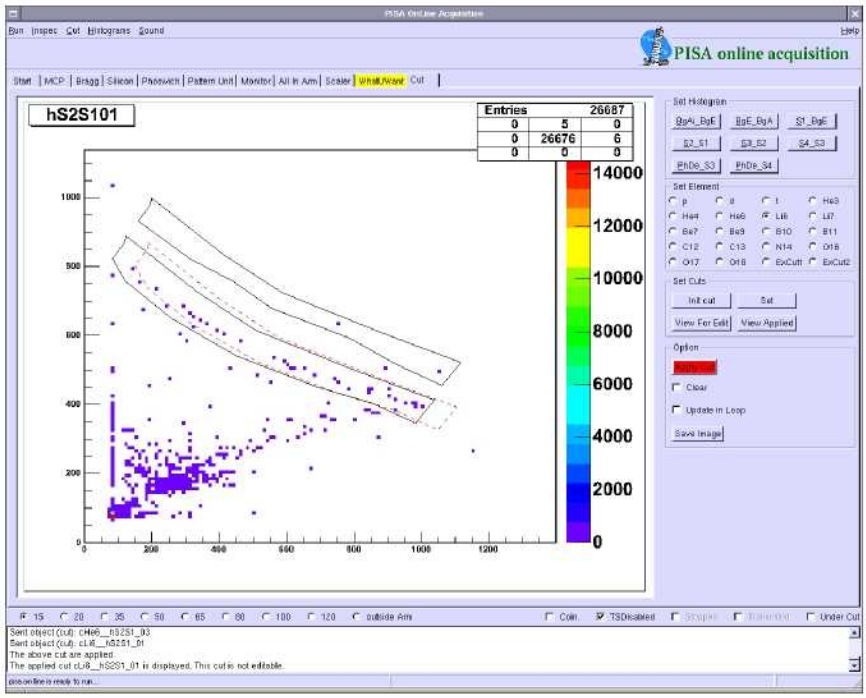

Figure A.11. The screenshot of the "Cut" Tab of the HistPresenter program. An example of graphical cuts on $\Delta E - E$ spectrum from two silicon detectors mounted at 15° are shown.

The example of PTPs used in the calibration procedures, and obtained from the experimental data, are presented in Fig. 6.6 on the preceding page. The simulation was carried out with the Geant4 simulation toolkit [63].

The relation between the energy value in PTPs from both simulated and experimental data gives energy calibration function. The fits to the energy calibration points for the BCDs at 15° and 120° are presented in Fig. 6.7.

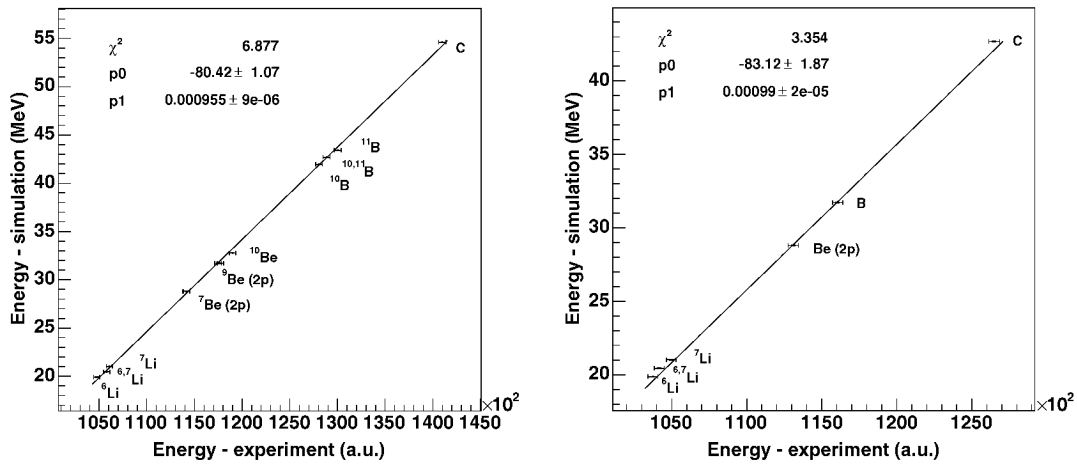

(a) BCD at 15°

(b) BCD at 120°

Figure 6.7. The energy calibration functions for BCDs at 15° and 120°. The parameters of the fitted functions (straight lines) are presented.

6.2.6 Atomic and mass number identification

The methods of the identification of the atomic and mass numbers of the products of the reaction p(1.9 GeV) + ^{nat}Ni are presented. The charge identification of the nuclei was performed with the BCDs, whereas mass identification by combining information from the BCD and MCPD.

6.2.6.1 Identification of the atomic number with BCD

The identification of the atomic number of the nuclei registered by the BCD is possible by inspection of the relationships between the Bragg curve parameters. In Fig. 6.8 on the next page the relation between the Bragg peak (BP) and energy deposited inside the BCD is shown, whereas the BP as a function of the range of particles is shown in Fig. 6.9 on the following page. The events with the same nuclear charge are located in branches parallel to the energy (and range) axis and correspond to the particles stopped inside the BCD volume. The distinction of the charge is visible in the range $2 \leqslant Z \leqslant 14$ and $2 \leqslant Z \leqslant 11$ at 15° and 120°, respectively. Two dimensional plots showing the range versus energy for the same data are shown in Fig. 6.10 on page 41.

One can notice that highly energetic particles with $Z \leqslant 6$ at 15° and $Z \leqslant 4$ at 120° have the range greater than the length of the BCD. This effect is very well visible in the Fig. 6.8 on the following page, where particles which cross the BCD lie on the return branches.

The slight variation of the slope of the BP amplitude with energy (see Fig. 6.8 on the next page) and with range (see Fig. 6.9 on the following page) was reported also in earlier works describing the general features of the Bragg curve spectroscopy [151–155]. This effect is caused by the recombination of electrons and inefficiency of the Frish grid [151,153]. It is also very well

visible in Fig. 6.4(b) on page 36, where the BCs of ^{6}Li and ^{7}Li are shown.

In order to obtain the charge identification spectra, the projection onto the BP amplitude axis, along the line fitted to the centers of gravity (COG) of each element distribution, was done. The coordinates of the centers of Z distributions are taken as the upper limits of the fitted line in Fig. 6.12(a) on page 42. The lines fitted to the COGs for each element for the data from the BCD at 15° are shown in Fig. 6.12 on page 42.

Due to the fact that the width of the charge distribution is a function of energy, instead of FWHM the standard deviations were calculated for each of the individual Z lines as the element's resolution (ΔZ). It is found that ΔZ varies between 10% and 12% per charge unit for peaks where isotopes are not distinguished, and 14% for Be where the isotopical structure is visible.

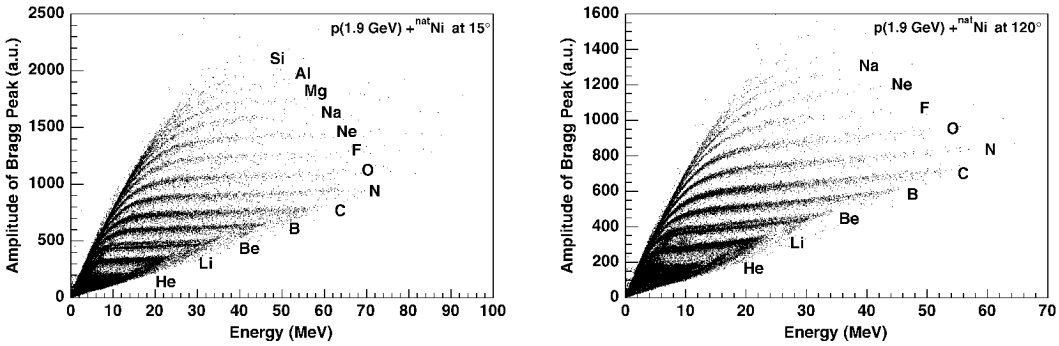

(a) The BCD at 15°

(b) The BCD at 120°

Figure 6.8. Scatter plot of the amplitude of the BP versus energy deposited in the BCD for p(1.9 GeV) + ^{nat}Ni reaction products measured with BCD mounted at 15° and 120° (cf. Fig. B.3(a) on page 75). The identified reaction products are indicated.

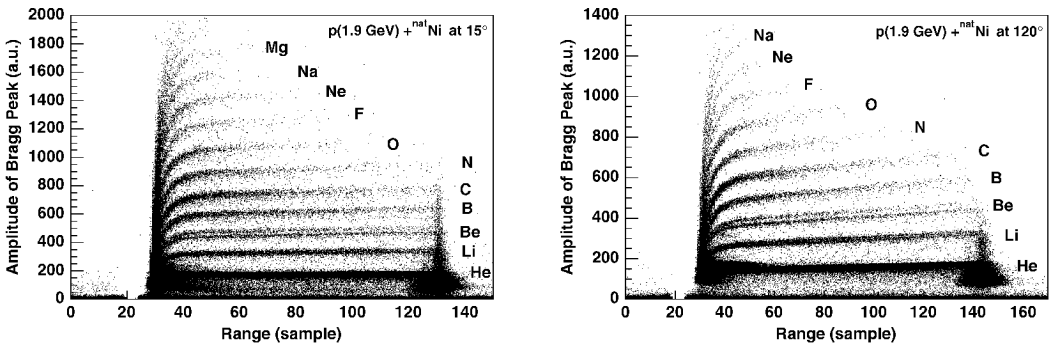

(a) The BCD at 15°

(b) The BCD at 120°

Figure 6.9. Scatter plot of the BP amplitude versus range of the particles measured inside the BCD volume mounted at 15° and 120° (cf. Fig. B.3(b) on page 75). The identified reaction products are indicated.

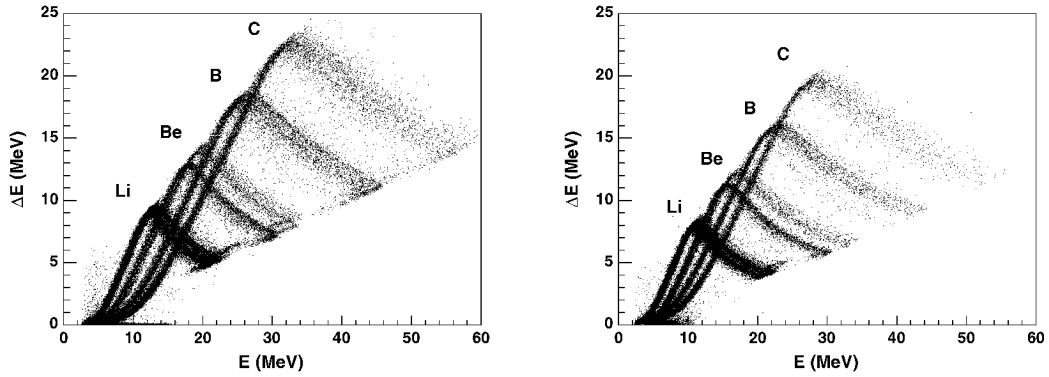

(a) BCD at 15° (b) BCD at 120°

Figure 6.20. Isotopic resolution obtained from the BC only. With the PSD method, the identification of Li, Be and B isotopes was possible.

1. **Single RBC method** [156]
   After isotope selection by the time-of-flight technique, single RBC for each isotope has been created. The RBCs for Li, Be, B, C and N isotopes obtained with this method are shown in Fig. 6.21 on the following page. The reference Bragg curves for different isotopes are well separated. This method is valid only under assumption that the maximum of the BC (i.e. BP) is constant for a given isotope. Unfortunately, it was observed that the value of the maximum of the Bragg curve increases with the range of the particle inside the BCD volume and with the deposited energy (see Fig. 6.4(b) on page 36 and section 6.2.6 on page 39). It indicates that the disturbance of the BP is inversely proportional to the particles' penetration depth in the BCD volume. The correction for that was done assuming that each point of the BC behaves in the same way as the BP.

2. **Multiple RBC method**
   This method assumes that the RBC is a function of the particles' range inside the BCD volume. It means that for a given isotope several reference shapes have to be created. The RBCs have been obtained by taking into account more than 50 BC.

The RBCs, in both methods, were obtained for "raw" and "smoothed" curves. The BC smoothing methods are described in section 6.2.2 on page 36.

The reference shape for a given isotope registered by the BCD has been chosen by applying the χ^2 criterion:

$$\chi^2 = \sum_{i=1}^{N} \frac{(Q_i - R_i)^2}{\sigma_i}, \tag{6.1}$$

where σ_i is a standard deviation and is equal to $\sqrt{R_i}$, Q_i corresponds to the curve which is tested, and R_i is a RBC. The summation is performed over all N samples of the BC. This χ^2 criterion method should unambiguously ascribe tested Bragg curve to the RBC corresponding to a given isotope.

The efficiency of both methods was calculated by the so called "cross check" technique. The "cross check" technique relies on using for the reference shape method the curves which were used for the creation of the referencing curves. The overall efficiency of the "multiple RBC method" is about 70%, whereas the efficiency of the "single RBC method" is about 10%. The detailed results of the identification efficiency of a given isotope with the "multiple RBC method" are

presented in Tab. 6.1 on the facing page. Except ^{9}Be isotope there is practically no distinct difference between "raw" and "smoothed" curves.

The results of the χ^2 criterion in the "cross check" method performed for ^{6}Li and ^{7}Li isotopes are shown in Fig. 6.22 on the next page.

The "multiple RBC method" was later used not only to the signals registered by both MCPDs and BCD (partial test), but also to all BCs (total test). The isotopes' ratio from the partial and total tests, as a quantity determining the agreement between them, was proposed. The results are shown in Tab. 6.2 on the facing page. The conformity is only restricted to the isotopes for which the efficiency of identification by the χ^2 criterion in "cross check" method exceeds 60% (cf. shaded rows in Tab. 6.2 on the next page.)

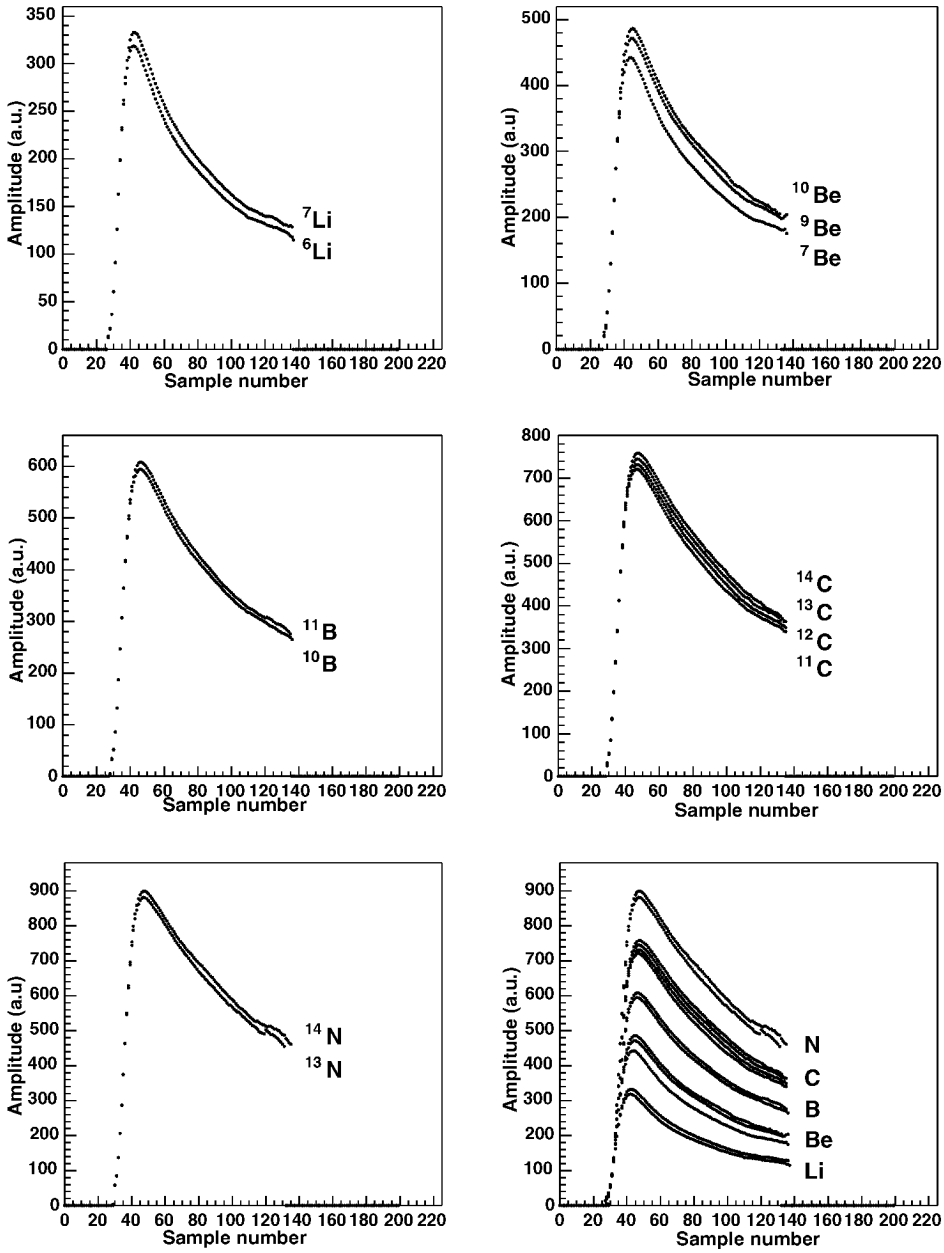

Figure 6.21. The reference shapes of the BCs for Li, Be, B, C and N isotopes obtained with the "single RBC method".

Isotope	Efficiency of identification (%)	
	"raw curves"	"smoothed curves"
^{6}Li	84.9 ± 2.5	84.2 ± 2.4
^{7}Li	82.1 ± 2.1	84.3 ± 1.0
^{7}Be	89.3 ± 1.2	89.5 ± 1.9
^{9}Be	57.0 ± 3.1	35.6 ± 3.4
^{10}Be	68.6 ± 1.6	59.7 ± 2.8
^{10}B	70.3 ± 1.5	71.3 ± 1.6
^{11}B	69.7 ± 2.1	77.5 ± 2.0
^{11}C	63.3 ± 3.0	58.8 ± 2.5
^{12}C	30.2 ± 5.3	36.3 ± 4.4
^{13}C	37.4 ± 4.9	35.0 ± 4.8
^{14}C	59.4 ± 1.4	67.7 ± 2.2
^{13}N	63.7 ± 2.3	63.7 ± 1.8
^{14}N	65.2 ± 1.1	68.4 ± 2.3

Table 6.1. Results of the "multiple RBC method".

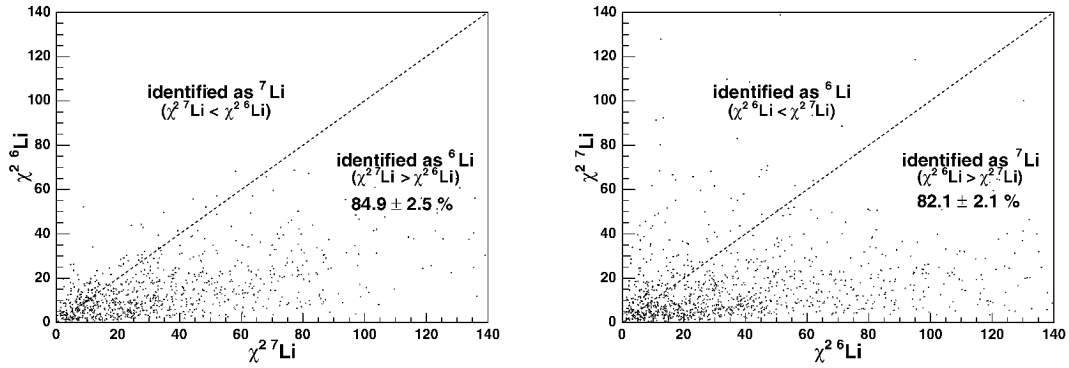

(a) "cross check" for ^{6}Li isotope

(b) "cross check" for ^{7}Li isotope

Figure 6.22. The ^{6}Li and ^{7}Li isotopes "cross checks" by the reference shape χ^2 criterion based on the membership of the identified particle to either ^{6}Li or ^{7}Li isotope.

Ratio of isotopes	Partial test	Total test
^{7}Li/^{6}Li	1.24 ± 0.06	1.04 ± 0.02
^{9}Be/^{7}Be	0.82 ± 0.04	0.43 ± 0.05
^{10}Be/^{9}Be	0.50 ± 0.09	1.30 ± 0.12
^{11}Be/^{10}Be	1.36 ± 0.04	1.12 ± 0.08
^{13}C/^{12}C	0.65 ± 0.02	1.01 ± 0.04
^{14}C/^{13}C	0.33 ± 0.11	0.91 ± 0.09
^{14}N/^{13}N	1.09 ± 0.03	1.07 ± 0.03
^{14}C/^{11}C	0.55 ± 0.05	0.67 ± 0.05
^{10}Be/^{7}Be	0.40 ± 0.04	0.55 ± 0.07

Table 6.2. The partial and total tests results. The shaded rows indicate the isotopes for which the efficiency of identification by the χ^2 criterion in "cross check" method exceeds 60%.

6.2.7 Bragg curve deconvolution method

In order to improve particles identification with the BCD the deconvolution of the BC was performed. The deconvolution method and obtained results are presented in this section.

The convolution is a mathematical way of combining two function to form the third one. The BC signals obtained in the PISA experiment are the convolution of two functions: the original signal (anode current signal) and the preamplifier response signal. The knowledge of the preamplifier response function allows to deconvolute it from the BC signal. For the deconvolution of the preamplifier response signal from the BC signal the Gold method [157], optimized by M.Morháč et al. [158], was used.

The convolution operation of two one-dimensional functions $f(t)$ and $g(t)$, denoted as $f(t) * g(t)$, can be written as the following integral [159–161]:

$$v(t) = f(t) * g(t) = \int_{-\infty}^{+\infty} f(t-x)g(x)dx, \tag{6.2}$$

where $g(t)$ can be treated as an input signal, which goes on indefinitely in time, and $f(t)$ as the response function that falls to zero in both direction from its maximum (e.g. the Gaussian distribution). The formula 6.2 can be also extended on two- or n-dimensional linear systems.

For the discrete signal, where output is sampled at regular intervals the integral in the equation 6.2 becomes sum:

$$v(t) = \sum_{k=0}^{N-1} f(t-x)g(x)dx, \tag{6.3}$$

where N is the total number of intervals. The original signal can be recovered by performing the inverse operation.

The example of the convolution of the rectangular signal (input signal) with the response function (here: Gauss function with $\sigma = 20$) is shown in Fig. 6.23. Since the response function is broader than some features of the original signal, these latter is "washed out" in the convolution. In absence of any additional noise, the process can be reversed by deconvolution.

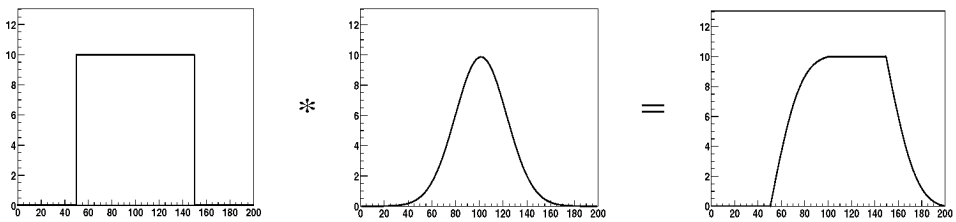

Figure 6.23. The example of the convolution of two functions. The rectangular original signal (input signal) is convoluted with the response function (here: the Gaussian distribution).

In the case of the BC it was assumed that the input signal is convoluted with the standard response function e.g. Gaussian distribution which parameters have been obtained by fitting it to the tail of the BC (see Fig. 6.24(a) on the next page). The parameters of the Gaussian function obtained from various BC (various range and amplitude), are very similar. The example of the deconvolution process performed on arbitrary chosen BC, is shown in Fig. 6.24(b) on the facing page. However, it was found that the Gaussian function only approximately reflects the real response function. Therefore a non-symmetric response function has been considered. In order to study the preamplifier response, rectangular signals of different amplitudes and lengths, in the range of 5–10 μs were fed to the preamplifier input. Selected lengths (5–10 μs) correspond to the lengths of the original BC obtained during the experiment. Typical shapes of the input and obtained convoluted output signals are shown in Fig. 6.25 on the next page.

Taking into account particles identification and identification energy threshold, the identification efficiency with and without deconvolution was compared. No significant differences have been found. Therefore one can conclude that rough approximation of the response function is insufficient to improve the particles identification, and the efforts should be still focused on the searching for the "real" response function.

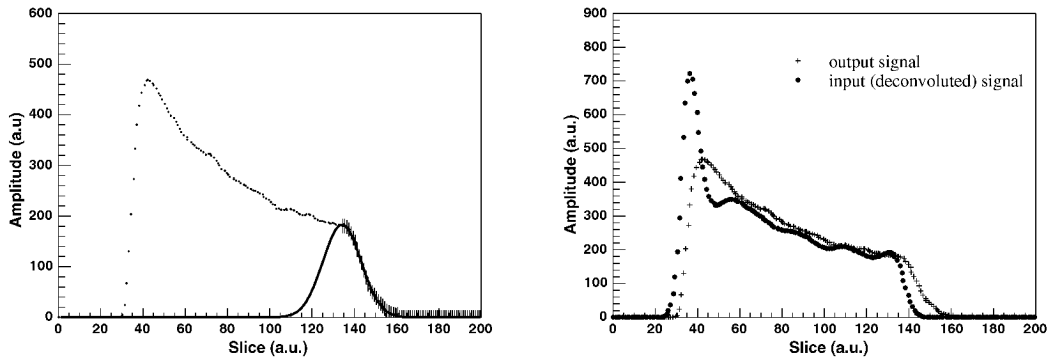

(a) example of the BC with fitted Gaussian function

(b) convoluted and deconvoluted BC

Figure 6.24. (a) The example of the fit of the Gaussian function to the tail of the BC. (b) The shape of the raw and deconvoluted BC. In figure (b) the raw BC is marked by crosses (output signal), whereas the deconvoluted BC by solid circles (input signal). It was assumed that the response signal of the preamplifier is the Gaussian function.

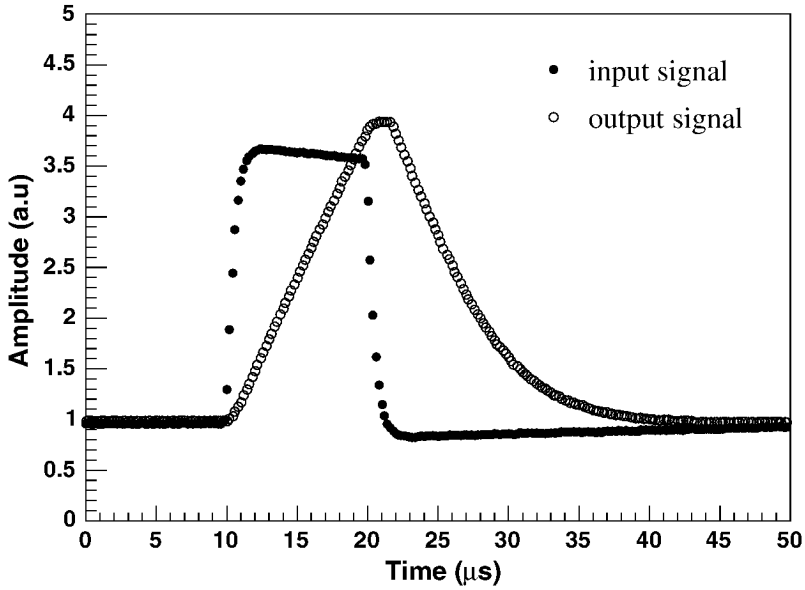

Figure 6.25. The shapes of the input signal fed to the BCD preamplifier (solid circles) and the output signal (open circles).

6.3 Energy spectra of intermediate mass fragments

The energy spectra of fragments emitted from the Ni target irradiated by 1.9 GeV protons at 15° and 120° in the laboratory are shown in Figs. 6.26 to 6.28 on pages 52–54. The fragment energies were corrected for energy losses in the foils in front of the BCDs and entrance windows of the BCDs (cf. section B.1 on page 73). The low energy cutoff (~ 1 MeV/A) arises from the detectors thresholds (~ 0.5 MeV/A; cf. section 6.2.6.1 on page 39) and the energy losses in the foils prior the BCD. As expected, the low energy cutoff threshold value increases with charge. It is very well visible in Fig. 6.26. The identification of isotopes was performed by means of the BC spectroscopy combined with the time-of-flight method. The correction for the MCPs efficiency, as a function of mass and energy, was taken into account (cf. section 6.1 on page 33).

One can notice, that the high energetic isotopes of C and N elements measured at forward direction (15°), are more abundant than those obtained at backward direction (120°).

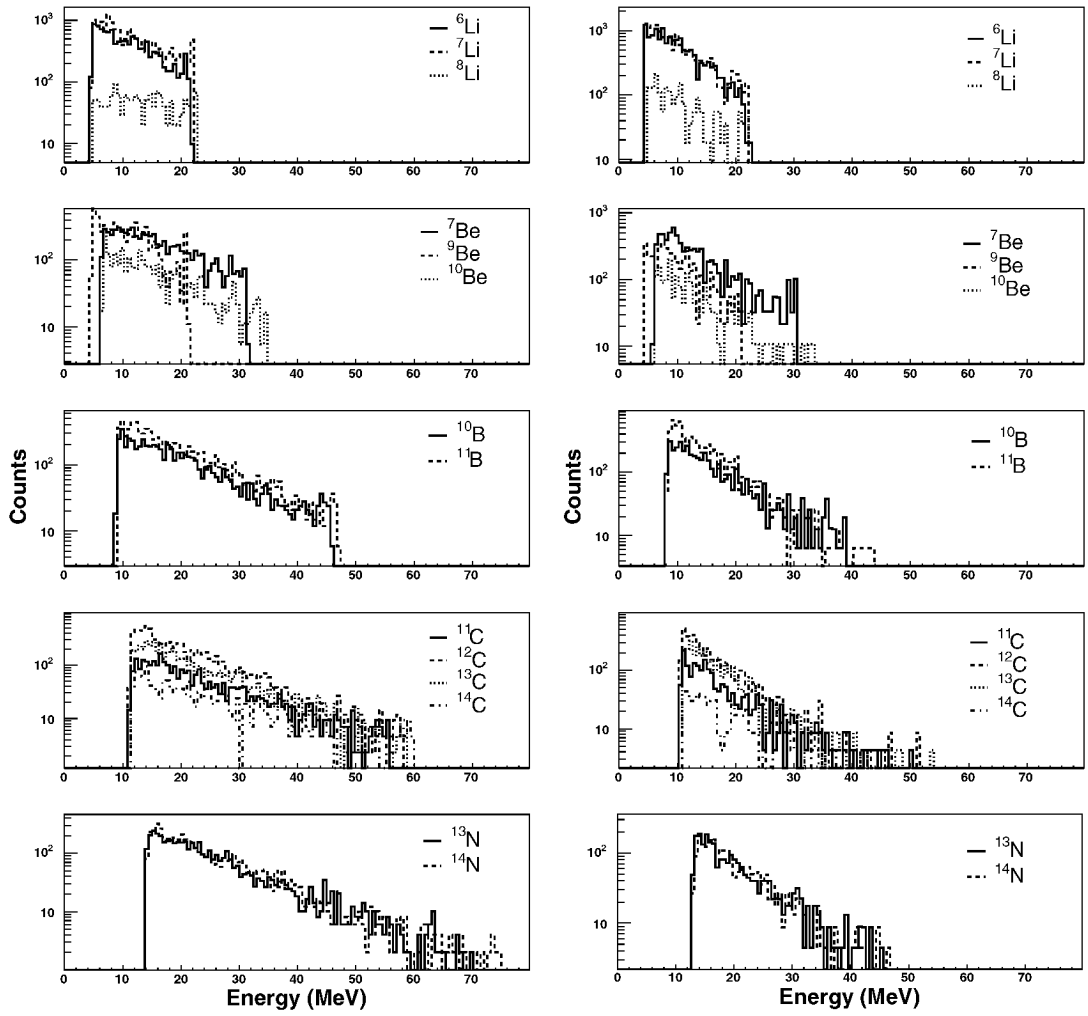

(a) isotopes from p(1.9 GeV) + ^{nat}Ni at 15°

(b) isotopes from p(1.9 GeV) + ^{nat}Ni at 120°

Figure 6.26. Energy spectra of various isotopes from p(1.9 GeV) + ^{nat}Ni reaction measured at 15° and 120°.

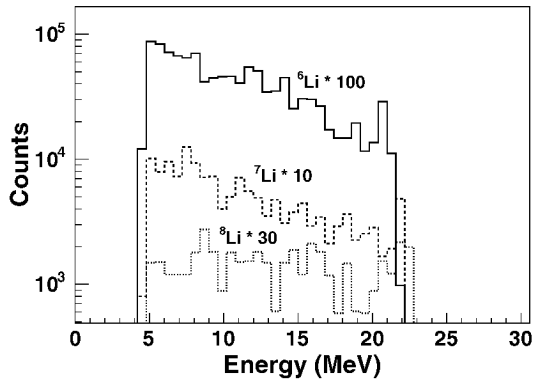

(a) ^{6,7,8}Li from p(1.9 GeV) + ^{nat}Ni at 15°

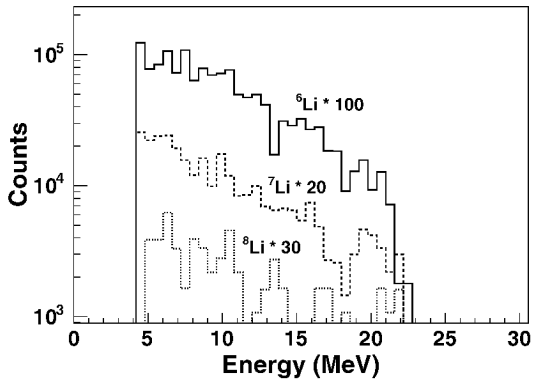

(b) ^{6,7,8}Li from p(1.9 GeV) + ^{nat}Ni at 120°

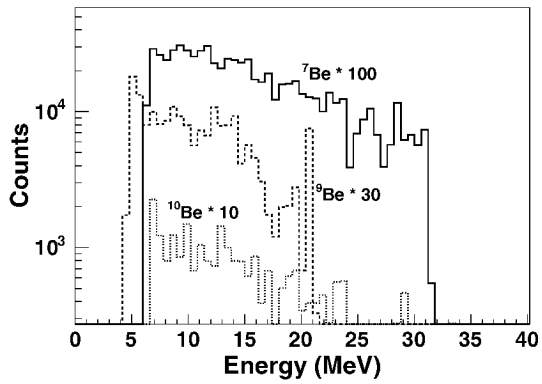

(c) ^{7,9,10}Be from p(1.9 GeV) + ^{nat}Ni at 15°

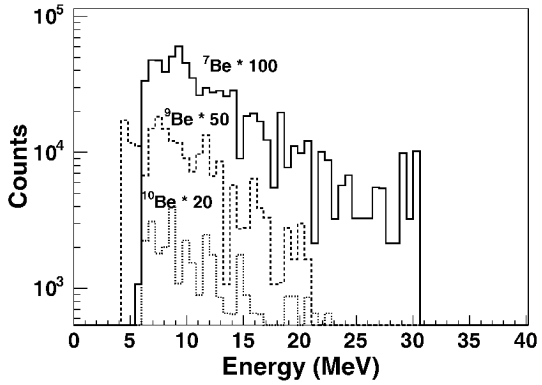

(d) ^{7,9,10}Be from p(1.9 GeV) + ^{nat}Ni at 120°

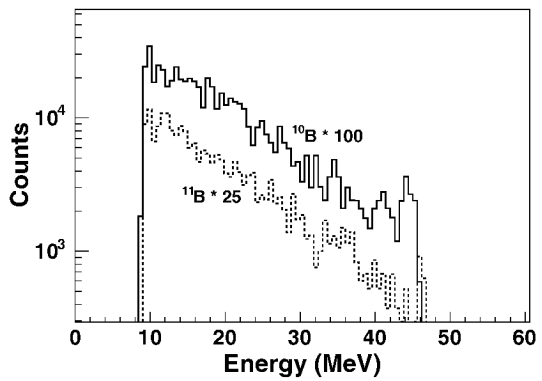

(e) ^{10,11}B from p(1.9 GeV) + ^{nat}Ni at 15°

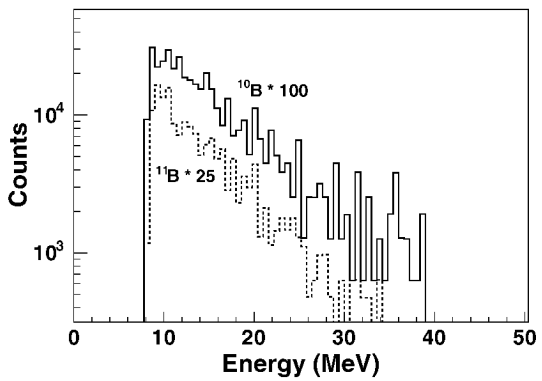

(f) ^{10,11}B from p(1.9 GeV) + ^{nat}Ni at 120°

Figure 6.27. Energy spectra of ^{6}Li, ^{7}Li, ^{8}Li, ^{7}Be, ^{9}Be, ^{10}Be, ^{10}B and ^{11}B isotopes from the p(1.9 GeV) + ^{nat}Ni reaction measured at 15° and 120°.

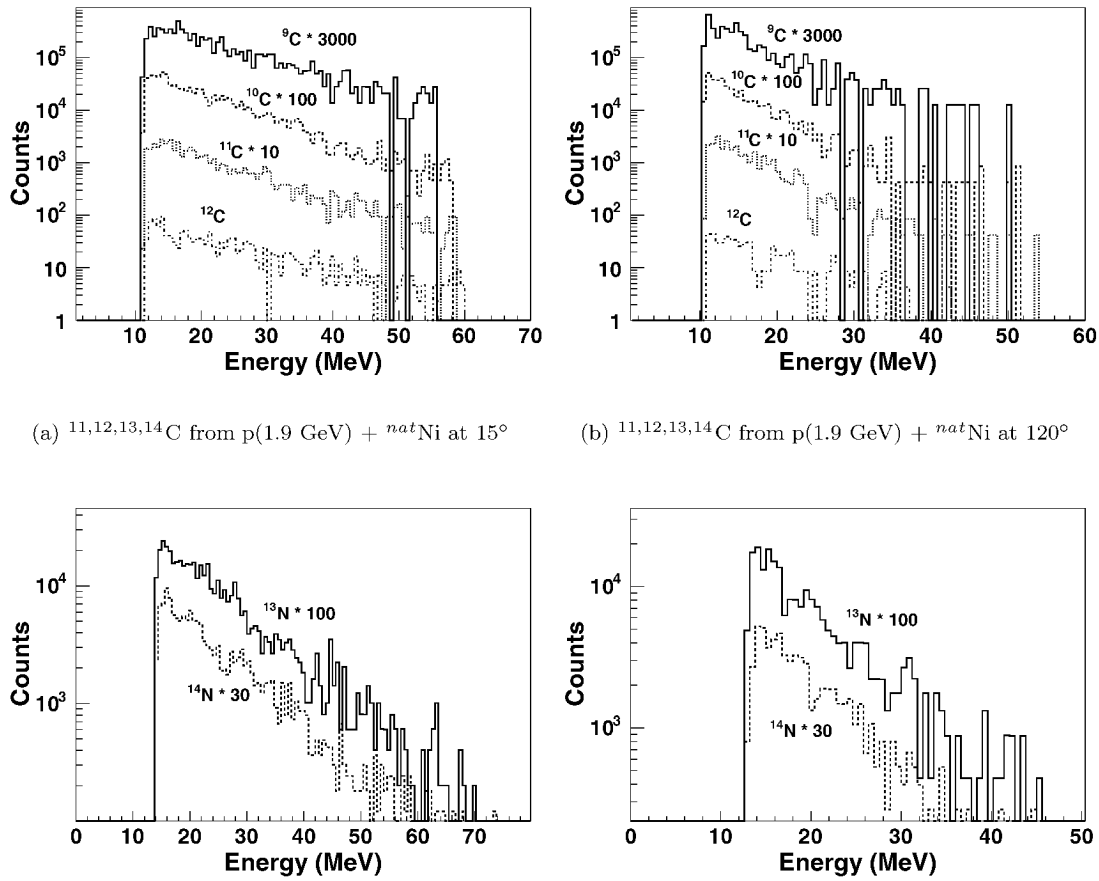

(a) ^{11,12,13,14}C from p(1.9 GeV) + ^{nat}Ni at 15°

(b) ^{11,12,13,14}C from p(1.9 GeV) + ^{nat}Ni at 120°

(c) ^{13,14}N from p(1.9 GeV) + ^{nat}Ni at 15°

(d) ^{13,14}N from p(1.9 GeV) + ^{nat}Ni at 120°

Figure 6.28. Energy spectra of ^{11}C, ^{12}C, ^{13}C, ^{14}C, ^{13}N and ^{14}N isotopes from the p(1.9 GeV) + ^{nat}Ni reaction measured at 15° and 120°.

6.4 Nuclear temperature determination

The determination of the nuclear matter temperature of the system created in the p(1.9 GeV) + ^{nat}Ni reaction is presented in this section. The results were obtained by applying two methods: (i) the double isotope yield ratio of emitted particles, and (ii) the slope parameter from the fragments kinetic energy spectra. The description of both methods is given in section 2.3 on page 9. The so called "apparent" temperature is determined, because contributions from the sequential decays (double isotope ratio method) and non-equilibrated particles emission (slope parameter method) can not be measured with the PISA experimental setup.

6.4.1 Temperature from fragments kinetic energy spectra of reaction products

The nuclear thermometer which has been under intense studies in the past few years [4, 52, 53, 58] utilizes the slope of the particle kinetic energy spectra. This thermometer is traditionally used at lower energies [27, 162–164] of the incident particles, because at higher energies the dynamical effects disturb the information which is included in it.

Z	A	T_{app}	
		15°	120°
3	6	7.3 ± 1.6	4.3 ± 0.1
3	7	8.5 ± 0.1	4.6 ± 0.3
4	7	7.1 ± 0.2	4.2 ± 0.1
4	9	4.5 ± 0.1	4.8 ± 0.5
4	10	9.9 ± 0.2	10.3 ± 0.2
5	10	7.6 ± 0.2	4.7 ± 0.2
5	11	7.4 ± 0.2	4.6 ± 0.5
6	11	10.0 ± 1.2	6.9 ± 1.6
6	12	6.6 ± 0.3	4.9 ± 0.1
6	13	6.3 ± 0.2	3.9 ± 0.2
6	14	14.9 ± 0.3	10.4 ± 0.4
7	13	7.5 ± 0.3	4.2 ± 0.3
7	14	7.2 ± 0.2	6.3 ± 0.1

Table 6.3. The temperatures extracted from the fit of the Maxwell distributions to the energy spectra of emitted fragments from the p(1.9 GeV) + ^{nat}Ni reaction detected at 15° and 120°.

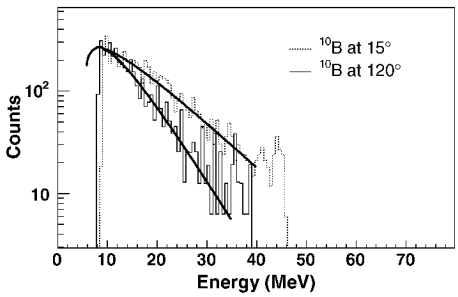

(a) ^{10}B from the p(1.9 GeV) + ^{nat}Ni at 15° and 120°

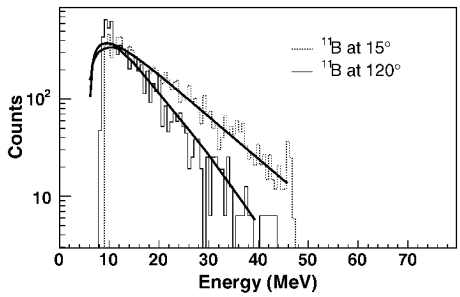

(b) ^{11}B from the p(1.9 GeV) + ^{nat}Ni at 15° and 120°

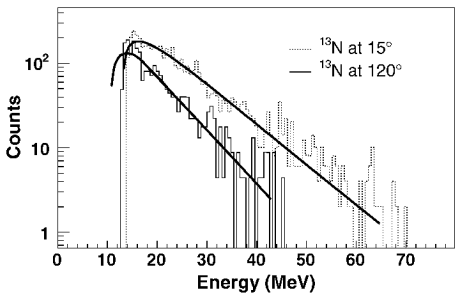

(c) ^{13}N from the p(1.9 GeV) + ^{nat}Ni at 15° and 120°

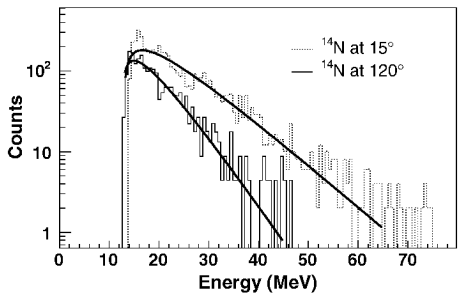

(d) ^{14}N from the p(1.9 GeV) + ^{nat}Ni at 15° and 120°

Figure 6.29. Energy spectra of ^{10}B, ^{11}B, ^{13}N and ^{14}N isotopes from the p(1.9 GeV) + ^{nat}Ni reaction observed at 15° and 120°. The isotopes identification were done by means of the BCD spectroscopy combined with the time-of-flight method. The spectra are corrected for the MCPDs efficiency. The solid lines are fits to the spectra using Eq. 2.2 on page 10.

It has been observed in Figs. 6.26 to 6.28 on pages 52–54 and Fig. 6.29 on the page before that the slope of the energy spectra at 120° is steeper than at 15°. This indicates that the temperature extracted from the slope of the energy spectra decreases as the detection angle increases. This observation is in agreement with the following assumption about the reaction mechanism: relatively higher temperature is associated with the non-equilibrated particles emission, and therefore related to the particles emission at forward angles.

The fragment energy distributions have been fitted using the Maxwellian function (see Eq. 2.2 on page 10). As a fit result T_{app} was obtained, and is presented in Tab 6.3 on the page before. Examples of the energy spectra of ^{10}B, ^{11}B, ^{13}N and ^{14}N isotopes and Maxwellian fits are shown in Fig. 6.29 on the preceding page. As it was expected, obtained temperature values are larger for the forward angle than for the backward one.

6.4.2 Temperature from double ratio of isotope yields

The temperature was evaluated from the double isotopic yield ratio of particles emitted at 15°, 35° and 120° in the p(1.9 GeV) + ^{nat}Ni reaction. For the particles measured by means of the BCDs (at 15° and 120°) the efficiency of the MCPDs has been taken into account (cf. section 6.1 on page 33). The isotope yields at 15° and 120° were obtained by integration of the energy spectra of isotopes, using the Maxwellian distribution in order to correct the data for not measured low energy part of the spectra. The temperatures from the isotopic yield ratios of emitted particles at 15° and 35° were determined only for tests, since the applicability of the Eqs. 2.4 to 2.7 on page 11 is restricted only to the equilibrated systems. It was assumed that at forward angles (15° and 35°) the particles emitted from the first, fast non-equilibrium part of the reaction, are more abundant. This assumption supports larger value of the power law parameter τ at 120° than at 15° (see Fig. 6.35 on page 61).

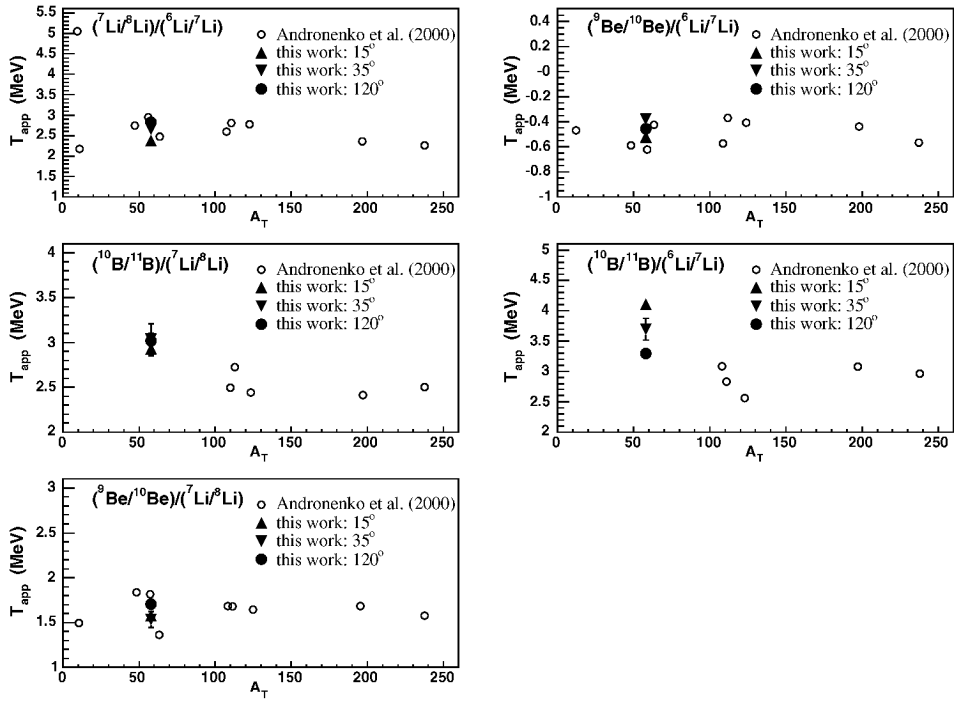

Figure 6.30. Apparent temperature as a function of the target mass A_T. Temperatures were obtained from the double isotopic yield ratio of emitted particles from the p(1.9 GeV) + ^{nat}Ni reaction at 15°, 35° and 120°. Solid triangles and circles are derived from ratios of (^{9}Be/^{10}Be)/(^{6}Li/^{7}Li), (^{9}Be/^{10}Be)/(^{7}Li/^{8}Li), (^{7}Li/^{8}Li)/(^{6}Li/^{7}Li), (^{10}B/^{11}B)/(^{6}Li/^{7}Li) and (^{10}B/^{11}B)/(^{7}Li/^{8}Li). The open circle represent data from Ref. [165]. No corrections have been made for sequential decay effects.

In order to minimize the influence of the Coulomb barrier, the isotopes with $\Delta A = 1$ and $\Delta Z = 0$ were chosen. The influence of the Coulomb barrier is mass dependent, whereas the thermal energies do not depend on the mass of the fragment [166–168].

The values of apparent temperatures (T_{app}) obtained from 47 double isotopes pairs, measured at 15°, 35° and 120° are presented in Tab. 6.4. Additionally, in Fig. 6.30 on the preceding page, the temperature from the double Li–Li, Li–Be and Li–B isotopic ratios as a function of the mass of the target (A_T) is compared with T_{app} obtained by Andronenko et al. [165]. In Ref. [165] the nuclear temperatures were extracted from the double isotope yield ratio measured in the p(1GeV) + A reaction, where A correspond to ^{6}Li, ^{7}Li, Be, C, Al, ^{58}Ni, Ag, Au, ^{238}U and Pb.

It can be observed that obtained values of the temperatures fluctuate over a large range of T_{app}, including the negative numbers. This results the fact that the reaction fragments can be highly excited and the sequential decays can lead to the non-negligible corrections to the measured isotope ratio [103]. The simple theoretical model (Eq. 2.4 on page 11) neglects these corrections. These fluctuations of the isotope ratio, and thus sensitivity of the temperature to such corrections can be minimized by selecting double ratios of isotopes with large binding energy differences (B). The uncertainties in T_{app} are proportional to the ratio T_{app}/B [28, 103]. Thus it can be concluded that nuclear matter thermometers characterized by the value of $B \gg T_{app}$ ($B \gtrsim$ 6–8) are more reliable. The temperatures obtained from the double isotope ratios as a function of B parameter are shown in Fig. 6.31 on the next page. One can observe that T_{app} is around 4 MeV for $B > 5$.

Combination of isotope pairs	T_{app} (MeV)			a	B (MeV)
	15°	35°	120°		
(^{7}Li/^{8}Li)/(^{6}Li/^{7}Li)	2.4 ± 0.3	2.7 ± 0.3	2.8 ± 0.3	0.90	5.22
(^{9}Be/^{10}Be)/(^{6}Li/^{7}Li)	-0.5 ± 0.3	1.6 ± 0.3	-0.4 ± 0.3	0.39	-4.2
(^{10}B/^{11}B)/(^{7}Li/^{8}Li)	2.9 ± 0.3	3.1 ± 0.5	3.0 ± 0.3	0.17	0.44
(^{9}Be/^{10}Be)/(^{7}Li/^{8}Li)	1.6 ± 0.3	-0.4 ± 0.3	1.7 ± 0.3	0.19	-4.78
(^{10}Be/^{11}Be)/(^{6}Li/^{7}Li)	4.1 ± 0.3	3.7 ± 0.4	3.3 ± 0.3	0.43	-9.42
(^{13}C/^{14}C)/(^{11}C/^{12}C)	3.1 ± 0.3		3.4 ± 0.5	1.96	10.54
(^{6}Li/^{7}Li)/(^{11}C/^{12}C)	4.6 ± 0.3		4.1 ± 0.3	5.90	11.47
(^{9}Be/^{10}Be)/(^{11}C/^{12}C)	7.2 ± 0.5		6.6 ± 0.5	1.03	11.91
(^{12}C/^{13}C)/(^{11}C/^{12}C)	4.0 ± 0.3		3.9 ± 0.3	7.93	13.77
(^{7}Li/^{8}Li)/(^{11}C/^{12}C)	3.6 ± 0.3		3.6 ± 0.3	5.37	16.69
(^{6}Li/^{7}Li)/(^{12}C/^{13}C)	2.5 ± 0.3		3.1 ± 0.3	0.74	-2.30
(^{6}Li/^{7}Li)/(^{13}C/^{14}C)	-4.2 ± 0.3		-2.9 ± 0.3	3.01	0.93
(^{7}Li/^{8}Li)/(^{12}C/^{13}C)	2.3 ± 0.3		2.7 ± 0.3	0.68	2.91
(^{7}Li/^{8}Li)/(^{13}C/^{14}C)	3.1 ± 0.3		4.0 ± 0.5	2.73	6.14
(^{9}Be/^{10}Be)/(^{12}C/^{13}C)	1.0 ± 0.3		1.1 ± 0.3	0.13	-1.87
(^{9}Be/^{10}Be)/(^{13}C/^{14}C)	-1.3 ± 0.3		-1.1 ± 0.3	0.52	1.36
(^{10}B/^{11}B)/(^{11}C/^{12}C)	5.0 ± 0.3		4.9 ± 0.4	2.32	7.27
(^{10}B/^{11}B)/(^{12}C/^{13}C)	3.3 ± 0.3		3.2 ± 0.3	0.29	-6.51
(^{10}B/^{11}B)/(^{13}C/^{14}C)	2.6 ± 0.3		2.1 ± 0.3	1.18	-3.28
(^{6}Li/^{7}Li)/(^{13}N/^{14}N)	-2.5 ± 0.8			1.00	3.30
(^{7}Li/^{8}Li)/(^{13}N/^{14}N)	4.1 ± 0.3			0.91	8.52
(^{9}Be/^{10}Be)/(^{13}N/^{14}N)	-3.8 ± 0.3			0.17	3.74
(^{10}B/^{11}B)/(^{13}N/^{14}N)	2.9 ± 0.3			0.39	-0.90

Table 6.4. Values of apparent temperatures obtained from the double yield isotope ratio of emitted particles at 15°, 35° and 120°. Values of constant a (cf. Eg. 2.5 on page 11) and B (cf. Eq. 2.6 on page 11) for various combinations of double isotope pairs are also given. No corrections have been made for the sequential decay effects.

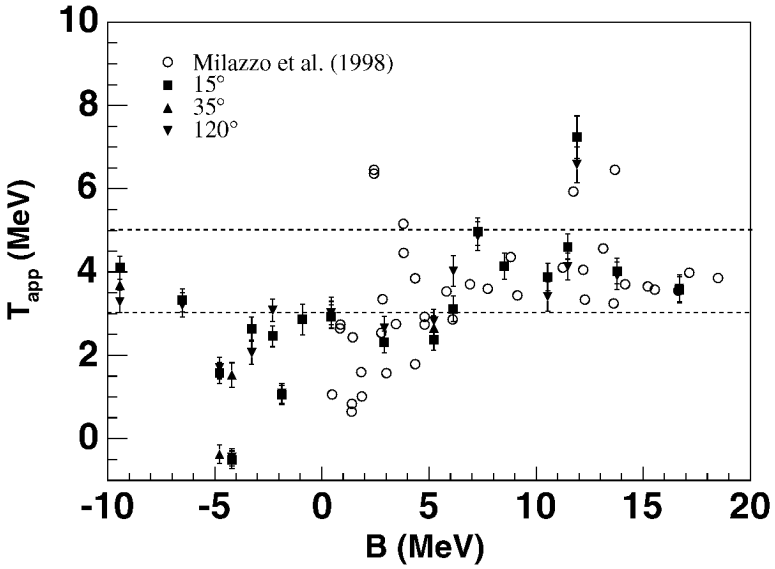

Figure 6.31. Apparent temperature as a function of the binding energy difference parameter for the p(1.9 GeV) + ^{nat}Ni system (cf. Tab. 6.4 on the page before). The solid triangles, squares and reverse triangles are from this work, whereas open circles from Ref. [103]. The straight dashed lines are drawn to guide the eye only.

6.4.3 Comparison between thermometers

The temperatures determined with two presented methods (the double isotope yield ratio and the method based on the slope of the fragment kinetic energy spectra) differ. This difference may be caused by the restricted applicability of both methods, which can be summarized in the following:

- As was suggested in Refs. [28, 103], and what can be observed in Fig. 6.31 the double isotope ratio thermometers characterized by value of $B \gg T_{app}$ ($B \gtrsim$ 6–8) are more reliable (the uncertainties in T_{app} are proportional to the ratio T_{app}/B [28, 103]) for the measurement of the nuclear temperature of the equilibrated system.

- The temperature values obtained at 15° are larger than those obtained at 120°. It can be explained by the fact that the spectra at forward angles are strongly influenced by products from the fast pre-equilibrium intranuclear cascade, therefore are derived from the non-equilibrated system. The kinetic energy spectra of fragments obtained at backward angles (e.g. 120°) give the more reliable information about the temperature of the equilibrated system.

The temperatures obtained from both methods are plotted in Fig. 6.32 on the next page for the different isotopes and isotope pairs. For the method based on the slope of the fragment kinetic energy spectra only the temperatures obtained from the spectra measured at backward angle (120°) are plotted. For the double isotope ratio method only 7 points, corresponding to the largest values of B (see Tab. 6.4 on the preceding page), are plotted.

One can notice that obtained values of temperatures of equilibrated source oscillate around 4.8 MeV. The average values of temperatures obtained from the straight line fit to the various sets of data are following: 5.1 $\pm$ 0.1 (fit to T_{app} values from the slope of the kinetic energy spectra only), 4.2 $\pm$ 0.1 (fit to T_{app} values from the double isotope ratio method for 7 biggest values of B), 4.8 $\pm$ 0.1 (fit to T_{app} values from both methods).

6.6 Power law parameter τ - mass and charge distributions of reaction products

In early studies of proton-induced reactions [1, 6] it was found that the yield distribution of mass fragments (A_f) obeys a power law behavior:

$$yield(A_f) \sim {A_f}^{-\tau}, \tag{6.4}$$

where τ is the power law parameter, which has to be determined from the experimental data. The same rule can be applied to the fragment charge distribution:

$$yield(Z_f) \sim {Z_f}^{-\tau}. \tag{6.5}$$

The power law parameter τ was originally used as an evidence and test of the critical point in the nuclear liquid-gas phase transition in high energy proton induced reactions [6, 19, 180]. It also may reflect change in the reaction mechanism, as suggested in Refs. [4, 53].

The number of intermediate mass fragments (IMFs) produced in the p(1.9 GeV) + ^{nat}Ni reaction, and stopped in the BCDs are presented in Fig. 6.35 for 15° and 120° as a function fragments' charge (Z). The count values were obtained by integration of the energy spectra of IMFs, using the Maxwellian distribution in order to correct the data for not measured low energy particles. The values of τ were determined by fitting the Eq. 6.5 to the integrated spectra.

The values of τ parameter (in range of $3 \leqslant Z \leqslant 7$) are 3.2 ± 0.1 and 3.7 ± 0.1 at 15° and 120°, respectively. According to the Ref. [52] the relatively larger values of the τ are associated with equilibrium processes, whereas non-equilibrium processes are described by lower values of τ. Therefore it can be concluded that for one selected projectile energy, the charge distribution at forward angles reflects the non-equilibrium processes, whereas the emission of fragments at backward angles is dominated by the equilibrium processes.

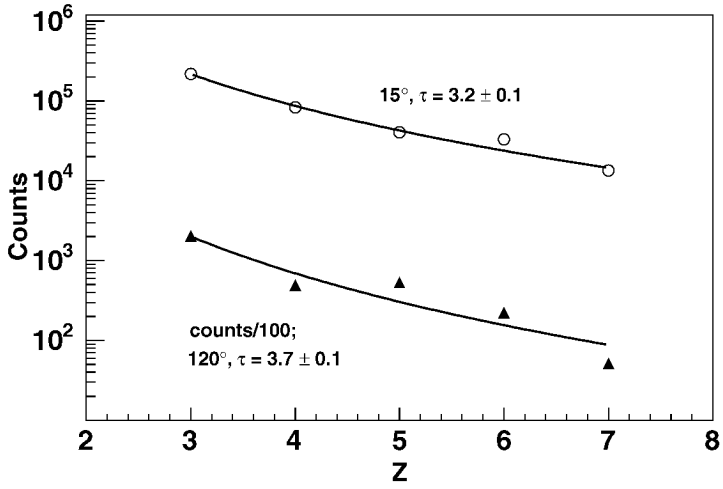

Figure 6.35. The counts of the IMFs versus fragments' charge (Z) from the BCD at 15° and 120°. The solid lines are power law fits (Eq. 6.5). The solid angle ratio of the BCDs at 15° and 120° was taken into account.

In previous sections it was shown that the nuclear matter temperature (T) varies with the angle of detected fragments, therefore it was concluded that T may reflect the change in the mechanism of the fragments production. Thus, the power law parameter τ should also vary with the temperature. In Fig. 6.36 on the next page the power law parameter, as a function of the temperature, is shown. Two temperatures were obtained from the slopes of the kinetic

energy spectra at 15° and 120°. They represent the average apparent temperature (T_{app}). As it is expected the τ parameter strongly depends on the temperature. The τ decreases with the temperature up to about 11–12 MeV, than the trend is reversed. In the Ref. [19] it was concluded that such behavior of the τ and T may indicate the critical temperature T_c of the liquid-gas phase transition. According to Ref. [85] the critical temperature of the finite nuclear system is in the range of 9–13 MeV.

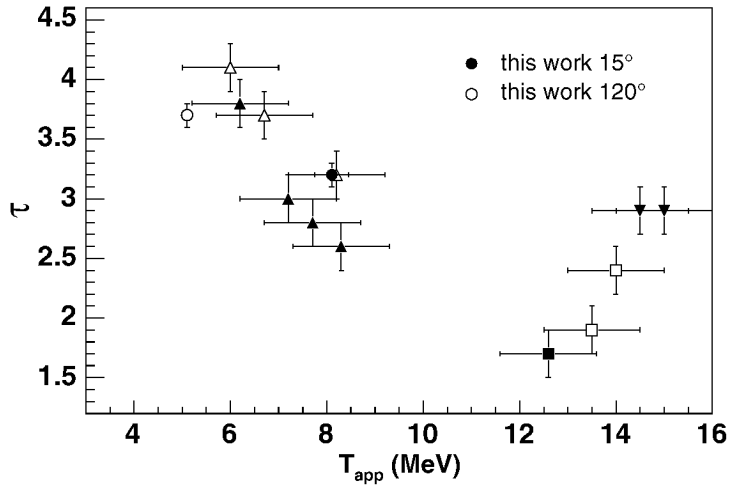

Figure 6.36. The power law parameter τ as a function of the apparent temperature (T_{app}). The symbols correspond as follow: solid, empty circles - this work; empty triangles - Ref. [4]; empty squares - Ref. [54]; solid reverse triangles - Ref. [6]; solid square - Ref. [1]; solid triangles - Ref. [181]. Fig. adapted from Ref. [19]

Chapter 7

Summary and conclusions

Omnia iam fient fieri quae posse negabam

Publius Ovidius Naso (43 B.C.–A.D. 18)

In this thesis the first results of the PISA project (**P**roton **I**nduced **S**p**A**llation) are discussed. The project consists in measuring of the intermediate mass fragments (IMFs) from proton induced reaction on nuclei using the internal proton beam of the COSY ring of the Forschungszentrum Jülich. The emphasis is put on the elemental and isotopic identification of the fragments and measuring the double differential production cross section. Efficient application of a new detecting system, consisted of Bragg curve detectors combined with the time-of-flight technique needed solution of a few experimental problems. The present thesis was devoted to solution of these problems and to application of the PISA apparatus for investigation of the reaction involved by protons of energy of 1.9 GeV interacting with the ^{nat}Ni nuclei.

The main tasks of the present PhD thesis were: (i) to built an appropriate data acquisition system, (ii) to perform the experiment on the internal beam of the COSY accelerator, (iii) to propose the methodology of the off-line analysis of the data from the Bragg curve detector (BCD) and microchannelplates (MCPD), (iv) to apply it to the event-by-event stored data, and (v) to perform the analysis of the extracted data.

In the course of the off-line analysis of the data from the BCD the emphasis was put on the identification of the particles in the wide range of their charge and mass, with the lowest possible energy detection threshold. The IMFs in the charge range $3 \leqslant Z \leqslant 14$ and $3 \leqslant Z \leqslant 11$, emitted in the p(1.9 GeV) + ^{nat}Ni reaction, were observed at 15° and 120° with the respect to the beam direction, respectively. The fragment charge and mass identification has been performed by means of the Bragg curve detectors and time-of-flight technique (TOF) using set of the microchannelplate detectors.

The use of the BCDs, which are gas ionization chambers, enabled for the particle identification down to very low energy threshold of about 0.5 MeV/A, common for all detected Z. After taking into account the energy losses in foils placed in the front of the BCD (cf. section 3.2 on page 15), the energy threshold increases to about 1 MeV/A. It still allows to explore the kinetic energy spectra of ejectiles well below the Coulomb barriers. The application of the Flash ADC module [117] for recording the Bragg detector signal allowed to reproduce precisely the shape of the Bragg curve (BC). Therefore the advantages offered by the Bragg curve spectroscopy result in excellent identification of charged fragments.

By the appropriate selection of the gas and electric field conditions for the BCDs, by applying a Flash ADC module [117], and finally by the use of a specially designed current preamplifier [115, 116] for the Bragg signal amplification, the excellent charge resolution of measured fragments was achieved: 10–12% per charge unit for peaks where isotopes are not distinguished, and 14% for beryllium where the isotopical structure is visible (cf. section 6.2.6.1 on page 39).

The obtained results give the hope that further development of the mass and charge identi-

fication from the Bragg curve (e.g. reference shape or/and pulse shape discrimination methods; cf. section 6.2.6.3 on page 46), may allow to improve not only the charge but also the mass identification of the fragments. We believe that the deconvolution of the BCD signal, may help to obtain more reliable shape of the Bragg curve, and can allow to distinguish isotopes of heavier elements. At the same time, the work on the improvement of the current preamplifier plugged into the BCD should be continued.

By combining the BCD and TOF, the distinct separation of following isotopes was achieved: ^{6}Li, ^{7}Li, ^{8}Li, ^{7}Be, ^{9}Be, ^{10}Be, ^{10}B, ^{11}B, ^{11}C, ^{12}C, ^{13}C, ^{14}C, ^{13}N and ^{14}N.

The energy spectra of the IMFs obtained by means of the BCD and TOF proved that such set of detectors is very useful for the IMFs identification. The obtained fragments energy distributions and values of the isotope yields measured at 15° and 120° were used for the determination of the temperature of the disassembling system created in the p(1.9 GeV) + ^{nat}Ni reaction. The following two methods for the nuclear matter temperature determination have been used: method based on the double isotopic yield ratio of emitted particles [27,28,59–62], and method which explores the shapes of the energy spectra of nuclear collision remnants [4,52,53,58]. In the first method the isotope yields were obtained by the integration of the isotope energy spectra, using the Maxwellian distributions, in order to correct the data for the unmeasured low energy part of the spectra.

The obtained values of the nuclear matter temperature T from both methods are consistent and oscillate around 4–5 MeV, what is in agreement with the temperature values of the equilibrated nuclear matter reported in the literature [7,61,104,165,182]. It can be also noticed that the average temperature evaluated from the slope of kinetic energy spectra is larger than T obtained from the double isotope ratio method. It can be explained by the contribution to the kinetic energy spectra of the fragments emitted from a non-equilibrated source.

The determination of the nuclear matter temperature was possible from 47 double ratios of isotope yields (i.e. using 47 "thermometers"). However, accordingly to the Refs. [28,103], only thermometers involving proton-rich isotopes, as e.g. ^{11}C (i.e. those which fulfill the condition of B (binding energy differences) $\gtrsim$ 6–8 MeV), give the most reliable information about the nuclear temperature of an equilibrated system (cf. section 6.4.2 on page 56). Among 47 constructed "thermometers" only 7 (at 120°) fulfill this condition. In the calculations performed in the framework of this thesis, the temperature values were corrected neither for the sequential decay, nor for the isotope contribution from the non-equilibrium emission. These two effects may slightly change the nuclear matter temperature, as was shown in Ref. [28].

The differences between temperatures evaluated from the fragments kinetic energy spectra obtained for each identified fragment at forward (15°) and backward (120°) angles, as well as different values of the power law parameter (τ) suggest the following mechanism of the IMF production: (i) during the first, fast stage of the reaction energetic particles (mainly light) are emitted in the direction strongly correlated with the beam direction (i.e. forward), whereas (ii) during the second, slow stage of the reaction the equilibrated nucleus evaporates isotropically low energy fragments. Therefore, the obtained temperatures of nuclear matter (temperature slope parameters) are larger at 15° than those obtained at 120°. The analysis of various particle spectra at backward angle (120°) shows approximately the same initial temperature of the emitting source, what may serve as an evidence of the statistical equilibrium in the hot nucleus.

The copious emission of the intermediate mass fragments is one of the predicted consequences of the liquid-gas phase transition (PT) in the nuclear matter [10,19,57,183]. One of the methods of the investigation of the PT phenomenon relies on the creation of the excitation energy-temperature diagram, the so called caloric curve (CC). The temperatures obtained within this thesis allowed to enrich the existing CC by adding the unmeasured previously temperature of the equilibrated nucleus created in the p(1.9 GeV) + ^{nat}Ni reaction. It should be noticed that the CC based only on the temperature and the excitation energy of the system is reliable only under several conditions, e.g the pressure is constant [184]. However, there is no experimental evidence that such condition is met in the investigated nuclear collisions. An attempt to construct the nuclear CC based on the pressure, volume and temperature of the nuclear matter was

recently undertaken, as mentioned in Ref. [183].

The low-energy spectra of intermediate mass fragments detected in the PISA experiment are well understood in terms of the particles evaporation from the hot nuclear target remnants after the intranuclear cascade (INC). In order to cover the high-energy part of the fragments spectra, which are expected to be filled by the products from the fast stage of the reaction, it is planned in the forthcoming experiment to detect the particles by the silicon and phoswich detectors mounted behind the BCD. The PISA experimental setup described in the section 3 on page 13 contains already detectors behind the BCD, however due to the technical problems during the last experiment the data from these detectors were not available.

It is also important to increase the efficiency of the microchannelplate detectors, e.g by using a foil, different than carbon, from which the δ electrons are knocked out (cf. section 3.2.2 on page 17). The results of the recently performed studies of the MCPD efficiency, with the mylar foil with very thin layer of Al on the surface, are very encouraging [185].

The data acquisition software package specially designed and written for the PISA experiment, although efficient and appropriate to the needs, has not avoided bugs and operational imperfection. The experiment is not a static system, but can be treated as a still growing organism, with growing needs. Therefore the continuous work on the software is required. It is especially important to work on the improvement of the efficiency and speed of the read out procedures implemented into the PISA software package. This is not meaningless in the case of the planned extension of the PISA experimental setup for the additional Bragg curve detectors, mounted at 20°, 35°, 50°, 65°, 80° and 100° with the respect to the beam direction. The part of the PISA software responsible for the data processing (cf. section 4.2.1 on page 25) was mainly engaged (in 90%) with the data collected by the BCDs. The extension of the PISA software package should be relatively easy due to its modular structure.

It is expected that the results obtained by the PISA collaboration during the first run in 2002 and presented partly in this thesis, together with the forthcoming production cross section measurements in the next runs will enrich our knowledge of the reaction mechanisms, and supplement the existing nuclear data basis.

Appendix B

Simulation of the PISA experiment

The simulation of the PISA experiment was performed with the use of the Geant4 [63], and partially Srim-2003 code [64, 65]. In the simulation with the Geant4 package the geometry of the experimental setup, composition and thicknesses of all parts of the detection system were taken into account (cf. chapter 3 on page 13).

The Geant4 simulation of the PISA experiment has been done from scratch, in the framework of the present PhD thesis. Details of the simulation related to the previous parts of this thesis are presented in this section.

B.1 Energy deposited in BCD volume as a function of particle incident energy

Simulation of the IMFs ($2 \leqslant Z \leqslant 7$) energy deposition in the BCD volume as a function of the IMFs incident energy is shown in Fig. B.1. The falling part of the curves correspond to the particles which cross the BCD.

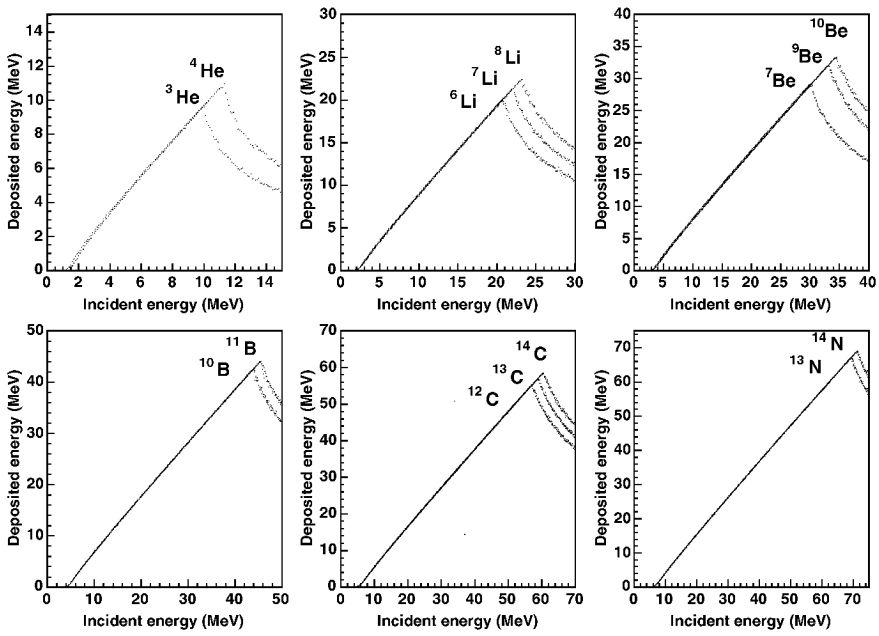

Figure B.1. Simulated energy deposition inside the BCD versus incident energy of intermediate mass fragments with $2 \leqslant Z \leqslant 7$.

The particle, before the BCD, crosses following foils: (i) 2 thin carbon foils (15-20 μg/cm^2), (ii) Mylar foil (1.12 μm) and, (iii) one side metalized Mylar foil (3.5 μm).

B.2 Range of intermediate mass fragments in the ^{nat}Ni target

In order to obtain undistorted information about the reaction mechanism it was decided to use in the PISA experiment the targets with thicknesses smaller than 200 μg/cm^2. Such thicknesses of targets allows reaction products to escape the target with minimal energy loss and minimal distortion due to scattering inside the target.

It was found that the particles up to the Si element, with energy above 300 keV, have a range greater than thickness of the ^{nat}Ni target used in the PISA experiment (thickness equal to 150 μg/cm^2). For the target with thickness of 300 $\mu g/cm^2$ (two times the thickness of the PISA target), the energy threshold of particles which can escape from it increases to 600 keV. Therefore, it can be concluded that this energy value is still below the BCD detection threshold, which is about 0.5 MeV/A.

Simulated range of the IMFs ($6 \leqslant A \leqslant 28$) in the ^{nat}Ni target as a function of incident IMFs energy are shown in Fig. B.2. The simulation was performed with use of the Srim-2003 code [64, 65].

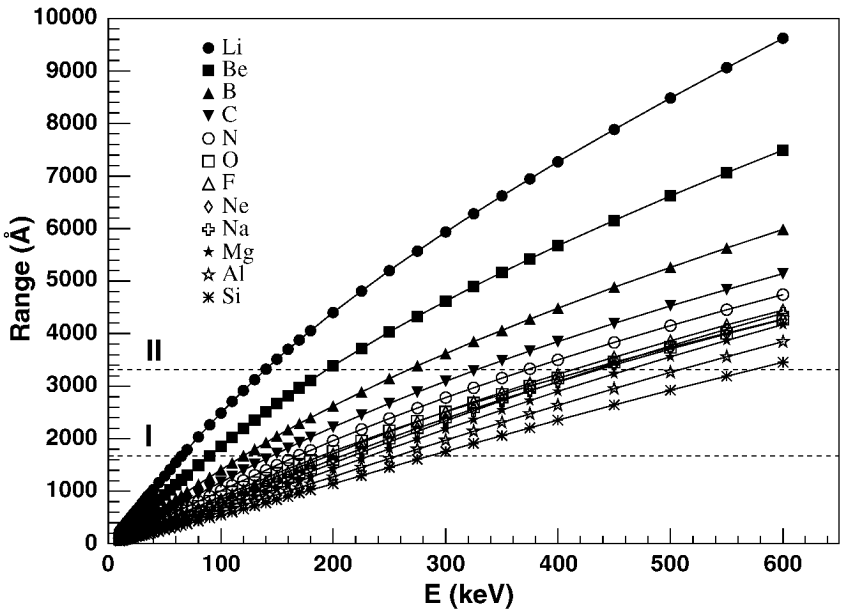

Figure B.2. Simulated range of the intermediate mass fragments ($6 \leqslant A \leqslant 28$) in the ^{nat}Ni target as a function of fragment incident energy. The symbols "I" and "II" correspond to the thicknesses of about 150 and 300 μg/cm^2 (about 1683 and 3367 Å), respectively.

B.3 Relations between BC parameters

The identification of the atomic number and/or mass of the nuclei registered by the BCD is possible by inspection of various relationships between the BC parameters. These relations are shown in Figs. B.3(a) to B.3(c) on the next page, where the results from the simulations are presented.

In the simulations the inefficiency of the Frish grid was not taken into account. It should be noted that, according to the Refs. [151, 153] this effect is partly responsible for the slope of the

elements' branches (cf. Fig. 6.8 to 6.9 on page 40).

The simulation was performed with use of the Geant4 package [63].

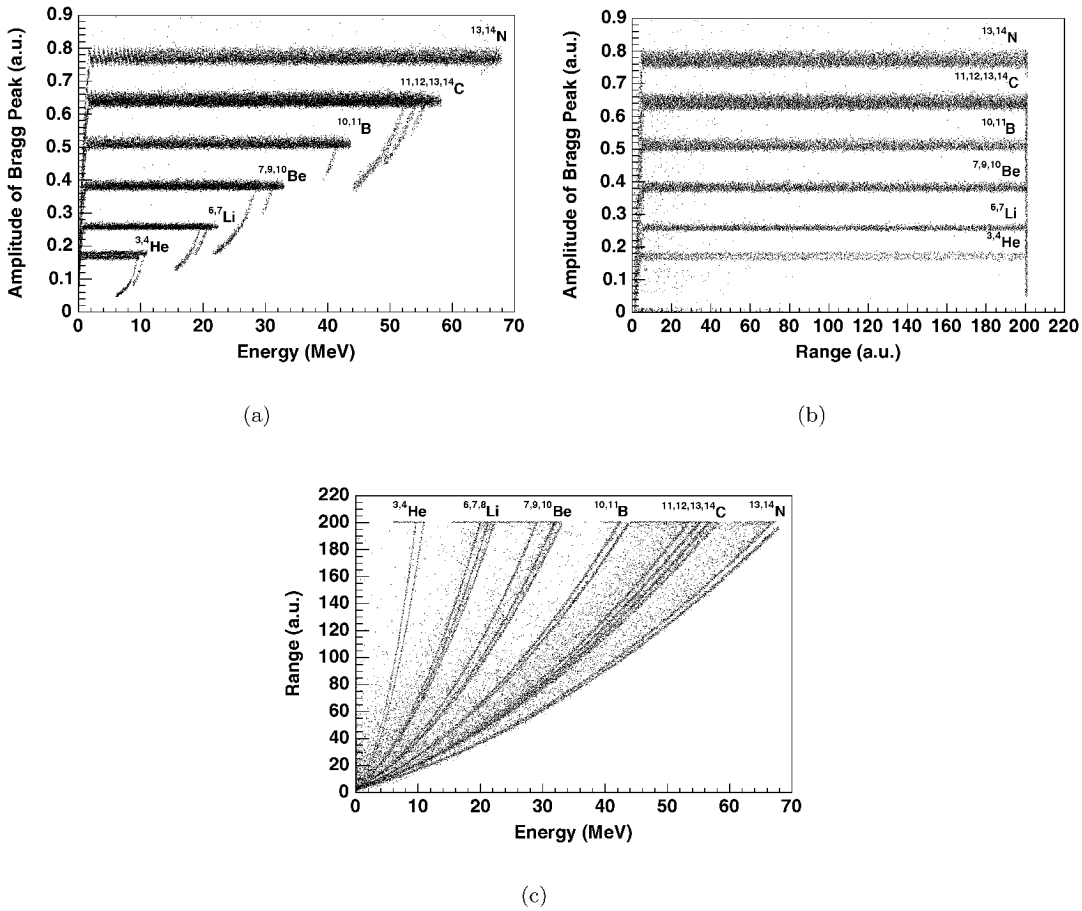

Figure B.3. Scatter plots of the relations between various BC parameters: (a) amplitude of the BP versus energy deposited inside the BCD volume, (b) amplitude of the BP versus depth of particles inside the BCD volume, and (c) depth of particles inside the BCD versus energy deposited inside the BCD volume. The simulation was performed for particles with masses $2 \leqslant A \leqslant 14$.

Appendix C

Example of results from cooled silicon detectors

The mass identification spectra of intermediate mass fragments produced in the p(1.9 GeV) + ^{nat}Ni reaction and measured at 35° by means of the cooled silicon detectors in the telescope geometry are shown in Fig. C.1. Detailed description of silicon detectors can be found in section 3.2.4 on page 21. The relation between energy deposited in the first silicon telescope detector ($\Delta ES1$) versus energy deposited in the second one ($\Delta ES2$) is shown in Fig. C.1(a), whereas energy deposited in the third detector ($\Delta ES2$) versus energy deposited in the second one ($\Delta ES2$) is presented in Fig. C.1(b). The separation of following elements and isotopes has been achieved: He, ^{6}Li, ^{7}Li, ^{8}Li, ^{7}Be, ^{9}Be, ^{10}Be, ^{10}B, ^{11}B and C.

Detailed analysis of the data from cooled silicon detectors is presented in Ref. [186].

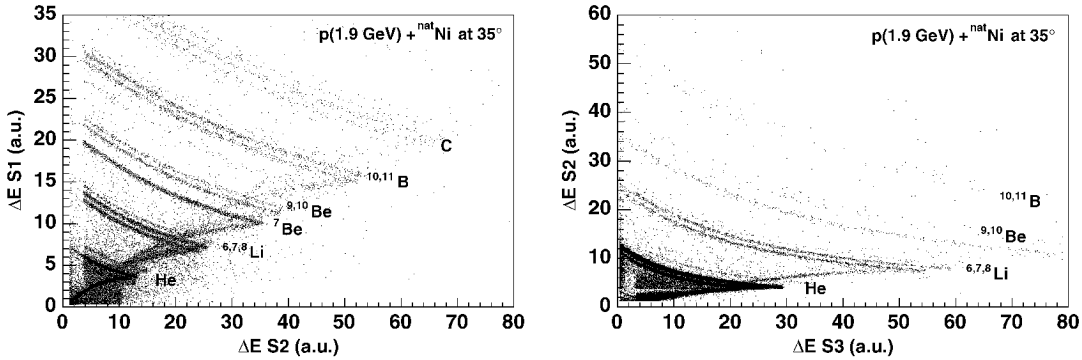

(a) the first silicon detector (S1) versus the second (S2)

(b) the second silicon detector (S2) versus the third (S3)

Figure C.1. Mass identification spectra of intermediate mass fragments emitted in the p(1.9 GeV) + ^{nat}Ni reaction and measured at 35° by means of cooled silicon detectors; S1, S2, S3 - first, second and third silicon detector in the telescope geometry.

Acknowledgments

People don't have to like or support you, so you always have to say thank you.

Ruben Studdard

Numerous people have been indispensable during the completion of this thesis and have given me valuable insights as the project progressed. I had the privilege to be supervised by great people, who offered me their trust and assistance in my PhD studies.

First of all I would like to express my gratitude to my supervisor Prof. Dr. Jan Kisiel for his criticisms, insights, suggestions and continual prodding during the course of this study. His knowledge, continuous interest and criticism were really inestimable. He spent his most precious time to read through my drafts and made many remarks and invaluable comments and suggestions.

I am indebted to Prof. Dr. Detlef Filges, Prof. Dr. Wiktor Zipper and Prof. Dr. Bogusław Kamys for the opportunity to work with the PISA collaboration at the Forschungszentrum Jülich.

I would also like to thank Prof. Dr. Bogusław Kamys for the great support and his outstanding advises throughout the last three years, and finally corrections of this thesis.

I am deeply indebted to Prof. Dr. Lucjan Jarczyk for his criticism and biting comments about my work. He reminded me that sometimes it is better to stop running and to think first.

I owe great debt to Dr. Frank Goldenbaum, a kind, energetic, and hardworking person, for his guidance, numerous helpful comments and suggestions, and his great influence on my work. Thanks also for his help in the administrative issues during my residence in Jülich.

I wish to express my sincere gratitude to Dr. Paweł Kulessa who guided some aspects of my work and helped whenever I was in need, especially greatly enriched my knowledge with his exceptional insights into the world of the acquisition system.

A special thanks also goes to Dr. Krzysztof Pysz for his valuable comments on my thesis.

My greatest debt is also to all these people who contributed to the success of the PISA experiment:

Prof. Dr. Andrzej Magiera, Dr. Stanisław Kistryn and Dr. Paweł Kulessa for their great contribution and effort to the preparation of the electronic for our experiment.

Dr. Krzysztof Pysz, Dr. Regina Siudak and Dr. Stanisław Kliczewski for their work and involvement in order to activate, develop and keep in a good shape the PISA detectors.

Wojtek Migdał and Jerzy Majewski for their technical support.

I wish to thank also Dr. Piotr Kowina for his help in the first days of my residence in Jülich.

I am grateful to the various people, who I have met in Jülich, Katowice and Kraków during the course of this study, for their openness, friendship, support and comradeship; especially to: Basia Bekman, Virgini Bollini, Aga i Piotr Hawranek, Małgosia Kistryn, Staszek Kliczewski, Wojtek Klimala, Ania i Piotr Kowina, Beata i Paweł Kulessa, Ola Matraszek, Wojtek Migdał, Żaneta i Paweł Moskal, Beata i Krzysztof Pysz, Ania i Tomek Rożek, Zbyszek Rudy, Regina Siudak, and last but certainly not least Ola Wrońska. They all created a wonderful working and living environment, very appealing to me. I am very grateful to all of you!

I would also like to acknowledge once more my comrade in sorrows and happiness: Ola Wrońska.

Our meetings and conversations will not be forgotten.

I would like to thank my beloved *femme fatale*: Ola Biegun. Without her charm, dangerously seductive, and all these good and bad experiences, to which she has contributed, my residence in Jülich would not be such varies, exciting, stirring, and sometimes a little thrilling. I am deeply grateful her for being who she is.

I am really grateful to my sister Magda who has always believed that I am able to complete my PhD.

At the end of my thesis I would like to thank once more all those who made this work an enjoyable experience for me. Many people supported me during the completion of this thesis with criticism, helpful assistance and references. This thesis would have never been possible without them.

This thesis is dedicated to the most important person in my whole life: my Mommy. She knows...

Bibliography

[1] A.M. Poskanzer, G.W. Butler and E.K. Hyde, *Fragment Production in the Interaction of 5.5 GeV Protons with Uranium*, Physical Review **C3** (1971) 882.

[2] J.A. Gaidos et al., *Nuclear Fragment Emission in High-Energy p-Xe and p-Kr Collisions and a Description of Their Production Mechanism*, Physical Review Letters **42** (1979) 82.

[3] N.T. Porile et al., *Fragment emission in proton-Xenon interactions in the near-threshold regime*, Nuclear Physics **A471** (1987) 149c.

[4] R.E.L. Green and R.G. Korteling, *Fragment production from p + Ag interactions at intermediate energies*, Physical Review **C22** (1980) 1594.

[5] A.A. Kotov et al., *Intermediate Mass Fragment Production on Au, Ag, Ni and Al Targets Induced by 1 GeV Protons*, Nuclear Physics **A** (1995) 575.

[6] J.E. Finn et al., *Nuclear Fragment Mass Yield from High-Energy Proton-Nucleus Interactions*, Physical Review Letters **49** (1982) 1321.

[7] H. Xi et al., *Influence of secondary dacay on isotope-ratio temperature measurements*, Physical Review **C59** (1999) 1567.

[8] J.P. Bondorf et al., *Statistical multifragmentation of nuclei*, Physics Report **257** (1995) 133.

[9] J.P. Bondorf et al., *Sampling in statistical multifragmentation of nuclei*, Physics Letters **B150** (1985) 57.

[10] J.P. Bondorf et al., *Statistical Multifragmentation of nuclei. (I) Formulation of the model*, Nuclear Physics **A443** (1986) 321.

[11] J.P. Bondorf et al., *Statistical Multifragmentation of nuclei. (II) Application of the model to finite nuclei disassembly*, Nuclear Physics **A444** (1985) 460.

[12] H.W. Barz et al., *Statistical Multifragmentation of nuclei. (III) Decay of the fragments*, Nuclear Physics **A448** (1987) 753.

[13] A.S. Botvina et al., *Statistical simulation of the break-up of highly excited nuclei*, Nuclear Physics **A475** (1987) 663.

[14] J. Bondorf, *Chaotic fragmentation of nuclei*, Nuclear Physics **A387** (1982) 25c.

[15] A.S. Botvin and D.H.E. Gross, *Sequential or simultaneous multifragmentation of nuclei*, Physics Letters **B344** (1995) 6.

[16] A. Chernomoretz et al., *Nonequilibrium effects in fragmentation*, Physical Review **C64** (2001) 24606.

[17] W. Bauer and A. Botvina, *Pre-equilibrium particle emission and critical exponent analysis*, Physical Review **C52** (1995) 1760.

[18] J.J. Griffin, *Statistical Model of Intermediate Structure*, Physical Review Letters **17** (1996) 478.

[19] A.D. Panagiotou et al., *Experimental Evidence for a Liquid-Gas Phase Transition in Nuclear Systems*, Physical Review Letters **52** (1984) 496.

[20] J.B. Elliot et al., *Liquid to Vapor Phase Transition in Excited Nuclei*, Physical Review Letters **88** (2002) 1.

[21] W. Bauer, *Extraction of signals of a phase transition from nuclear multifragmentation*, Physical Review **C38** (1988) 1297.

[22] A. Chbihi, O. Schapiro and D.H.E. Gross, *Experimental and theoretical search for a phase transition in nuclear fragmentation*, The European Physical Journal **A5** (1999) 251.

[23] V.A. Karnaukhov et al., *Critical Temperature for the Nuclear Liquid-Gas Phase Transition*, Physical Review **C67** (2003) 011601, nucl-ex/0302006.

[24] A. Strachan and C.O. Dorso, *Caloric curve in fragmentation*, Physical Review **C58** (1998) 632.

[25] J.B. Natowitz et al., *Caloric curves and critical behavior in nuclei*, Physical Review **C65** (2002) 34618.

[26] A. Chernomoretz, C.O. Dorso and J.A. López, *The Caloric Curve in Collisions*, Acta Physica Hungarica, N.S. Heavy Ion Physics **11** (2000) 0.

[27] R. Wada et al., *Excitation energies and temperatures of hot nuclei produced in the reactions of* $^{63}Cu+^{197}Au$ *at 35A MeV*, Physical Review **55** (1997) 227.

[28] M.B. Tsang, W.G. Lynch and H. Xi, *Nuclear Thermometers from Isotope Yield Ratios*, Physical Review Letters **78** (1997) 3836.

[29] W. Bauer, *Temperatures of fragment kinetic energy spectra*, Physical Review **C51** (1995) 803.

[30] G.M. Raisbeck et al., *Li, Be, and B Production in the 3-GeV proton bombardment of Ni*, Physical Review **C12** (1975) 527.

[31] T.P. Walker, G. Mathews and V.E. Viola, *Astrophysical production rates for Li, Be, and B isotopes from energetic* ^1H *and* ^4He *reaction with HeCNO nuclei*, The Astrophysical Journal **299** (1985) 745.

[32] R. Michel et al., *Nuclide production by proton-induced reactions on elements* ($6 \lesssim Z \lesssim 29$) *in the energy range from 800 to 2600 MeV*, Nuclear Instruments and Methods in Physics Research **B103** (1995) 183.

[33] R. Michel et al., *Cross sections for the production of residual nuclides by low- and medium-energy protons from the target elements C, N, O, Mg, Al, Si, Ca, Ti, V, Mn, Fe, Co, Ni, Cu, Sr, Y, Zr, Nb, Ba and Au*, Nuclear Instruments and Methods in Physics Research **B129** (1997) 153.

[34] *Proton Induced Spallation Database*, SQL database - only electronic version; PISA Collaboration, 2000-2003.

[35] M. Enke et al., *Evolution of a spallation reaction: experiment and Monte Carlo simulation*, Nuclear Physics **A657** (1999) 317.

[36] D. Filges, F. Goldenbaum and Y. Yariv, editors, Proceedings of the Fifth Workshop On Simulating Accelerator Radiation Enviroment (SARE-5); Models and Codes for Spallation Neutron Source, OECD Headquarters, Paris, France, Forschungszentrum Jülich, 2001.

[37] C. Herbach et al., Proceedings of the International Conference on Nuclear Data for Science and Technology ND2001, Tsukuba, Japan, Nuclear Data Center, JAERI.

[38] W.C. Hsi et al., *Formation of Hot Nuclei with GeV p and π^- Beams*, Physical Review Letters **79** (1997) 817.

[39] L.N. Andronenko et al., Z. Phys. **A318** (1984) 97.

[40] D. Hilscher et al., *Neuton production by hadron-induced spallation reactions in thin and thick Pb and U targets from 1 to 5 GeV*, Nuclear Instruments and Methods in Physics Research **A414** (1998) 100.

[41] O.A. Schaeffer and A. Zähringer, *High-Sensitivity Mass Spectrometric Measurement of Stable Helium and Argon Isotopes Produced by High-Energy Protons in Iron*, Physical Review **113** (1959) 674.

[42] R.H. Bieri and W. Rutsch, Helvetica Physica Acta **35** (1962) 553.

[43] K. Goebel, H. Schultes and J. Zähringer, Report CERN 64-12 (1964).

[44] S.L. Green et al., J. Nucl. Mater. **115-157** (1988) 1350.

[45] C.M. Herbach et al., Proceedings of the Fifth Workshop On Simulating Accelerator Radiation Enviroment (SARE-5); Models and Codes for Spallation Neutron Source, edited by D. Filges, F. Goldenbaum and Y. Yariv, p. 7, OECD Headquarters, Paris, France, Forschungszentrum Jülich, 2001.

[46] J. Cugnon, C. Volant and S. Vuillier, *Improved intranuclear cascade model for nucleon-nucleus interactions*, Nuclear Physics **A620** (1997) 475.

[47] J. Cugnon and P. Henrotte, Proceedings of the Fifth Workshop On Simulating Accelerator Radiation Enviroment (SARE-5); Models and Codes for Spallation Neutron Source, edited by D. Filges, F. Goldenbaum and Y. Yariv, p. 65, OECD Headquarters, Paris, France, Forschungszentrum Jülich, 2001.

[48] P. Cloth et al., *HERMES; A Monte Carlo Program System for Beam-Materials Interaction Studies*, Report Jülich 2203, 1988.

[49] R.E. Prael and H. Lichtenstein, Report LA-UR-89-3014, 1989.

[50] R.E. Prael, Issyles-Moulineaux, France, OECD, p. 145, 1994.

[51] S.G. Mashnik et al., *Cascade-exciton model analysis of proton induced reactions from 10 MeV to 5 GeV*, Nuclear Instruments and Methods in Physics Research **A414** (1998) 68.

[52] S.J. Yennello et al., *Intermediate mass fragment emission in the 161 MeV p + Ag reaction*, Physical Review **C41** (1990) 79.

[53] R.E.L. Green, R.G. Korteling and K.P. Jackson, *Inclusive production of isotopically resolved Li through Mg fragments by 480 MeV p+Ag reactions*, Physical Review **C29** (1984) 1806.

[54] G.D. Westfall et al., *Energy spectra of nuclear fragments produced by high energy protons*, Physical Review **C17** (1978) 1368.

[55] K. Hagel et al., *Production and characterization of hot nuclei in the reaction of 19 and 35 MeV/u ^{14}N with ^{145}Sm*, Nuclear Physics **A486** (1988) 429.

[56] D. Cussol et al., *Charge - particles calorimetry of ^{40}Ar + 27Al reaction from 36 to 65 MeV/u*, Nuclear Physics **A561** (1993) 298.

[57] D.H.E. Gross, Z. Xiao-ze and X. Shu-yan, *Decay of Very Hot Nuclei*, Physical Review Letters **56** (1986) 1544.

[58] A.S. Hirsch et al., *Experimental results from high energy proton-nucleus interactions, critical phenomena, and the thermal liquid drop model of fragment production*, Physical Review **C29** (1984) 508.

[59] S. Albergo et al., *Temperature and Free-Nucleon Densities of Nuclear Matter Exploding into Light Clusters in Heavy-Ion Collision*, Il Nuovo Cimento **A** (1985) 1.

[60] M.B. Tsang et al., *Cross comparison of nuclear temperatures determined from excited state populations and isotope yields*, Physical Review **C53** (1996) R1057.

[61] M.J. Huang et al., *Temperature Measurements for Central Au+Au Collisions at 35A MeV*, Physical Review Letters **78** (1997) 1648.

[62] Y.G. Ma et al., *Surveying the nuclear caloric curve*, Physics Letters **B390** (1997) 41.

[63] S. Agostinelli et al., *Geant - 4 a simulation toolkit*, Nuclear Instruments and Methods in Physics Research **A506** (2003) 250.

[64] J.F. Ziegler, J.P. Biersack and U. Littmark, The Stopping and Range of Ions in Solid (Pergamon Press, New York, 1996).

[65] J.P. Biersack and L. Haggmark, *A monte carlo computer program for the transport of energetic ions in amorphous targets*, Nuclear Instruments and Methods **174** (1980) 257.

[66] J. Hüfner, *Heavy fragments produced in proton-nucleus and nucleus-nucleus collisions at relativistic energies*, Physics Report **125** (1984) 129.

[67] I.I. Gurevich et al., Dokl. Akad. Nauk SSSR **18** (1938) 169.

[68] E. Schopper, Naturwissenschafter **25** (1937) 557.

[69] J. Knoll and B. Strack, *The dynamics of the nuclear disassembly in a field-theoretical model at finite entropies*, Physics Letters **B149** (1984) 45.

[70] B. Strack, *Fragmentation of hot quantum drops*, Physical Review **C35** (1987) 691.

[71] D. Vautherin, J. Treiner and M. Vénŕoni, *Evolution of hot compressed nuclei in the time-dependent Hartree-Fock approximation*, Physics Letters **B191** (1987) 6.

[72] A. Dhar and S. Das Gupta, *Time evolution of a compressed nucleus in the time-dependent Hartree-Fock approximation*, Physical Review **C30** (1984) 1545.

[73] S. Das Gupta et al., *Mass distributions from microscopic models of heavy ion collisions*, Physical Review **C35** (1987) 556.

[74] A. Vicentini, G. Jacucci and V.R. Pandharipande, *Fragmentation of hot classical drops*, Physical Review **C31** (1985) 1783.

[75] J. Aichelin et al., *Quantum molecular dynamics approach to heavy ion collisions: Description of the model, comparison with fragmentation data, and the mechanism of fragment formation*, Physical Review **C37** (1988) 2451.

[76] G. Peilert et al., *Multifragmentation, fragment flow, and the nuclear equation of state*, Physical Review **C39** (1989) 1402.

[77] J. Aichelin and G. Bertsch, *Numerical simulation of medium energy heavy ion reactions*, Physical Review **C31** (1985) 1730.

[78] J. Aichelin, *Three heavy fragments observed in simulations of medium energy heavy ion reactions*, Physics Letters **B175** (1986) 120.

[79] D.H. Boal and J.N. Glosli, *From binary breakup to multifragmentation: Computer simulation*, Physical Review **C37** (1988) 91.

[80] G.F. Bertsch and S. Das Gupta, *A guide to microscopic models for intermediate energy heavy ion collisions*, Physical Review **160** (1988) 189.

[81] J. Aichelin, J. Hüfner and R. Ibarra, *Cold breakup of spectator residues in nucleus-nucleus collisions at high energy*, Physical Review **C30** (1984) 107.

[82] D.J. Fields et al., *Complex particle emission from decaying regions of high excitation formed in ^{12}C induced reactions on ^{197}Au at E/A = 30 MeV*, Physical Review **C30** (1984) 1912.

[83] B.E. Hasselquist et al., *Light-particle-complex-fragment coincidence cross sections from intermediate energy nucleus-nucleus collisions*, Physical Review **C32** (1985) 145.

[84] W. Bauer et al., *The nuclear lattice model of proton-induced multi-fragmentation reactions*, Nuclear Physics **A452** (1986) 699.

[85] H. Jaqaman, A.Z. Mekjian and L. Zamick, *Nuclear condensation*, Physical Review **C27** (1983) 2782.

[86] H. Jaqaman, A.Z. Mekjian and L. Zamick, *Liquid-gas phase transitions in finite nuclear matter*, Physical Review **C29** (1984) 2067.

[87] H.T. M. W. Curtin and D.K. Scott, *Liquid-gas phase instabilities in nuclear systems*, Physics Letters **B123** (1983) 289.

[88] A.D. Panagiotou, M.W. Curtin and D.K. Scott, *Fragmentation instabilities in nuclear systems*, Physical Review **C31** (1985) 55.

[89] G. Bertsch and P.J. Siemens, *Nuclear fragmentation*, Physics Letters **B126** (1983) 9.

[90] G. Fái and J. Randrup, *Explosion-evaporation model for fragment production in medium-energy nuclear collisions*, Nuclear Physics **A381** (1982) 551.

[91] G. Fái and J. Randrup, *Statistical simulation of complete events in energetic nuclear collisions*, Nuclear Physics **A404** (1983) 557.

[92] G. Röpke, *Particle clustering and Mott transitions in nuclear matter at finite temperature : (I). Method and general aspects*, Nuclear Physics **A379** (1982) 536.

[93] J. Randrup and S.E. Koonin, *The disassembly of nuclear matter*, Nuclear Physics **A356** (1981) 223.

[94] D. Hahn and H. Stöcker, *The quantum statistical model of fragment formation: Entropy and temperature extraction in heavy ion collisions*, Nuclear Physics **A476** (1988) 718.

[95] A.Z. Mekjian, *Explosive nucleosynthesis, equilibrium thermodynamics, and relativistic heavy-ion collisions*, Physical Review **C17** (1978) 1051.

[96] O. Hahn and F. Strassman, Naturwiss. **27** (1939) 11.

[97] L. Meitner and O. Frisch, *Disintegration of Uranium by Neutrons: a New Type of Nuclear Reaction*, Nature **143** (1939) 239.

[98] D. Hilscher, *Wie langsam ist die Kernspaltung?*, Physikalische Blätter (1991) 1073.

[99] A. Iljinov et al., *An Analysis of nuclear fissility for intermediate-energy proton induced reactions*, Z.F.Phys. **A248** (1978) 37.

[100] H.W. Bertini, *Low-Energy Intranuclear Cascade Calculation*, Physical Review **131** (1963) 1801.

[101] J. Pochodzalla et al., *Two-particle correlations at small relative momenta for ^{40}Ar induced reactions on ^{197}Au at E/A=60 MeV*, Physical Review **C35** (1987) 1695.

[102] W.A. Friedman and W.G. Lynch, *Statistical formalism for particle emission*, Physical Review **C28** (1983) 16.

[103] P.M. Milazzo et al., *Temperature measurement of fragment emitting systems in Au+Au 35 MeV/nucleon collisions*, Physical Review **C58** (1998) 953.

[104] H. Xi et al., *Dinamical emission and isotope thermometry*, Physical Review **C58** (1998) 2636.

[105] R. Maier, *Cooler synchrotron COSY - performance and perspectives*, Nuclear Instruments and Methods in Physics Research **A390** (1997) 1.

[106] H. Stockhorst et al., Proceedings of EPAC, Viena, Austria, 2000.

[107] R. Tölle et al., Proceedings of EPAC, pp. 572–574, Fifth European Particle Accelerator Conference, 1996.

[108] H. Ohm, *PISA Targets and Beam Properties of COSY*, Forschungszentrum Jülich, Germany, 2001.

[109] R. Barna et al., *Development of the PISA experimental setup*, Annual Report, Forschungszentrum Jülich, Germany, 2000.

[110] C. Schiessl et al., *A Bragg-curve spectroscopy detector*, Nuclear Instruments and Methods **192** (1982) 291.

[111] R.M. Barnett et al., *Review of Particle Physics*, Physical Review **D54** (1996).

[112] *Review of Particle Physics*, Particle Data Group (2000).

[113] D.E. Groom et al., *Review of Particle Physics*, The European Physical Journal **C15** (2000) 1.

[114] H.J. Shenhav and H. Stelzer, *The mass dependence of the signal peak height of Bragg-curve ionization chamber*, Nuclear Instruments and Methods in Physics Research **228** (1985) 359.

[115] J. Majewski, private communication.

[116] R. Barna et al., *PISA - an Experiment for Fragment Spectroscopy at the Internal Beam of COSY: Application of an Axial Ionization Chamber*, Nuclear Instruments and Methods in Physics Research **A519** (2004) 610.

[117] Costruzioni Apparecchiature Elettroniche Nucleari (C.A.E.N.), Technical Information Manual, MOD. V729 A, 4 Channel, 12 bit, 40 MHz ADC, 1999.

[118] G.F. Knoll, Radiation Detection and Measurement (John Wiley and Sons, 1989).

[119] *International Organization for Standarization, ISO9506 - Manufacturing Message Specification*, 1990.

[120] M. Drochner, *Das EMS-Client Program "klient" - Benutzeranleitung*, Interner Bericht KFA-ZEL-IB-501094, Zentral Labor für Elektronik, Forschungszentrum Jülich, 1993.

[121] M. Drochner, *Multiprozessor VME-Eventbuilder auf der Basis der objektorientierten Experimental Message Specification. Berichte zum Datenerfassungssystem fur physikalische Experimente an COSY KFA-ZEL*, Interner Bericht, Zentral Labor für Elektronik, Forschungszentrum Jülich, 1993.

[122] K. Zwoll, M. Drochner and P. Wüstner, *Objektorientrierte Modellierung des On-Line Datenerfassungssystems fur COSY-Experimente. Berichte zum Datenerfassungssystem für physikalische Experimente an COSY KFA-ZEL*, Interner Bericht, Zentral Labor für Elektronik, Forschungszentrum Jülich, 1993.

[123] W.D. Peterson, VMEbus Handbook, 4th ed. (VITA, 1997).

[124] *HyperDictionary.com*, Internet web page: http://www.hyperdictionary.com, 2000-2003 WEBNOX Corporation.

[125] M. Drochner, Aufbau eines flexiblen Datensufnahmesystems für das GEM-Experiment am Jülicher Beschleuniger COSY und Messungen der Reaktion $pp \rightarrow \pi^+ d$ nahe der Produktionsschwelle, PhD thesis, Technischen Universität Dresden, 1996.

[126] B. Eckel, Thinking in C++, 2nd ed. (Prentice Hall, Upper Saddle River, New Jersey 07458, 2000).

[127] B. Welch, K. Jones and J. Hobbs, Practical Programming in Tcl and Tk, 4th ed. (Prentice Hall, 2003), ISBN: 0-13-038560-3.

[128] M. Cooper, Advanced Bash-Scripting Guide. An in-depth exploration of the art of shell scripting, Linux Documentation Project Guides, 2.5 ed., 2004.

[129] W.R. Stevens, UNIX Network Programming (Prentice-Hall, 1990), Hard cover, 772 pp.

[130] O. Kirch and T. Dawson, Linux Network Administrator's Guide, 2nd ed. (O'Reilly, 2000).

[131] R. Brun and F. Rademaker, *ROOT - An Object Oriented Data Analysis Framework*, Nuclear Instruments and Methods in Physics Research **A389** (1997) 81, See also http://root.cern.ch/.

[132] Costruzioni Apparecchiature Elettroniche Nucleari (C.A.E.N.), Technical Information Manual, MOD. V785 series, MOD. V785 N series, 32/16 Channel Peak Sensing ADCs, 2002.

[133] Costruzioni Apparecchiature Elettroniche Nucleari (C.A.E.N.), Technical Information Manual, MOD. V793 QDC, 2002.

[134] Costruzioni Apparecchiature Elettroniche Nucleari (C.A.E.N.), Technical Information Manual, MOD. V560, 16 Channel Scaler, 1993.

[135] Costruzioni Apparecchiature Elettroniche Nucleari (C.A.E.N.), Technical Information Manual, MOD. V830, 32 Channel Latching Scaler, 1993.

[136] Costruzioni Apparecchiature Elettroniche Nucleari (C.A.E.N.), Technical Information Manual, MOD. V259E, 16 bit Strobed Multi-hit Pattern Unit, 1991.

[137] Costruzioni Apparecchiature Elettroniche Nucleari (C.A.E.N.), Technical Information Manual, MOD. V775, 32 Channel Multievent TDC, 2001.

[138] A. Strzałkowski, Wstęp fo fizyki jądra atomowego, 3rd ed. (Państwowe Wydawnictwo Naukowe, Warszawa, 1979).

[139] J.F. Kenney and E.S. Keeping, Methematics of Statistics, 3rd ed. (Princeton, 1962).

[140] E.T. Whittaker and G. Robinson, The Calculus of Observations: A Treatise on Numerical Mathematics, 4th ed. (Dover, New York, 1967).

[141] I.N. Bronsztejn and K. Siemiendiajew, Matematyka - poradnik encyklopedyczny, 6th ed. (Państwowe Wydawnictwo Naukowe, Warszawa, 1976).

[142] M. Abramowitz and I.A. Stegun, Handbook of Mathematical Functions with Formulas, Graphs, and Mathematical Tables, 9th ed. (Dover, New York, 1972).

[143] V. Adamchik, *The Evaluation of Integrals of Bessel Functions via G-Function Identities*, J. Comput. Appl. Math. **64** (1995) 573.

[144] G. Arfken, Mathematical Methods for Physicists (Academic Press, Orlando FL, 1985) chap. 11 - Bessel Functions, pp. 573–636.

[145] W.G. Bickley, Bessel Functions and Formulae (Cambridge University Press, Cambridge, England, 1957).

[146] F. Bowman, Introduction to Bessel Functions (Dover, New York, 1958).

[147] W.E. Byerly, An Elementary Treatise on Fourier's Series, and Spherical, Cylindrical, and Ellipsoidal Harmonics, with Applications to Problems in Mathematical Physics (Dover, New York, 1959) chap. 7 - Cylindrical Harmonics (Bessel's Functions), pp. 219–237.

[148] A. Gray and G.B. Mathews, A Treatise on Bessel Functions and Their Applications to Physics, 2nd ed. (Dover, New York, 1966).

[149] W.H. Press et al., Numerical Recipes in FORTRAN: The Art of Scientific Computin, 2nd ed. (Cambridge University Press, Cambridge, England, 1992) chap. Bessel Functions of Integral Order, Bessel Functions of Fractional Order, Airy Functions, Spherical Bessel Functions, pp. 223–229, 234–245.

[150] G.N. Watson, A Treatise on the Theory of Bessel Functions, 2nd ed. (Cambridge University Press, Cambridge, England, 1966).

[151] J.M. Asselineau et al., *Performance of a Bragg curve detector for heavy ion identification*, Nuclear Instruments and Methods **204** (1982) 109.

[152] C.R. Gruhn et al., *Bragg curve spectroscopy*, Nuclear Instruments and Methods **196** (1982) 33.

[153] L.N. Andronenko et al., *A twin axial ionization chamber for studies of multiple intermediate-mass-fragment production in 1 GeV proton-nucleus collisions*, Nuclear Instruments and Methods in Physics Research **A312** (1992) 467.

[154] H. Ochiishi et al., *Application of Bragg-curve counters to a target multifragmentation measurement*, Nuclear Instruments and Methods in Physics Research **A369** (1996) 269.

[155] M.F. Vineyard et al., *Performance of a large Bragg-curve spectrometer*, Nuclear Instruments and Methods in Physics Research **A255** (1987) 507.

[156] M.N. Andronenko and W. Neubert, *Application of Pulse Shape Analysis to Isotope Separation in Bragg Curve Spectroscopy*, Annual Report, Forschungszentrum Rossendorf, Germany, 1998.

[157] R. Gold, *An iterative unfolding method for matrices*, Mathematics and Computer Research and Development Rep. ANL-6984, Argonne National Laboratory (1964).

[158] M. Morháč et al., *Efficient one- and two-dimensional gold deconvolution and its application to γ-ray spectra decomposition*, Nuclear Instruments and Methods in Physics Research **A401** (1997) 385.

[159] K.V. Babu, Y. Yoganandam and V. U.Reddy, *Adaptive estimation of eigensubspace and tracking the directions of arrival*, Signal Processing **68** (1998) 317.

[160] M. Morháč and V. Matoušek, *Fast adaptive Fourier-based transform and its use in multi-dimensional data compression*, Signal Processing **68** (1998) 141.

[161] M. Namb and Y. Ishida, *Wavelet transform domain blind deconvolution*, Signal Processing **68** (1998) 119.

[162] S.J. Yennello et al., *Multifragment Emission in Reaction Induced by 0.90 and 3.6 GeV ^3He Ions on ^{nat}Ag*, Physical Review Letters **67** (1991) 671.

[163] K. Kwiatkowski et al., *Multifragmentation in the 4.8-GeV ^3He + ^{nat}Ag, ^{197}Au Reactions*, Physical Review Letters **74** (1995) 3756.

[164] R. Wada et al., *Temperatures and excitation energies of hot nuclei in the reactions of ^{32}S+Ag and ^{16}O+Ag at 30 MeV/nucleon*, Physical Review **C39** (1989) 497.

[165] M.N. Andronenko et al., *Peculiarities of isotopic temperatures obtained from p + A collisions at 1 GeV*, The European Physical Journal **A** (2000) 9.

[166] K.G.R. Doss et al., *Fragment Flow in Nuclear Collisions*, Physical Review Letters **59** (1987) 2720.

[167] W.C. Hsi et al., *Collective Expansion in Central Au + Au Collisions*, Physical Review Letters **73** (1994) 3367.

[168] S.C. Jeong et al., *Collective motion in selected central collisions of Au on Au at 150A MeV*, Physical Review Letters **72** (1994) 3468.

[169] M. Gonin et al., *Dynamical effects on the de-excitation of hot nuclei with A = 160*, Physical Review **C42** (1990) 2125.

[170] J. Pochodzalla et al., *Probing the Nuclear Liquid-Gas Phase Transition*, Physical Review Letters **75** (1995) 1040.

[171] J.A. Hauger et al., *Two-stage multifragmentation of 1A GeV Kr, La, and Au*, Physical Review **C62** (2000) 24616.

[172] K. Kwiatkowski et al., *Heating nuclear matter with GeV ^3He beams*, Physical Review Letters **B423** (1998) 21.

[173] K.B. Morley et al., *4 π studies of the 1.8-4.8 GeV ^3He+^{nat}Ag, ^{197}Au reactions. II. Multifragmentation*, Physical Review **C54** (1996) 749.

[174] K.B. Morley et al., *4 π studies of the 1.8-4.8 GeV ^3He+^{nat}Ag, ^{197}Au reactions. I. Energy deposition*, Physical Review **C54** (1996) 737.

[175] J. Cibor et al., *Dynamic evolution and the caloric curve for medium mass nuclei*, Physics Letters **B473** (2000) 29.

[176] K. Hagel et al., *Light particle probes of expansion and temperature evolution: Coalescence model analyses of heavy ion collisions at 47A MeV*, Physical Review **C62** (2000) 034607.

[177] A. Ruangma et al., *Caloric curve of 8-GeV/c pi-, anti-p + Au-197 reactions*, Physical Review **C66** (2002) 044603, nucl-ex/0110004.

[178] A. Boudard et al., *Intranuclear cascade model for a comprehensive description of spallation reaction data*, Physical Review **C66** (2002) 044615.

[179] F. Goldenbaum, private communication.

[180] N.T. Porille et al., *Approach to criticalty in the fragmentation of xenon by 1-19 GeV protons*, Physical Review **C39** (1989) 1914.

[181] C.B. Chitwood et al., *Emission of complex nuclei in ^{12}C induced reactions at E/A = 15 and 30 MeV*, Physical Review **B131** (1983) 289.

[182] V. Serfling et al., *Temperature of Exploding Nuclei*, Physical Review Letters **80** (1998) 3928.

[183] S. Das Gupta, A.Z. Mekjian and M.B. Tsang, *Liquid-gas phase transition in nuclear multifragmentation*, (2000), nucl-th/0009033.

[184] L.G. Moretto et al., *Comment on "Probing the Nuclear Liquid-Gas Phase Transition"*, Physical Review Letters **76** (1996) 2822.

[185] V. Bollini et al., *Study of efficiency of Multichannel Plate detector used in PISA experiment*, Annual Report, Forschungszentrum Jülich, Germany, 2003.

[186] V. Bollini, Energetic intermediate mass fragments emission from proton nucleus collision, PhD thesis, Bergischen Universität - Gesamthochschule Wuppertal, 2004, In progress.